Miniaturized Passive Hydrogel Check Valves for the Treatment of Hydrocephalic Fluid Retention

by

Seunghyun Lee

A Dissertation Presented in Partial Fulfillment
of the Requirements for the Degree
Doctor of Philosophy

Approved October 2020 by the
Graduate Supervisory Committee:

Jennifer Blain Christen, Chair
Michael Goryll
Mehdi Nikkhah
SungMin Sohn

ARIZONA STATE UNIVERSITY

December 2020

ABSTRACT

BioMEMS has the potential to provide many future tools for life sciences, combined with microfabrication technologies and biomaterials. Especially due to the recent COVID-19 epidemic, interest in BioMEMS technology has increased significantly, and the related research has also grown significantly. The field with the highest demand for BioMEMS devices is in the medical field. In particular, the implantable device field is the largest sector where cutting-edge BioMEMS technology is applied along with nanotechnology, artificial intelligence, genetic engineering, etc. However, implantable devices used for brain diseases are still very limited because unlike other parts of human organs, the brain is still unknow area which cannot be completely replaceable.

To date, the most commercially used, almost only, implantable device for the brain is a shunt system for the treatment of hydrocephalus. The current cerebrospinal fluid (CSF) shunt treatment yields high failure rates: ~40% within first 2 years and 98% within 10 years. These failures lead to high hospital admission rates and repeated invasive surgical procedures, along with reduced quality of life. New treatments are needed to improve the disease burden associated with hydrocephalus. In this research, the proposed catheter-free, completely-passive miniaturized valve is designed to alleviate hydrocephalus at the originating site of the disorder and diminish failure mechanisms associated with current treatment methods. The valve is composed of hydrogel diaphragm structure and polymer or glass outer frame which are 100% bio-compatible material. The valve aims to be implanted between the sub-arachnoid space and the superior sagittal sinus to regulate the CSF flow substituting for the obstructed arachnoid granulations.

A cardiac pacemaker is one of the longest and most widely used implantable devices and the wireless technology is the most widely used with it for easy acquisition of vital signs and rapid disease diagnosis without clinical surgery. But the conventional pacemakers with some wireless technology face some essential complications associated with finite battery life, ultra-vein pacing leads, and risk of infection from device pockets and leads. To solve these problems, wireless cardiac pacemaker operating in fully-passive modality is proposed and demonstrates the promising potential by realizing a prototype and functional evaluating.

ACKNOWLEDGMENTS

I am grateful for my fellow lab members and their friendship, amusement, and support. The invaluable knowledge and experiences that I obtained through the insightful discussion with them would not have been attainable elsewhere and strongly influenced my research abilities.

I was fortunate to have the opportunity to conduct research under Dr. Junseok Chae's guidance. Whenever my passion for research cooled down, I was able to stand up again with generous encouragement and advice. Working with Dr. Chae has greatly strengthened my ability and desire to pursue research. Thank you for his patience and enthusiasm, and always for his sincere and thorough advice and counsel. Although his life did not end with a happy ending, I believe that his excellent guidance as a leader, and a warm friendship and generosity as a mentor or even a friend, will always be kept in my heart and will lead many of his disciples, including myself, to a happy ending. The warmth of the cup of coffee I had with Dr. Chae someday in the past is still unforgettable. He left so suddenly that I couldn't even say goodbye, but I will definitely go say hello to him next time with a cup of coffee.

I am grateful towards my current PI, Dr. Jennifer Blain Christen. I am indebted to her for the great support and contribution to my doctoral studies. Without her help and guidance, I can't imagine the end of my Ph.D. program. Not only in research but also outside of research, seeing her always caring for students as a truly inspiring mentor and living a busy life for her research gives me motivation for the new start of my life. Although I haven't been able to do research with her for a long time, I am countless

fortunate to be able to finish my Ph.D. life under her guidance at this most important time in my life.

I would like to thank Drs. Michael Goryll, Mehdi Nikkhah and Sungmin Sohn for serving as my committee, enhancing my knowledge and skillsets by their thoughtful consideration and critic of my research and for contributing their valuable time and energy towards my research studies. Their willingness to become a committee in this tough season gave me a lot of encouragement in finishing my Ph.D. course.

I also wish to thank Dr. Mark C. Preul and Dr. Ruth E. Bristol for their valuable help in functional testing of the hydrogel valves including CSF and animal models. Their experienced insight and feedback onto methods of improving the valve and its clinical relevance is a great driving force in continuing hydrocephalus research.

TABLE OF CONTENTS

Page

CHAPTER Page

LIST OF TABLES

Table Page

LIST OF FIGURES

Figure Page

Figure Page

Figure Page

CHAPTER 1

1. INTRODUCTION

1.1. Micro Electro Mechanical Systems (MEMS): The Core of the 4th Industrial Revolution

The name of MEMS is an abbreviation of Micro Electro Mechanical System. MEMS is referred to as a microscopic 3D structure or a system implementation technology. It is a compact and complex system that performs high-level operation and is sometimes called a microsystem or a micromachine. MEMS is based on the technology of semiconductor integrated circuits and is manufactured with micro-processing technology that combines various technologies such as electronics, machinery, light, and materials, so it is suitable for most electronics, machines and parts with miniaturization, integration, low power and low cost purposes (LyshevskiSergey, 2018). Basically, MEMS has developed along with semiconductor technology. It is made through deposition, patterning through photolithography, which is a general semiconductor production method, and etching to produce a required shape. MEMS is made of various materials such as silicon, polymer, metal, ceramic, etc., depending on the purpose or function to be implemented, and MEMS made in this way is playing new functions and roles by providing a mechanical drive method in the size of millimeters to micrometers.

Looking at the beginning of MEMS, there were attempts to make silicon-based sensors already in the 1970s. At that time, the semiconductor manufacturing technology began to develop integrated sensors with built-in peripheral circuits (BogueRobert, 2013). In the 1980s, the manufacture of simple mechanical parts using the semiconductor production process began. In the early 1980s, micro-mechanical elements such as springs

and cantilevers were manufactured. In the late 1980s, microstructures separated from the substrate such as micro motors, and gears were produced (MehreganyM.,, 1999). Then, in the 1990s, sensors, logic circuits, and drivers were developed in an integrated form. In particular, as the 2000s began, research on MEMS sensors has been conducted in earnest, and MEMS technology has become an essential element in realizing the miniaturization, high performance, and high integration of sensors (WiseKensall, 2007). In terms of materials, it has passed the initial stage of using only pure silicon, and is changing with the combination of silicon and new materials, and the sensing area is also expanding from dynamic sensors to other energy areas such as temperature, light, gas, and bio applications (CiutiGastone,, 2015).

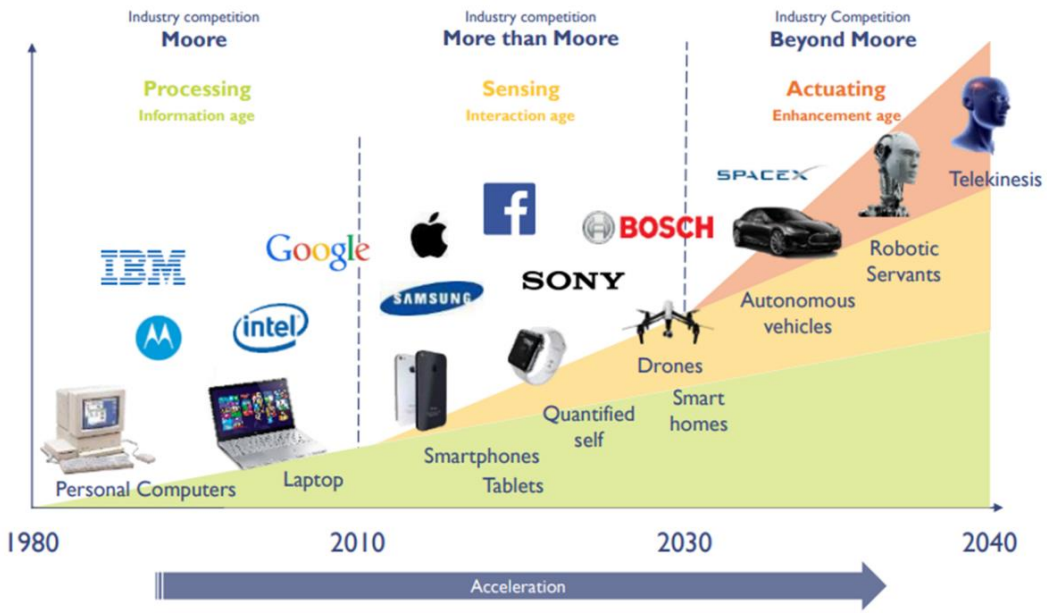

Figure 1.1. Roadmap of MEMS & Sensors. MEMS sensor refers to a high-sensitivity sensor in micro or nano units manufactured by applying microfabrication technology of semiconductor manufacturing process. There are various types of motion sensors,

environmental sensors, and acoustic sensors, and recently, the market is expanding rapidly as MEMS technology is used in gyroscopes and acceleration sensors applied to smartphones, mobile game consoles and autonomous vehicles. MEMS devices were initially applied as automotive and industrial sensors, then expanded to printers and display devices, and rapidly increased as they were applied to mobile, and are expected to expand further in the age of Internet of Things (IoT) (Yole Development, 2016).

Now, MEMS sensors are increasingly replacing the existing sensor market and widely used in various fields such as home appliances, automobiles, industry, healthcare, defense, communications, and aerospace. For examples, MEMS acceleration sensors are applied to mobile phones to perform functions such as bearing and pedometer (Shin, et al., 2017; Flader, et al., 2019; Seshia, et al., 2002), and MEMS gyro sensors are replacing the quartz gyro used to correct hand-vibration of digital cameras (Nitzan, et al., 2015). In addition, the printing inkjet head is a product that is only possible by MEMS technology (Meinhart, 2000) (Lee, 2013) . In the automotive field, it is used in various electronic control units, electronically controlled driving stabilization devices, etc., and is used as a pressure sensor, optical sensor, IR sensor, gas sensor, etc. in various industrial fields (Acar, 2009) (Schoebel, 2005) (Kraft, 2013). As such, the current MEMS technology is playing a very important role in diversifying applications to new industrial sectors as it has been successfully applied in various fields despite a relatively short history. In particular, in recent years, the role of MEMS microphones has emerged with the development of AI, and the related market is rapidly evolving (Sanders, 2009). Like this

way, MEMS has been expected to introduce a variety of promising products in diverse industrial fields.

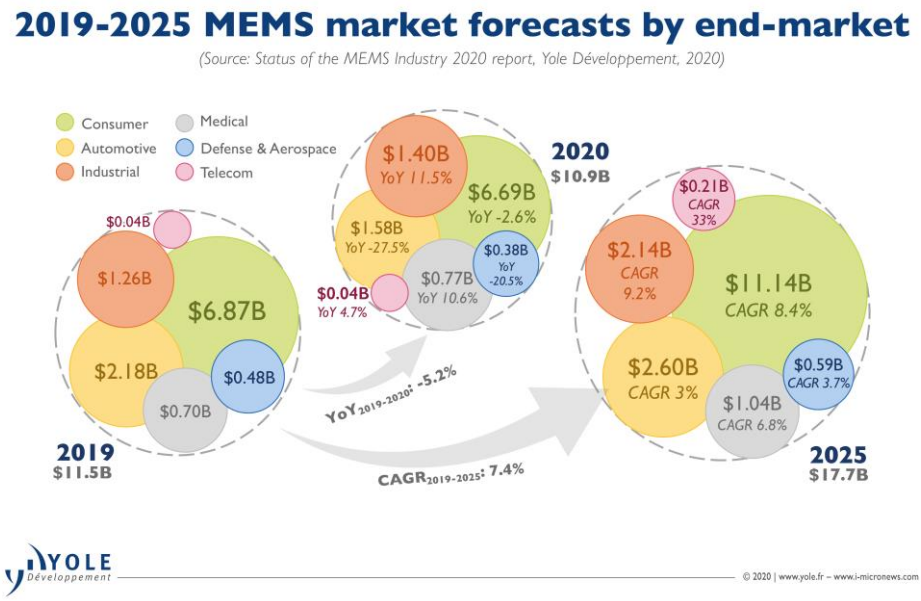

Figure 1.2. MEMS market forecasts by end-market. The global MEMS market is estimated to grow to 7.4% CAGR from $11.5 billion in 2019, reaching $17.7 billion in 2025. In particular, due to the novel coronavirus infection (COVID - 19), the demand for MEMS and sensors used in quarantine and medical fields is expected to increase further, and the need for data collection in artificial intelligence (AI) and autonomous vehicles is also growing (Yole Development, 2019).

According to past statistics, the global market for MEMS is expected to increase from $12 billion in 2017 to $31 billion in 2023 by 17.5% annually. The significant factors to influence the growth of MEMS market are generally related to the increasing popularity of IoT in semiconductors, increasing demand for smart consumer electronics

and wearable devices, and growing adoption of automation in industries, automobiles and homes (Eric Mounier, 2018).

1.2. BioMEMS: MEMS Technology for Biomedical Devices

Recently, healthcare technologies regarding daily life and medicine are being combined with MEMS technology, and a lot of attempts have been made to utilize them in the biotechnology field. For example, real-time analysis and high-sensitivity analysis using very small amounts of biomaterials are performed by detecting and analyzing biomaterials such as DNA, proteins, cells, etc. on a system manufactured with MEMS technology (Grayson, 2004). As described above, one field of MEMS technology that is developed in connection with the bio / health field is called BioMEMS technology, and the technology is recognized as a core platform technology for the development of the biological field. In general, BioMEMS is expanding its application range by fusion with microsystems, nanotechnology, biology, chemistry, medicine, and microfluidics. In addition, such BioMEMS research has very important significance in that it leads directly to usage of the applications in actual medical fields: genomics, proteomics, molecular diagnostics, single cell analysis, point-of-care diagnostics and implantable microdevices (Saliterman, 2006). From this perspective, the market of BioMEMS has achieved remarkable growth in recent years and is expected to grow even further in the near future: the market is expected to grow by 16.5 % annually for the near future. (2020-2025) (MordorIntelligence, 2019). Along with high potential of BioMEMS, a lot of major global companies such as Google, Amazon, Apple, etc. are diving into the investment of research and development in biological fields for developing various healthcare

diagnostic systems and biomedical devices. For example, the mobile care / monitoring applications have been developing from the recent past years with the development and incorporation of advanced technologies in the healthcare industry. Wearable biomedical / biochemical sensors are another major field to drive the growth of the market of BioMEMS. Also, with the interest of the mobile care applications, MEMS sensors play a key role for real-time and non-invasive measurement of biological constituents in personalized medicine and continuous monitoring of human health (Wilson K. P., 2007) (Bashir, 2004). The aging of the population and recent global outbreak of COVID-19 have led the BioMEMS market to have a significant surge with explosive growth of interests in human health.

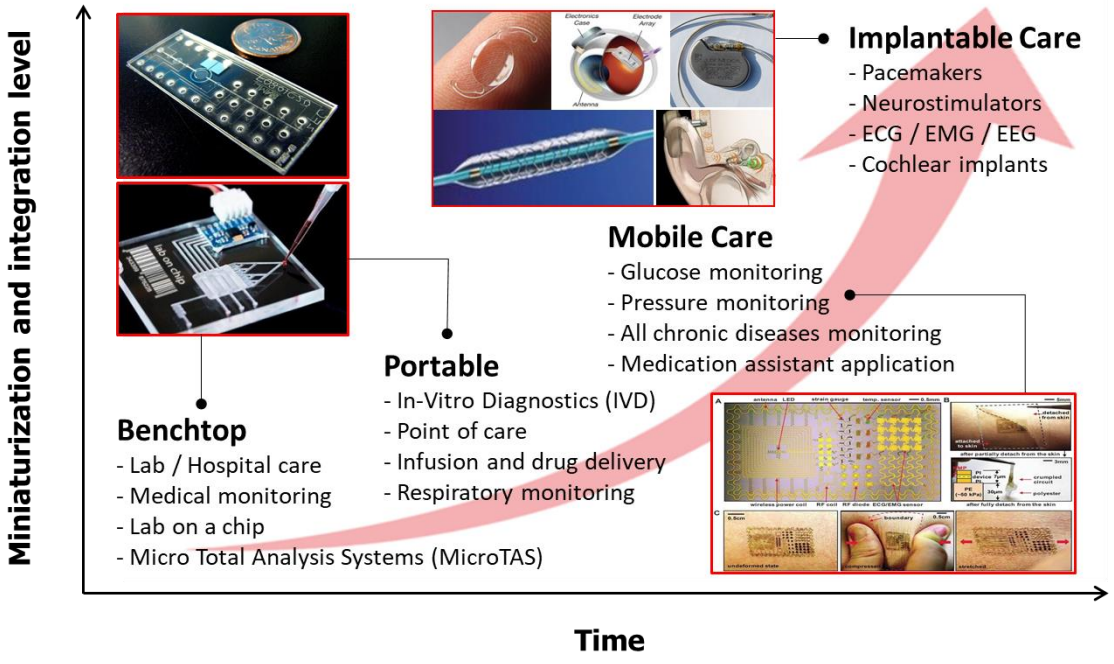

Figure 1.3. Development of Bio-MEMS in terms of its miniaturization and integration level.

Bio-MEMS can be used not only in various fields of medicine and biology, but also can create high added value, so it is possible to produce individual products for specific purposes. Major application fields of Bio-MEMS include biomedical engineering field, bio chip field including DNA chip, protein chip, and cell chip, and lab-on-a-chip field based on microfluidics. Bio-MEMS technology is a new technology with high technical level of difficulty, technology ripple effect, and economic and industrial value, and can be said to be a tool that enables the life science revolution of the 21st century (Lo, 2008) (Kim, 2011).

BioMEMS has the potential to provide many future tools for life sciences in combination with microfabrication techniques, low-power integrated circuits and biomaterials. The scope of research on the BioMEMS can be limited to product purposes including diagnostic microsystems, therapeutic microsystems, surgical applications and implantable devices. The most representative diagnostic device in the BioMEMS technology is point of care (POC) diagnostic microsystems. Such microsystems are known as μTAS (micro Total Analysis Systems) or LoC (Lab-on-a Chip) devices and used to characterize biological samples and run full diagnostic tasks. In order to produce fast and accurate diagnoses, multiplexing of the tests is required, for which each step can have different MEMS components such as cell separation, cell lysis and detection elements (Au, 2011). For the therapeutic BioMEMS devices, majority of components and devices developed for drug delivery are microneedles and drug reservoirs. These devices have been designed to provide painless, patient-friendly and effective drug release into the human body with a controlled dosage and built with MEMS manufacturing techniques as well as biology and materials research to optimize the drug delivery

systems in the human body (Ziaie, 2004). BioMEMS technology for surgical applications has evolved to reduce surgical trauma by reducing postoperative pain and recovery time using minimally invasive methods and new biomedical tools. Representatively, MEMS technology can downscale surgical devices to the size of individual cells with high spatial resolution: surgical grippers, tweezers, scissors in micro scale (Polla, 2001), and it allows surgeons to access inaccessible body areas with minimal surgical trauma. Furthermore, the advancement of MEMS sensing technology allows to enhance tactile sensation and reduce the scale of endoscopy systems to fit into a drug capsule by piezoelectric sensors for tactile sensing and image sensors & telemetry units for endoscopy (Saliterman, 2006). BioMEMS devices play an important role also in implantable devices in a device miniaturization approach with high flexibility and biocompatibility. For instance, currently, a lot of researchers are focusing on development of miniaturized devices that stimulate or record nerve signals while reducing potential damage to tissues. In addition, a variety of related technologies are additionally required for more complex and sophisticated sensing functions: integration with circuitry for signal amplification, wireless transmission of power, bidirectional data transmission, etc., which can be developed by MEMS technology (Saliterman, 2006). Biocompatibility is also a critical factor which should be considered for implantable devices. For this reason, various polymers such as polymide, parylene, and PDMS are being studied to prevent unexpected interactions with the human body (Velten, 2005).

Depending on the product types, BioMEMS can also be categorized by microfluidic chips and sensor-type devices for medical and healthcare applications worldwide. First, microfluidics refers to systems that manipulate small amounts of fluids

on microfabricated substrates, such as a glass, silicon, PDMS, etc., including microchannels and patterns fabricated by etching or molding techniques. Microfluidic engineering is an innovative technology in the biotechnology and medical industries. Its cost-effective, easy-to-manufacture and user-friendly features make it a leap forward in healthcare. By using this, pre-processing for analysis, such as sample pretreatment and manufacturing, can be performed on a single chip. Therefore, methods such as DNA analysis and proteomics have changed significantly through microfluidic devices, bringing about fundamental changes in pharmaceutical and life science research areas such as drug delivery and in vitro diagnosis. The main factor in this significant development is the need for rapid disease diagnosis in the medical field and simple in vitro diagnosis in daily life is increasing. In particular, the microfluidics field occupied the largest share in the BioMEMS market: 72% in 2017, 85% in 2020. The global market of microfluidics was valued at $13.5 billion in 2019 and is expected to record an annual average growth rate of 11.3% over the forecast period. The growing demand for Point-of-Care (POC) devices is expected to drive the market significantly (MordorIntelligence, 2019). In the coming years, the market is also expected to develop further due to the demand for high-throughput screening methodology, small sample analysis, in vitro diagnostics (IVD) and the development of advanced lab-on-a-chip technology. For example, the growing demand for next-generation sequencing applications is a major factor in driving the growth of the bio-MEMS market for microfluidic chips (MordorIntelligence, 2019). The applications of next-generation sequencing are expected to advance significantly in the near future, which could create more demand for microfluidic chips.

For the sensor-type BioMEMS devices, pressure sensors are the most representative sensor devices used for respiratory and blood monitoring, still reaching hundreds of millions of units per year. In the future, pressure sensors are still expected to continue to have high interest from research and industry fields due to new demand for smart connected entities such as inhalers and sleep apnea monitoring systems. The areas with the highest growth expected over the next five years are micromechanical ultrasound sensors (MUTs) for medical imaging and inertial sensors for fall detection and activity tracking. In recent years, along with changes in global healthcare, medical devices with new diagnostic functions using gas sensors and micro-machine ultrasound transducers (MUT), such as capacitive micromachined ultrasound transduces (CMUT) and piezoelectric micromachined ultrasound transducers (PMUT), are being developed. BioMEMS sensors have led to the advancement of healthcare market providing a better quality of life (Grayson, 2004).

In particular, the global healthcare market has grown significantly in recent years in an effort to diagnose or overcome the corona19 pandemic. BioMEMS areas used in the development of COVID-19 antibodies, including non-face-to-face thermometers and diagnostic kits, are expected to show high growth rates in research and industry fields. Just as life around the world has changed since COVID-19, the healthcare market has also changed, and the infectious disease has hit the fields of medical devices and in-vitro diagnostic medical devices (IVD), and has had a great impact on sales as well as application and use. Representatively, AbCellera, a Canadian biotechnology company, has developed microfluidic MEMS for the development of COVID-19 antibody therapeutics. First, the immune cells that make antibodies are isolated from the blood of

convalescent patients rich in Corona 19 antibodies. Here, AbCellera has developed microfluidic chips that can isolate one immune cell and confine it in small reservoirs (Knapp, 2020). If antibody treatments are found to be effective in the treatment and prevention of COVID-19, they are expected to be useful in the development of treatments for COVID-19 as well as other new infectious diseases. It is one of the major achievements of BioMEMS technology.

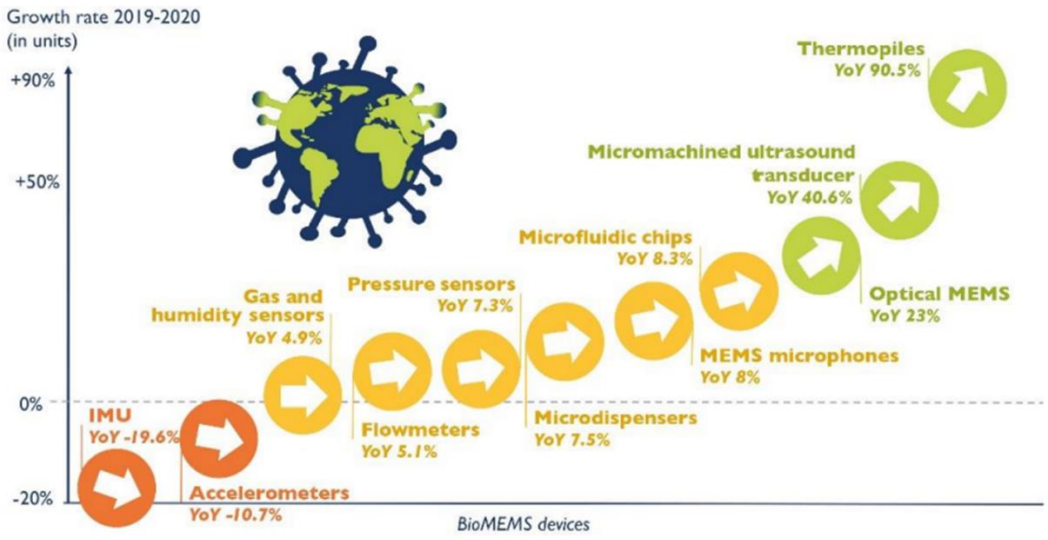

Figure 1.4. COVID-19 impact: the different BioMEMS devices growth rate between 2019 and 2020. Due to the COVID-19 outbreak, the BioMEMS market has been shaken greatly by a number of complex factors that mix negative and positive factors. As a result, the overall BioMEMS market is expected to grow 12.4% from 2019 to 2020. Although the impact of COVID-19 on each specific application will not be the same, in the medium to long term, connected wearables and point-of-care medical devices will amplify more interest in the healthcare sector. The pandemic has had a profound impact on the medical

device and In-Vitro Diagnostics (IVD) fields, affecting the public's interest in healthcare, as well as applications and uses (YoleDevelopment, 2020).

After the successful development of the BioMEMS technology, the expected health care impact is enormous: early disease diagnosis, reduced physical trauma, and more accessible health care monitoring and delivery at a lower total cost. Lab-on-a-chip will enable rapid diagnosis at low cost in developing countries and even remote locations. Furthermore, the technology used to fabricate the BioMEMS device is closely related to the development of micro / nanotechnology. In the future, as microfluidics and microelectronics converge, and technologies using new materials such as carbon nanotubes and graphene are introduced, new devices are expected to be developed in more various fields.

1.3. Implantable BioMEMS Applications

The beginning of traditional implantable electronics goes back 60 years. In 1959, Mackay Noller and his colleagues began research to develop a radio transmitter that carries physiological information within the human body, primarily in the gastrointestinal tract. Since then, other researchers have integrated biometric telemetry devices to measure information about human organisms in various body cavities. The first major generation of implantable biotelemetry appeared in the 1960s, it measured cardiovascular, respiratory, nerve activity and gastrointestinal activity. In the late 1970s, biotelemetry technology evolved at a very rapid pace, ranging from pacemakers, nerve stimulators, insulin dispensers, and even sports medicine applications such as intracranial

pressure (ICP) monitoring (Ko, 2012). In particular, the miniaturization and development of biomedical implantable devices has advanced with the development of BioMEMS including IC technologies, robotics, power and energy harvesting. Advances in MEMS technology have made it possible to use smaller, lighter, and versatile electronic devices. For instance, a shrinking race for transistor size began with the proliferation of clean room facilities in the 1960s. Then, Intel adopted 10 μm manufacturing technology in 1971, now, in 2020, they applied 7 nm linewidth technology to diverse applications. The resulting reduction in electronic circuit size has had other benefits in battery life and capacity. In 1973 Greatbatch and Holmes developed a lithium-iodine battery, which has good properties for use in smaller and lighter electronic systems such as long life, low power consumption and constant voltage output (Greatbatch, 1991). Since the invention of the lithium battery in 1973, much research and studies have been conducted. But nevertheless, batteries for implanted devices haven't changed much since then. However, a number of studies on alternative methods of transferring energy to implants are being conducted steadily with advanced MEMS technologies, and mainly focused on energy harvesting methods and fully-passive wireless methods (Suzuki, 2011). The recently reported studies, such as glucose biofuel cell research and fully-passive wireless neural sensors, set a new direction that will enable the next revolutionary step in powering implantable devices (Slaughter, 2015).

As mentioned in the previous chapter, the fields of application of BioMEMS can be used for diverse fields, and it can be largely divided into medical (clinical diagnosis), pharmaceutical, environmental, food, military and research use. The characteristics of the BioMEMS industry are slightly different depending on the application field. The field

with the most demand for BioMEMS devices is in the medical sector, and medical devices are expected to serve as a driving force for the growth of the BioMEMS industry in the future. Especially, the implantable segment held the largest market share, accounting for nearly 80% of the market. The market share for this product is expected to increase nearly 6% by 2022. The injectables segment is also expected to register a growth of nearly 5% by 2022 (Technavio, 2018). This is because the size and sensitivity of BioMEMS devices are well suited for cell-level applications, so many implantable surgical devices have been developed using BioMEMS technology to perform advanced diagnostics and therapeutics.

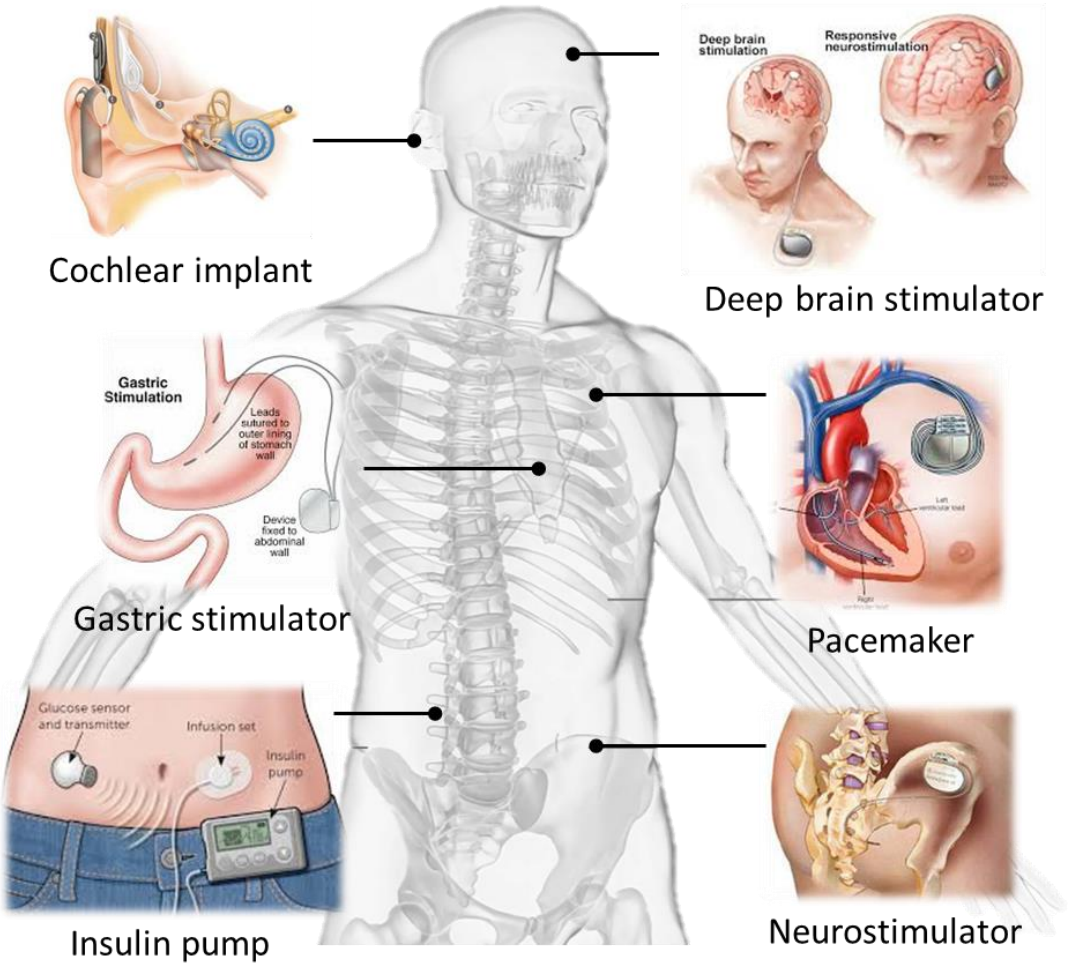

Figure 1.5. Examples of implantable devices. Implantable medical devices are designed to assist or replace certain physical activities by being placed inside the body through a medical procedure and maintained after the procedure. With the advancement of science and engineering technology, implantable medical devices have been developed and improved a lot. Examples of implantable devices include pacemakers, implantable cardiac defibrillators (ICD), neurostimulators, coronary stents, hip implants, cochlear implants, and implantable insulin pumps. The development of such medical devices will continue with the entry of an aging society and the development of various new science and technology, and this will increase the interest of not only medical personnel but also the general public.

Among the various types of implantable devices, cardiovascular implants dominate the market for implantable devices. The invention of the electrocardiogram (EKG) to record the electrical activity of the heart in 1903 was critical in the development of modern cardiovascular medicine. In addition, advances in hydrodynamics and cardiac physiology made it possible to perform the first artificial heart valve transplantation with an external pacemaker in the early of 1950s, and thus the heart itself was one of the first to benefit from implantable technology. In 1960s, as mentioned earlier, the development of transistors took place, and made it possible to fully implantable electronic devices. Advances in these technologies were rapidly applied for the development of fully implanted pacemakers, first tested on animals in 1958 and then successfully performed in humans for the first time in 1960, turning the pacemaker into the first implantable electronic device (Kim A. e., 2015). Subsequent developments have

spurred research into biocompatible materials, electrodes and rechargeable light batteries. And today, modern pacemakers are often integrated with defibrillators that function to reset the heart rate if the heart stops.

Another representative implant device to which BioMEMS is applied is a neural probe device for brain medicine / science. Further developments in MEMS technology, along with active research on action potential mechanisms, have made it possible to develop neural probes that can operate in the human body. For example, when the brain generates electrical signals for certain physical activities, the transmitted neurons are captured by implanted neural probes. Then, implanted electronic devices and signal processing algorithms allow the person to move his robotic arm or leg to perform tasks that are normally performed by natural limbs. This process is called BMI (a brain-to-machine interface), and currently, the external robotic prosthetic technology is advancing rapidly by implementing improved brain-machine interfaces and new materials, which allows the prosthesis to be seamlessly integrated into our body (Cheung, 2006).

In addition to detecting activities related to body kinetic function, neural probe interfaces are widely used to activate physical or neural activity by stimulating other areas of the brain. A lot of researches have been actively conducted to stimulate the auditory nerve or the optic nerve by implanting a probe in the inner region of the brain. In 1987, a deep brain stimulation technique for treatment of Parkinson's disease was developed by A.L. Benabid (Benabid, 1987). After that, the technique has widely been applied in the field of deep brain neurosurgery to treat Tourette syndrome, chronic pain, major depression, and obsessive-compulsive disorder.

Cochlear implants, which have been in clinical use since 1977, are considered one of the most successful commercial implants to date. The general operating principle is that the microphone and sound processor are mounted externally. Then, it uses a short-range wireless communication channel to transmit the processed information to an internal implant that provides adequate stimulation to the electrodes inside the cochlear implant. As a result, electrically stimulated auditory nerves allow the brain to interpret incoming sounds. The current technical stage is at a level that can help people hear voices, not for listening music or nature sound. However, with the advancement of MEMS technology, other mechanisms for stimulating the cochlear nerves, such as the use of a series of laser pulses within the inner ear and the use of photoacoustic effects, are constantly being studied (Wilson B. S., 2003).

Visual prostheses research is closely related to the development of cochlear implant models. For the working mechanism, images are digitized and electronically processed using an external camera, and implanted electrodes stimulate the retina by using the digitized image data. The optic nerve then transmits the information to the brain, interpreting the artificially generated signal as a low-resolution image. Today, state-of-the-art experimental bionic eye systems use thousands of electrodes (Luo, 2014), but due to the relatively low resolution black and white images, still many further improvements are required to achieve the resolution required, for example for reading a book.

Implantable systems are inevitably prone to many types of errors in mechanical, electronical and biological aspects. This is mostly because non-biological materials used for electronics, electrodes and device packaging in the in-vivo environment are

eventually corrosive. Therefore, long-term interaction with the human body is the most important factor to consider in the deterioration of implant material performance and ultimately system failure. In addition, the design and technical limitations of implantable systems related to physiology and pathology are areas that need continuous development. Nevertheless, implantable systems are still being developed with high expectations that we can conquer the mysteries of the human body and even reach new technological revolutions in the future. For example, with the rapid development of BMI, we will be able to live in a world where people can wear their artificial eyes, noses, or ears for their own taste or business reasons and control the machines as they think in their mind, as seen only in science fiction movies.

1.4. Artificial Organs Technology: a Hydrocephalus Treatment Example

One of the important goals of BioMEMS is to develop and put into practice technologies that will maintain, improve or restore the functioning of diseased organs. Artificial organs are engineering tools that are partially transplanted into living human organs or separate units to replace human organs that suffer from malfunction or complete loss of function. Especially recent advances in MEMS technology have brought biomedical devices and artificial organ development technologies closer to a level where they can enhance or replace organ function. Devices consisting of artificial synthetic components, for example called "bio-hybrid organs" can be combined with sensors, new biomaterials and advanced delivery systems to replace the original organ role. Artificial organs take over the unique functions of natural organs, allowing patients to return to a healthy life. Until now, artificial organ devices have been used to restore the

health of patients by replacing their core functions in the lungs, heart, liver, kidneys or nerve sensory organs.

Today, there is a growing demand for these technologies. According to a report released by recent statistics (FiorMarkets, 2020), the global wearable artificial organ market is expected to grow at a CAGR of 16.20% by 2027 (It is expected to reach $5.26 billion in 2019 to $17.4 billion in 2027). This is because the market is growing as the number of patients with organ dysfunction increases and the imbalance in supply and demand for organ donors is growing. In addition, technology and investment in research and development activities for implantable / wearable artificial organs are also developing along with the growth of the market. Advances in microelectronics, nanotechnology, artificial intelligence, genetic engineering, stem cells, and bioinformatics are paving the way for the artificial organs (Onuki, 2008). The use of artificial organs is also cheaper than organ transplants in terms of cost, creating new opportunities and demand in the market. And with the advancement of traffic, even the high incidence of many permanent injuries and road accidents is a major reason for the growing demand for artificial organs. Many companies in the industry are also leading the development of artificial organs for diseases that cannot be treated with modern medical technology. For patients with kidney failure, for example, commercial wearables and portable artificial organ devices can be used to provide simple treatment and dialysis in everyday life, which can improve long-term quality of life (Huff, 2020).

In particular, the recent trends in the development of artificial devices are moving beyond simple mechanical organ function replacement to organ recovery and biological replacement that operate as tissue-based artificial organs and simulate the physiological

function of the organ. These devices are designed and operated to suit the patient's individual environment. Organs transplanted from other people or animals such as pigs carry the inevitable risk of immune rejection, so scientists have already studied similar living organs made of their own cells for the goal of personalized artificial organs, which is called Organoid, for 20 years. Organoids are stem cells or somatic cells removed from the body that have been cultured and grown in an external environment. Even if transplanted, immune rejection does not occur. As such, modern artificial organ devices are moving from mechanical alternatives to more fundamental biological substitutes. Another technique that is currently being studied heavily is the use of 3D printing to create artificial organs. This technology is being applied to the medical world through 3D printing devices such as prosthetics and surgical tools, and research on bio-inks for printing vital organs, bones and cartilage is further intensifying. In the medical field, with the advancement of bio-ink technology, various organs, including the thyroid gland, a tibial substitute that has already been implanted in a patient, and a heart cell patch that actually beats, have been successfully applied using 3D bioprinting technology. This 3D bioprinting method could be the next generation technology beyond organ transplantation. For example, stem cells from transplant recipients can be harvested and printed on replacement organs, which can help reduce complications associated with organ transplantation, such as long waiting for an appropriate donor or immune rejection of new organs.

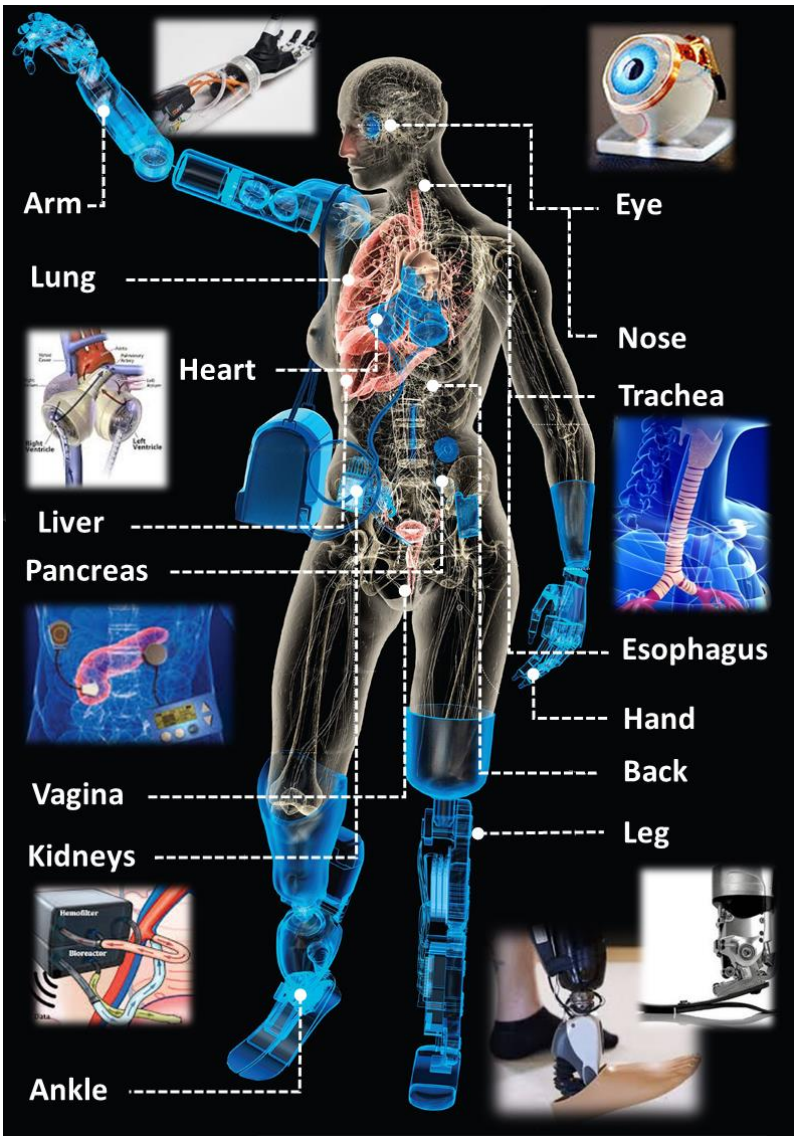

Figure 1.6. Examples of artificial organs. In the future decades later, it may become possible to create and implant new artificial organs. This is because technologies that can create various organs in the body such as the heart and liver as well as various human tissues such as skin and cornea are being studied. For example, the artificial organ technology has been applied in various medical products for heart, limbs, vision, brain, exoskeletons, cochlear implants, pancreas and kidneys. Technologies that can find and treat incurable diseases such as cancer and various chronic diseases are being developed, but

there are many cases in which organ transplantation is absolutely necessary in the treatment method, and it is expected to become the core of future medical care (SuhJeong & ChristieBryan , 2014).

Artificial organ technology has been applied in several medical products for limbs, vision, brain, exoskeletons, cochlear implants, pancreas and kidneys. Among them, the cochlear implant segment is the field where the most actual products are released, and it is recorded the highest share in the wearable artificial organ market at 19.07% in 2019 (FiorMarkets, 2020). Looking at artificial organ devices in real life, in August 2019, FDA authorized MED-EL Cochlear Implant System for children five years and older who suffer from asymmetric hearing loss (FDA, 2019). In December 2019, the FDA approved another cochlear system, which is the first active Osseointegrated steady-state implant for use in children 12 years of age and older with single-sided sensorineural deafness (FiorMarkets, 2020). These artificial organ devices not only improve the patient's hearing ability in daily life, but ultimately help them advance their future lives. In addition to the cochlear devices, other representative fields of artificial organ devices can be classified as vision bionics, orthopedic bionics, cardiac bionics and neuro/brain bionics. In general, for example, there are bionic eyes including artificial corneas for vision bionics; bionic limb, exoskeleton and electrical bone growth stimulators for orthopedic bionics; artificial heart including valves and pumps, pacemakers and ventricular assist devices cardiac bionics; and deep brain stimulator, vagus nerve stimulator, and spinal cord stimulator neural/brain bionics (Bronzino, 2016).

In the case of artificial organ devices for the brain bionics, related research and investments are very active, and the market size is steadily growing (MarketWactch, 2020). However, the types of artificial organ devices or implant devices used for brain diseases are still very limited because unlike other parts of human organs, the brain is not completely replaceable for obvious reasons; we still don't know how many components are in the brain. And, even the humans have approximately 86 billion neurons in the brain, each with 1,000 connections. As mentioned previously, most of the devices at the actual commercial level are neurological devices such as nerve stimulators that help the brain to perform specific actions by transmitting specific electrical impulses to the nervous system.

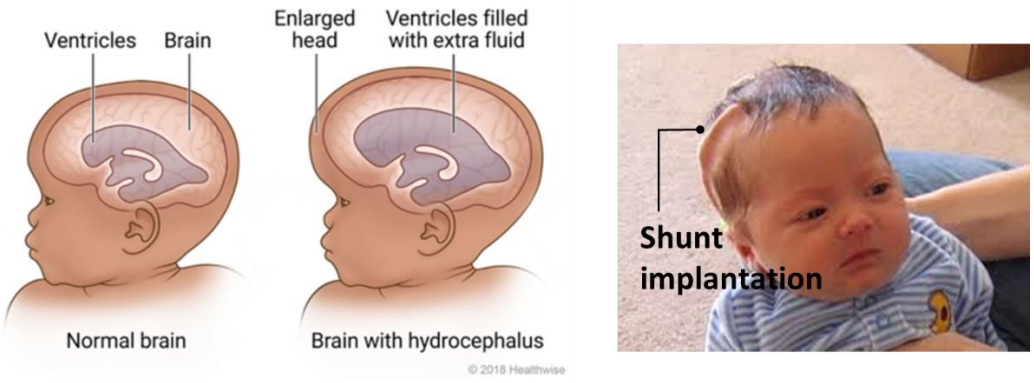

Figure 1.7. Comparison between normal brain and hydrocephalus case (left). Actual case of implantation of a shunt device (right). When the circulatory path of the cerebrospinal fluid is partially blocked for some reason, the cerebrospinal fluid is abnormally accumulated in the cranial or spinal cavity. The accumulation of cerebrospinal fluid leads to an increase in brain pressure in most cases, leading to symptoms and impaired brain development. It is often associated with congenital brain and spinal cord structural

abnormalities, so it occurs a lot in children. There are currently no non-surgical treatment methods for hydrocephalus, the shunt device is the only method for the treatment of hydrocephalus. Shunt surgery is a surgery in which a thin tube is inserted into the ventricle to draw out cerebrospinal fluid and send it to the abdominal cavity through a connected tube, where it is absorbed back into the body through the peritoneum. A valve device is installed in the middle to adjust the amount of cerebrospinal fluid flowing according to the high degree of brain pressure (Fetalhydrocephalus, 2020) (Healthwise, 2020).

On the other hand, there is another brain bionics device, which is the shunt system for hydrocephalus treatment. In order to figure out the shunt device, we must first understand about hydrocephalus. In general, hydrocephalus is an abnormal accumulation of cerebrospinal fluid (CSF) in the cavity of the brain, ventricle. Cerebrospinal fluid circulates through the brain's ventricular system and is absorbed into the bloodstream. If there is an imbalance between the amount of CSF produced and the rate of absorption, hydrocephalus occurs. As a result, as CSF accumulates in the head, the pressure inside the head increases, resulting in a larger head. At this point, the shunt device can be implanted directly into the brain to provide an alternative fluid pathway that bypasses the obstacles blocking the CSF flow. The implanted shunt sends CSF to the ventricles within the brain or to the subarachnoid space around the brain and spinal cord, allowing the CSF to be absorbed in other areas of the body and consequently restore the physiological balance of CSF flow in terms of its production and absorption. However, shunt cannot be a fundamental treatment method for improving the disease because it cannot directly treat the factors that cause hydrocephalus: imbalance between CSF production and absorption.

In addition, within the first 2 years after shunt transplantation, about 40 to 50% of the shunt devices have fatal problems due to various factors, and must be replaced with several additional invasive surgeries. These major complications include mechanical malfunction, natural obstruction, infection, subdural hematoma, and excessive drainage or insufficient drainage (Verrees, 2004).

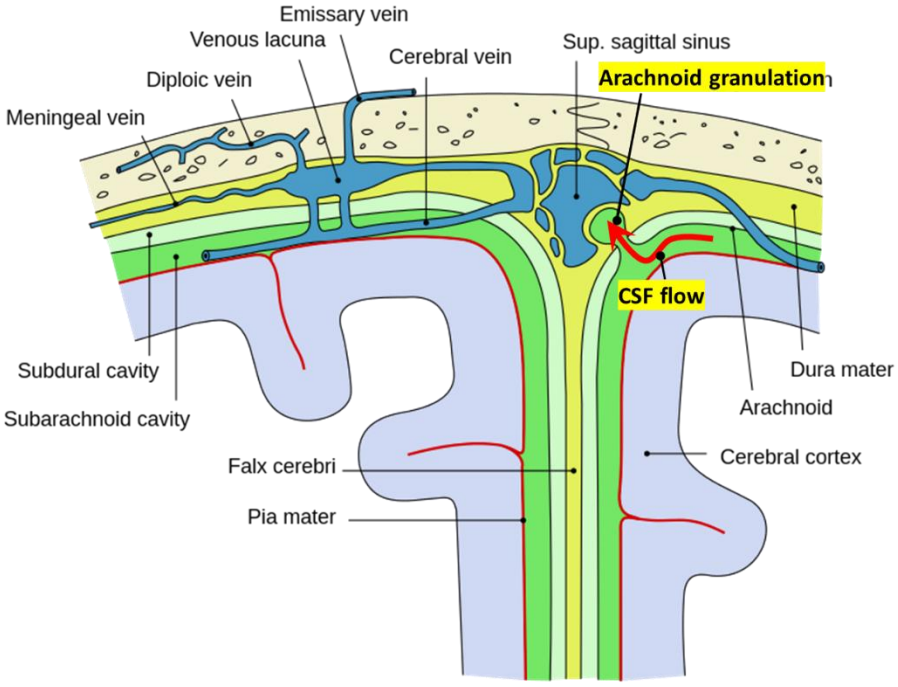

Figure 1.8. Diagrammatic representation of a section across the top of the skull, showing the membranes of the brain (Mysid, 2010). In the case of communicating HCP, the impaired CSF absorption at the arachnoid granulations (AGs) is considered as the main cause as the AGs act as one-way valves to regulate CSF transport. The AGs are natural valve systems of the arachnoid mater protruding into the outer membrane of the meningeal dura mater. They absorb the excessive CSF from the subarachnoid space (SAS) and drain

it to the venous system superior sagittal sinus (SSS) to maintain CSF circulation in a proper range.

In this regard, arachnoid granulation is a key component that handles CSF production and absorption. Arachnoid granulation is a small protrusion of arachnoid material into the epidural membrane. They protrude into the dural venous sinus of the brain, allowing cerebrospinal fluid (CSF) to exit the subarachnoid space and into the bloodstream. CSF returns to venous circulation through diffusion from the arachnoid granules to the upper sagittal sinus. Here, the arachnoid granules regulate CSF on the same principle as a one-way valve. In general, the pressure in the CSF is higher than that in the venous system, so the CSF flows into the blood through the granulations. However, if the pressure is reversed for any reason causing the malfunction of the arachnoid granulation, the CSF will not return to the subarachnoid space. Much research has been done on the cause of the reversal of pressure due to impaired arachnoid granulation, but the exact is not yet known.

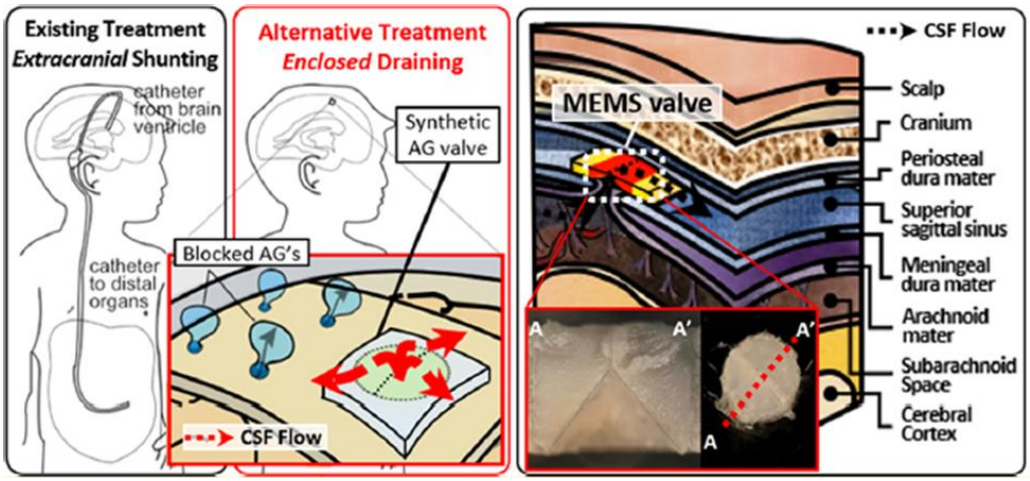

Figure 1.9. Depiction of current hydrocephalus treatment methods (shunts) versus a fully enclosed approach. The fully enclosed approach would eliminate the need for bulky subcutaneous catheters and valves (Lee, 2020). An alternative cerebrospinal fluid (CSF) draining method to treat obstructed CSF flow in hydrocephalus (HCP) when the arachnoid granulations (AGs) fail to regulate the flow. Current commercial shunt systems deliver CSF from the brain to the stomach or other distal organs, so catheterization through repeated craniotomy is essential. However, the miniaturized hydrogel valve is an artificial organ device that directly replaces arachnoid granulations (AGs), replacing the blocked AG's CSF drainage operation and allowing the CSF to circulate as in normal conditions.

Accordingly, many scholars are researching and developing devices that can replace arachnoid granulation with the concept of artificial organs while supplementing the shortcomings of the existing shunt device. And these hydrocephalus treatment devices basically function as passvie check valves, and together with them, they must have the following core functions to completely replace the existing arachnoid granulation: 1) When ΔP (differential pressure applied across the valve) is less than valve opening

pressure P_T ($\Delta P < P_T$), the valve must be in the closed state and completely block the flow of CSF; 2) Depending on the differential pressure applied to the valve, it must have high diodicity or one-way flow, and at the same time completely control the reverse fluid flow; 3) Characteristics of a one-way valve that opens in a specific pressure section, not at zero ($0 < P_T$). Along with these essential properties of arachnoid granules, various types of check valves utilizing MEMS technology have been actively studied for over 20 years, such as cantilever, bridge, perforated membrane or spherical ball type valve. Nevertheless, most MEMS-based valves have yet to fully meet these three essential check valve characteristics with other limitations such as deformation or stiction of valve structure and finite leakage after multiple periods of operation. To overcome many of these failure mechanisms, advanced valve design and fabrication processes are being developed along with newer biocompatible materials research (Lee, 2020) (Schwerdt, 2013) (Schwerdt, 2015). This will be exemplified by the alternative hydrocephalus treatments which will be addressed in more detail in following chapters.

Although the human body has been studied and developed a lot to this day, there are still infinite hidden areas that have not been revealed. Therefore, the need for biomedical devices continues to increase, and research and development of related technologies are also required for the future; in particular, the interest of the biomedical industry worldwide is hotter than ever due to the current outbreak of covid-19. As we have learned so far, the development of biomedical devices has been steadily developed in conjunction with many advanced science technologies along with existing medical technologies. This is because the characteristics of the development of bio-devices essentially coincide with the search for human life, so it can be developed into infinite

applications. In this respect, the application of MEMS technology for biomedical devices is an indispensable trend. This is because MEMS is basically based on the characteristics of device minimization, low power, high integration, and mass production, which are combined with next-generation new technologies, such as wireless communication, new material technology, powerless operation and etc., to produce infinite synergy for biomedical devices. From mobile diagnostic kits to implantable artificial organs, the ultimate goal of next-generation biomedical devices is clear. However, since these devices directly target the human body, there are many strict physical and functional limitations resulting in more complicating working mechanism and relevant analysis compared to other fields. Therefore, more research time and investment are required, and a multi-disciplinary approach is required rather than a single discipline. Nevertheless, it is clear that the improved healthcare / biomedical-related technologies have increased the longevity of the population and will play a greater role in managing end-stage patients by providing long-term support and replacement devices in response to a shortage of donor institutions.

CHAPTER 2

2. 3-DIMENSIONALLY PRINTED MICROELECTROMECHANICAL-SYSTEM HYDROGEL VALVE FOR COMMUNICATING HYDROCEPHALUS

Reproduced with permission from Royal Society of Chemistry. Seunghyun Lee, Ruth E. Bristol, Mark C. Preul, and Junseok Chae. “A 3D-printed MEMS (Micro-Electro-Mechanical-System) Hydrogel Valve for Communicating Hydrocephalus” ACS Sens. 2020, 5, 5, 1398–1404 Publication Date: March 6, 2020 https://doi.org/10.1021/acssensors.0c00181

2.1. Abstract

Hydrocephalus (HCP) is a chronic neurological brain disorder caused by a malfunction of the cerebrospinal fluid (CSF) drainage mechanism in the brain. The current standard method to treat HCP is a shunt system. Unfortunately, the shunt system suffers from complications including mechanical malfunctions, obstructions, infections, blockage, breakage, overdrainage, and/or underdrainage. Some of these complications may be attributed to the shunts’ physically large and lengthy course making them susceptible to external forces, siphoning effects, and risks of infection. Additionally, intracranial catheters artificially traverse the brain, and drain the ventricle rather than the subarachnoid space. We report a 3D-printed MEMS (Micro-Electro-Mechanical-System) based implantable valve to improve HCP treatment. This device provides an alternative approach targeting restoration of near natural CSF dynamics by artificial arachnoid granulations (AGs), natural components for CSF drainage in the brain. The valve, made

of hydrogel, aims to regulate the CSF flow between the sub-arachnoid space and the superior sagittal sinus, in essence substituting for the obstructed arachnoid granulations. The valve, operating in a fully passive manner, utilizes hydrogel swelling feature to create non-zero cracking pressure, $P_T \sim 47.4 \pm 6.8$ mmH_2O, as well as to minimize reverse flow leakage, $Q_O \sim 0.7$ µl/min on bench-top experiments. The additional measurements performed in realistic experimental setups using a fixed sheep brain also deliver comparable results, $P_T \sim 113.0 \pm 9.8$ mmH_2O and $Q_O \sim 3.7$ µl/min. In automated loop functional tests, the valve maintains functionality during maximum 1536 cycles with the P_T variance of 44.5 $mmH_2O < P_T < 61.1$ mmH_2O and negligible average reverse flow leakage rates ~ 0.3 µl/min.

2.2. Introduction

Hydrocephalus (HCP) is a chronic neurological condition, characterized broadly by the malfunctions of cerebrospinal fluid (CSF) flow, absorption and drainage in the brain. CSF is a clear body $_{fluid}$ that flows through the ventricles, surrounds the brain and spinal cord, and representatively functions as; 1) a “cushion” for protecting the brain and spinal cord from external shocks; 2) a “delivery system” for nutrients necessary for brain and removing waste; and 3) a “regulator” to adjust intracranial pressures (ICP) through flowing between the cranium and spine (Verrees, 2004). HCP often occurs by an imbalance between production and drainage of the CSF, leading to excess accumulation of CSF in the ventricles. The accumulating fluid results in abnormal enlargement of the head, compression of the brain, and a variety of neurological symptoms such as headache, vomiting, convulsions and even death (Brodbelt, 2007; Chabrerie, 2002;

Kirkpatrick, 1989). HCP can be classified into communicating and non-communicating HCP depending on the place where CSF blockage occurs. In the case of communicating HCP, the impaired CSF absorption at the arachnoid granulations (AGs) is considered as the main cause as the AGs act as one-way valves to regulate CSF transport. The AGs are natural valve systems of the arachnoid mater protruding into the outer membrane of the meningeal dura mater. They absorb the excessive CSF from the subarachnoid space (SAS) and drain it to the venous system, superior sagittal sinus (SSS), to maintain CSF circulation in proper range (Brodbelt, 2007) (Fig. 2-1(a)).

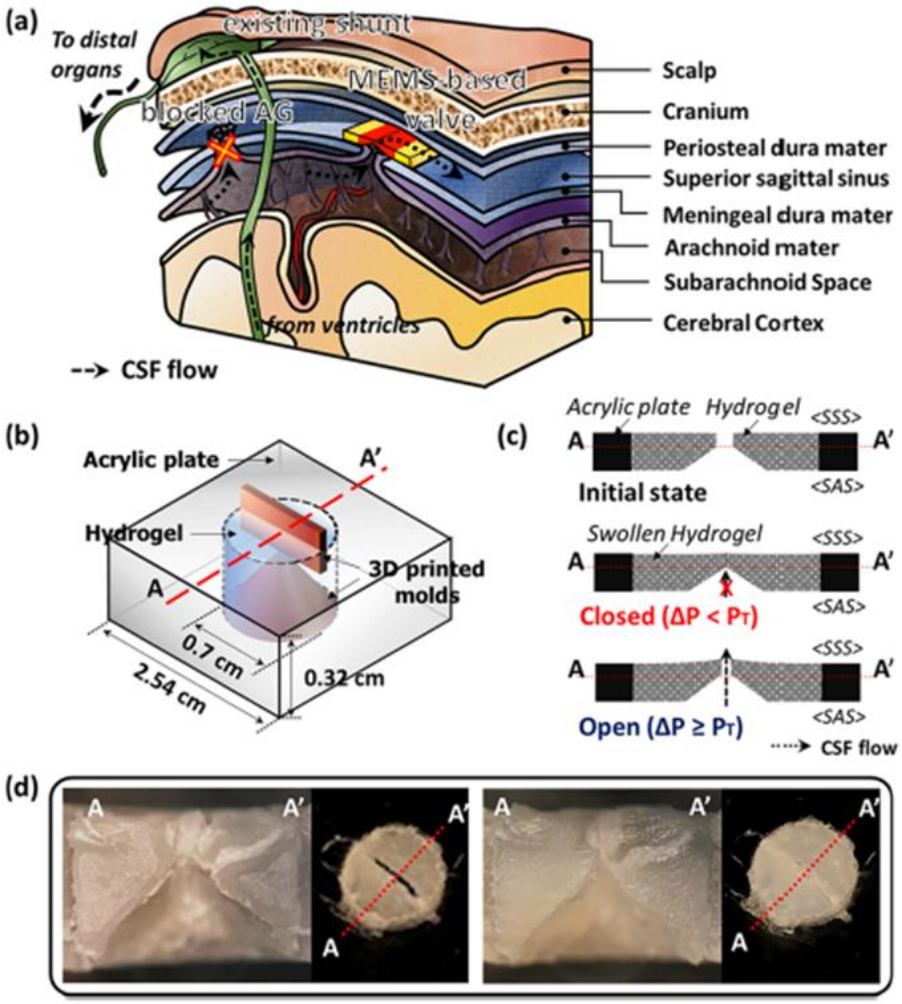

Figure 2.1. Illustration of the alternative cerebrospinal fluid draining methods (MEMS-based valve). (a) Illustration of alternative cerebrospinal fluid (CSF) draining methods (existing shunt system and MEMS-based valve of this work) to treat obstructed CSF flow in hydrocephalus (HCP) when the arachnoid granulations (AGs) fail to regulate the flow. Existing shunts include catheters and a valve to drain CSF outward from the ventricles to distal organs. The MEMS-based valve is implanted directly on the dura mater and directs CSF drainage from subarachnoid space (SAS) into the superior sagittal sinus (SSS). This method of directing CSF allows the CSF drainage process to be confined within the cranium, eliminating the use of catheters that cause many complications. (b) Schematic of the MEMS-based valve fabrication. The valve is composed of a hydrogel and surrounded by an acrylic plate to support the valve structure. 3D-printed molds are assembled in the punctured hole at the center of the acrylic plate then the liquid-state hydrogel is cured inside the hole by UV to be solidified (Figure 2.6). (c) Basic operation of the MEMS-based valve at a cross-sectional view. At the initial state, when the hydrogel is dehydrated, the valve opens to form a fluidic conduit between SAS and SSS. When the hydrogel becomes hydrated, the swollen hydrogel structure closes the hole, forming the closed valve. When the pressure in the SAS reaches higher than the SSS over the threshold, namely, cracking pressure (P_T), $\Delta P > P_T$, the swollen hydrogel valve becomes the open status, and CSF can flow unidirectionally from SAS to SSS. When the pressure at the SAS is lower than that at the SSS by less than P_T, $\Delta P < P_T$, the valve is closed and blocks the CSF flow as the pressure difference cannot open the valve. (d) Photograph of the fabricated 3D-printed MEMS-based valve at the cross-sectional and top view of before (left) and after hydrogel swelling (right).

Standard treatments for HCP involve implantation of a drainage tube, called a shunt, between the ventricles and abdominal cavity or heart, offering an alternative pathway when CSF is accumulated excessively in the ventricles. A shunt typically consists of three major components: an inflow catheter, a valve and outflow catheter. The inflow catheter is inserted to the ventricles to drain excess CSF from the ventricles, and the valve controls the drained CSF flow, which the outflow catheter directs the CSF to the drainage site (Codman, 2014; Drake, 2000; Medtronic, 2012). Shunts are the most popular and primary treatment method for HCP; however, the failure rate is, unfortunately, relatively high, almost 50% within the first two years, thus leading to additional invasive surgeries for replacement (Drake, 2000; Drake J. K., 1998; Reddy, 2014; Stone, 2013). Major shunt complications include shunt malfunctions, infections and obstructions, and most of those complications are associated with catheters such as infection, clogging or breakage (Drake J. K., 1998; Stone, 2013; Czosnyka, 2005; M., 1997).

Catheter-less approaches may be attractive to address these complications and have been explored in the past, including a ventriculosinus shunt (VSS), also as known as the El-Shafei shunt, that directly routes CSF between cerebral ventricles and SSS. The VSS directs CSF to the SSS on the blood stream, taking advantage of the pressure generated by the blood flow in the SSS. However, VSS is neither capable of avoiding reverse flow nor forming non-zero cracking pressure, resulting in headache, nausea, vomiting and papilledema (El-Shafei, 2001; Oliveira, 2017; Van Canneyt, 2008). VSS has not been implanted recently as the efficacy of VSS is questionable in the neurosurgical community (Oliveira M. T., 2015). More recently, Micro-Electro-

Mechanical System (MEMS) technology has been adopted to build miniaturized fluidic valves (S Choi, 2009; R Wang, 2011). Those miniaturized fluidic valves have been extensively researched and developed in various forms such as cantilever, bridge, perforated membrane, or spherical ball type valve (Oh J. K., 2011; Oh K. a., 2006; Chen, 2007; Tiren, 1989; Kim D. a., 2007; Lo R. L., 2009; Moon, 2012; Schwerdt, 2013; Schwerdt, 2015). Critical technical challenges, however, exist: reverse flow leakage (Oh J. K., 2011), valve deformation in long-term operation (Kim D. a., 2007), valve stiction, imperfect sealing (Oh J. K., 2011; Tiren, 1989; Kim D. a., 2007), etc.- involving low reproducibility and durability of the valves. These challenges directly motivate us to study a fundamentally different mechanism of MEMS valve for hydrocephalus treatment.

The work presented here addresses those challenges by using the swollen feature of hydrogel in a custom-made 3D-printed mold. The work aims to direct CSF from SAS to SSS, mimicking AGs, through embedding a unidirectional miniaturized passive valve on meningeal dura mater. The AGs mimicking valve, 'artificial AG', is inconspicuous as it would be concealed within the cranium. The artificial AG directs CSF drainage from SAS into the SSS, thus the CSF draining path is confined within the cranium, eliminating the use of catheters. This approach may mitigate a large proportion of the complications resulted by the catheters - infections, clogging, breakage, *etc*. Our earlier work demonstrated reasonable fluid draining and showed its feasibility as an alternative CSF drainage path (Schwerdt, 2013; Schwerdt, 2015). However, the previous work suffered from low reproducibility and durability due to the manufacturing complexity, deficiency of the accurate measure of fluid pressure across the valve inside of the set-up, and the lack of verification of the valve in realistic environments. This work adopts 3D-printed

molds to significantly simplify the manufacturing complexity and utilizes swollen hydrogel to create non-zero cracking pressure and to achieve negligible reverse leakage. The hydrogel valve shows the CSF flow characteristics within the targeted range at the bench-top and in-vitro settings. The long-term behavior of the valve, through the automated loop functional tests, demonstrates the repeatability and durability of the valve.

2.3. Materials and Methods

Hydrogel. The hydrogel solution was prepared by mixing the base (2-hydroxyethyl methacrylate, Sigma Aldrich), crosslinker (ethylene glycol dimethacrylate, Sigma Aldrich) and photoinitiator (2,2-dimethoxy-2-phenylacetophenone, Sigma Aldrich) at the ratio of 1 : 0.04 : 0.1 respectively (Schwerdt, 2013; Schwerdt, 2015)**.**

*3D-Printed molds***.** The tapered hydrogel structure was fabricated using 3D-printed molds (Fig. 2.6). The models used in this work were designed in Autodesk's Fusion 360 and were printed on the Ultimaker 2 Go 3D printer. The Ultimaker 2 Go has a positioning precision of 12.5 µm and 5 µm in the horizonal and vertical directions, respectively. The 3D molds were put into the hole drilled at the center of the acrylic plate, and then prepared liquid-state hydrogel was poured into the hole. The liquid-state hydrogel was cured by UV crosslinked at ~ 400 mJ/cm^2, then the solidified hydrogel was easily disassembled from the 3D molds.

Bench-top set up. The basic functionality of the MEMS-based hydrogel valve was evaluated by the bench-top fluidic circulatory setup (Fig. 2.7). The bench-top tests were performed to ensure that the valve operates within the targeted fluidic requirements, set

by the specifications of AGs. The setup consists of the hydrogel valve, a fluid source and pressure & flow rate sensors (Fig. 2.7). The fluid circulatory system consists of fluid column (a graduated cylinder), syringe pump (Model 33, Harvard Apparatus) and peristaltic pump (P-70, Harvard Apparatus). Resistive pressure sensors (PX26-001DV, Omega) have 1 mmH_2O resolution, which were calibrated for the actual experiments by a customized setting (Schwerdt, 2013; Schwerdt, 2015). All data were recorded by a data acquisition board (NI USB 6216, National Instruments) and Signal express.

Long-term valve testing was performed by automated loop testing setup using two water columns (1000 mL gradient cylinders), regulating fluidic flow between the two columns, where the valve connects. The fluidic flow generates forward and reverse flows periodically, controlled by a programmable peristaltic pump, as a function of forward/reverse flow, the number of flow cycles, and flow rate. The duration of forward/reverse cycles were set by a few initial trials. The pressure and flow rate across the valve were measured by corresponding sensors to evaluate the valve performance.

In vitro set up using a fixed sheep brain. In-vitro evaluation setting for the valve was built on a fixed sheep brain (Bio corporation). The sheep brain was enclosed by PDMS molding to form a water-tight environment. The valve was placed on designated points of dura mater, where we manually punctured through, and excessive cut was sealed by PDMS to prevent any leakage. CSF was injected to the cavity created by the valve and SAS and the differential pressure across the valve was measured by a pressure sensor.

Cerebrospinal fluid preparation. CSF was collected from hydrocephalic patients at Phoenix Children's Hospital with approved materials transfer agreement (MTA). The

CSF solutions were from an aggregate of multiple CSF bags and maintained in a 4°C environment when not in use.

2.4. Results

3D-printed hydrogel valve. The hydrogel structure has a slit-shaped tapered channel to allow unidirectional fluid flow upon open and close (Fig. 2.1). The detailed fabrication process is described in Fig. 2.6. The unidirectional flow is established by the tapered channel configuration, requiring asymmetrical force to open the valve. When the hydrogel is swollen, due to the liquid absorption, the hydrogel incurs a pre-induced sealing force, establishing a non-zero P_T for opening the valve. This swelling feature combined with the tapered channel configuration provides two main flow characteristics: non-zero cracking pressure and little reverse flow leakage. When the differential pressure between SAS and SSS is less than the cracking pressure, $\Delta P < P_T$, the valve effectively seals the tapered channel to prevent fluid outflow (closed state). When the differential pressure is larger than the cracking pressure, $\Delta P > P_T$, the fluid pressure overcomes the swollen hydrogel resistance, thus the fluid flows through (open state).

The valve dimension was determined and designed by considering the SSS size of the human skull first; the valve needs to be comparable or smaller than SSS for actual implantation. SSS has mean diameter of 7.3 ~ 8.8 mm (Boddu, 2018), thus, we aimed to fabricate the valve with 7 mm diameter. The normal ICP in human ranges -100~350 mmH_2O, and it increases to > 500 mmH_2O for hydrocephalus patients. The valve aims to operate at the range of $-200 < \Delta P < 600$ mmH_2O (Chabrerie, 2002; Czosnyka, 2005; M.,

1997). The target cracking pressure, P_T, is 10–230 mmH_2O and the maximum allowable leakage is set to be 50 µl/min (Chabrerie, 2002; Drake J. K., 1998).

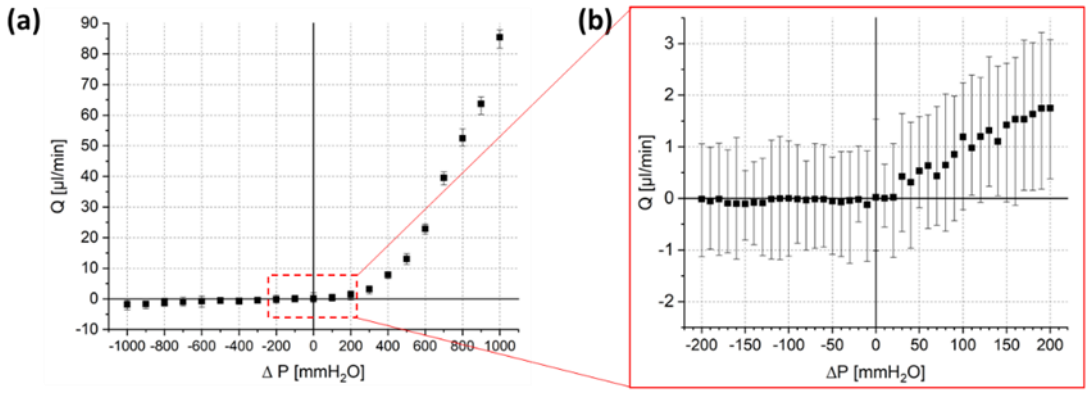

Figure 2.2. Hydrostatic responses of the valve. (a) The valve demonstrated high diodicity without any noticeable reverse flow leakage in the range of pressure across the valve, $-1000 < \Delta P < 1000$ mmH_2O. The reverse flow leakage marked ~0.7 µl/min on average, thus is negligible. Error bar: min to max (b) Close up in $-200 < \Delta P < 200$ mmH_2O. P_T is 47.4 ± 6.8 mmH_2O, calculated by extrapolated linear line on x-axis.

Hydrodynamic valve characteristics on bench-top setup. The basic flow response of the hydrogel valve was measured in the bench-top fluidic circulatory setup shown in Fig. 2.2 (a) and (b). A syringe pump of 450 µl/min flow rate, the average CSF flow rate in human brains ($200 < Q_O < 700$ µl/min) (Torchilin, 2014), drove a wide range of pressure ($-1000 < \Delta P < 1000$ mmH_2O) across the valve. The valve showed highly-directional hydrostatic response, demonstrating high diodicity with little reverse flow leakage within the pressure range (Fig. 2.2 (a)). The output flow rate of the valve increased up to 85.5 µl/min in forward flow direction (0 to 1000 mmH_2O), and very low,

< 0.7 µl/min, leakage was observed in reverse flow (-1000 to 0 mmH_2O). Fig. 2.2 (b) shows the hydrostatic response zoomed in $-200 < \Delta P < 200$ mmH_2O, and the P_T is 47.4 ± 6.8 mmH_2O, determined by calculating the slope from a fitted linear regression model based on pressure-flow rate data for $Q_O > 0$. The hydrostatic measurement was also performed by pressure source, a water column, to verify the consistent operational behavior of the valve regardless of flow rate or pressure sources. The limited resolution and response time of the sensors resulted in finite uncertainty on exact cracking pressure, leading us to perform by small-step increase of pressure (10 mmH_2O) to obtain more accurate P_T (Fig. 2.8). The measured P_T and leakage flow were 42.8 ± 5.3 mmH_2O and < 0.4 µl/min, respectively. Both P_T and leakage flow from syringe pump and water column settings showed very close to each other.

Long-term functional *tests.* The valve is expected to perform within the target specifications for a long period of time inside the brain to avoid additional invasive surgeries. It is, however, challenging to evaluate the long-term valve functionality in a truly realistic setting. Literature shows a single forward / reverse cycle corresponds to one-day operation of the valve based on the assumption that the direction of CSF flow changes once a day, depending on the body position change (Klarica, 2014). We performed repetitive sequences of forward / reverse cycles, controlled by a programmable pump, to evaluate the long-term feasibility of the valve function, by monitoring each cycle of hydrostatic characteristics of the valve (Fig. 2.3). The programmed peristaltic pump controlled the pressure, applied across the valve, in the range of $-50 < \Delta P < 300$ (Klarica, 2014). One cycle of forward / reverse flow was timed at 5 minutes. The hydrogel valve, device under test 4 (DUT 4), maintained relatively-constant cracking

pressure and little reverse flow leakage for 1536 cycles (Fig. 2.3 (a)), at 44.5 < P_T < 61.1 mmH_2O and < 0.3 µl/min, respectively, during the repetitive test (Fig. 2.3 (b)). The detailed analysis of the damages is described later in this section (Future work & Figure 2.5). After the 1536th run, the valve started showing significant leakage due to damages at the hydrogel of the valve structure. We also performed repetitive tests using multiple devices to show the valve durability and reproducibility (Fig. 2.3 (c), (d)). 4 out of 5 devices (DUT 1,3,4,5) have over 1000 cycles of runs (Min. 1104 ~ Max. 1536), which suggest the valves operate for over 1000 days. DUTs showed reasonable P_T and reverse flow leakage during the repetitive tests in the range of 40.3 ~ 53.2 mmH_2O and 0.2 ~ 0.5 µl/min, respectively.

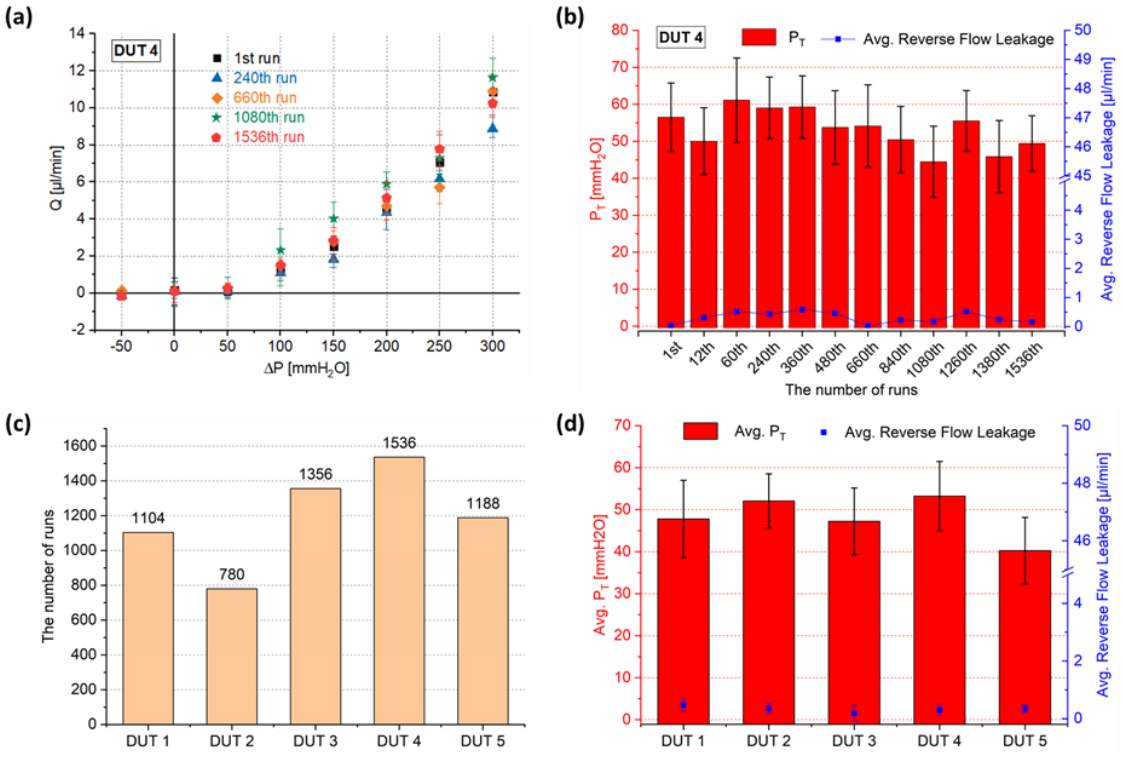

Figure 2.3. Automated repetitive tests for the evaluation of valve's long-term functionality.

Automated repetitive tests were performed by a programmable peristaltic pump to evaluate the valve's long-term functionality. One run consists of flow response measurements in forward and reverse flow and is analogous to one-day operation of the valve (Klarica, 2014). (a) The hydrostatic characteristic of the valve (DUT 4) shows diodicity behavior with negligible reverse flow leakage throughout 1536 runs. The target cracking pressure and leakage flow rate are $P_T \approx 10 \sim 230$ mmH_2O and < 50 µl/min, respectively. Error bar: min to max (b) P_T and reverse flow leakage of DUT 4 over 1536 runs. The measurements show the valve functions consistently at $44.5 < P_T < 61.1$ mmH_2O and reverse flow leakage of < 0.3 µl/min. Error bar: standard deviation (c) The results of the automated repetitive tests of 5 devices. 4 out of 5 devices (DUT 1,3,4,5) marked >1000 cycles of runs, which suggests the valves operate for over 1000 days. (d) Average value of P_T and reverse flow leakage of the devices during the repetitive tests. The devices show P_T and reverse flow leakage in the range of $40.3 \sim 53.2$ mmH_2O and $0.2 \sim 0.5$ µl/min, respectively. Error bar: standard deviation

Hydrostatic Characteristics on a sheep brain setup. The valve was evaluated in a fixed sheep brain (Fig. 2.4 (c), (d)). The meningeal layer was cut to fit the valve between SAS and SSS. The fixed sheep brain did not come with the skull or intact meninges; a sheep brain tends to be easily deformed, causing a technical challenge to implant the valve. Thus, we casted the entire brain in PDMS to form a water-tight seal with the valve implanted. Pressure sensors measured the inlet and outlet pressure of fluidic ports. The inlet fluidic port directly connected to the SAS cavity and a syringe pump injected CSF at 450 µl/min (average flow rate of CSF in human brain is 200 ~ 700 µl/min (Torchilin,

2014)). The CSF passed through the valve when the pressure across the valve exceeds P_T of the valve. Another pressure sensor monitored the differential pressure between inlet and outlet fluidic ports to ensure the pressure measurements were all correct. The hydrostatic response of the valve from the fixed sheep brain, as shown in Fig 2.4 (b), shows flow rate of up to 98.5 µl/min at 0 ~ 1000 mmH_2O, P_T of 113.0 ± 9.8 mmH_2O, and reverse flow leakage of 3.7 µl/min at -1000 ~ 0 mmH_2O. The measured P_T is higher than that of bench-top evaluation because the valve was placed on the thin flexible dura mater, possibly leading to the attenuation of pressure on the valve.

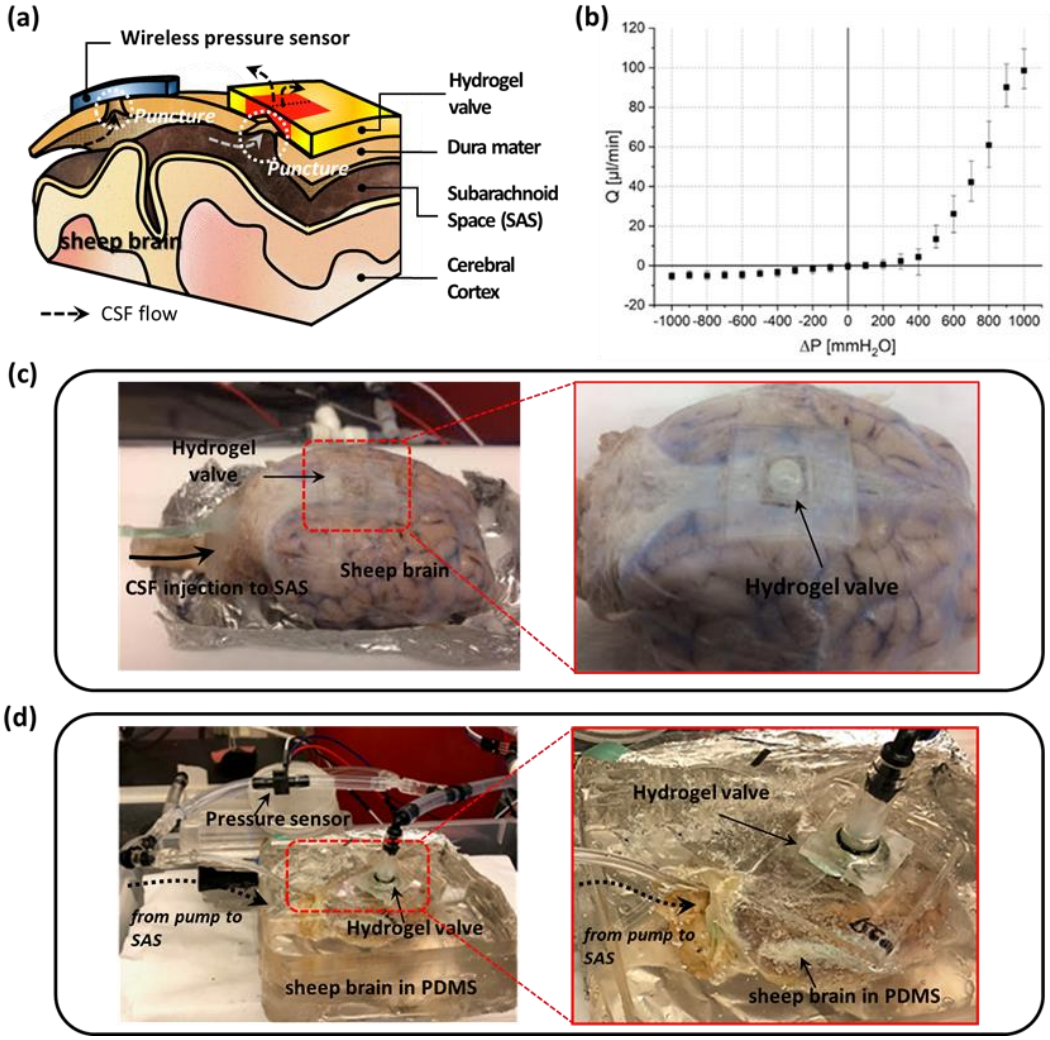

Figure 2.4. The functional test of the hydrogel in a sheep brain model. The hydrogel valve was evaluated in in-vitro setting using a fixed sheep brain. (a) Schematic of the experiment setup. The valve was located onto the designated points of dura mater, where we manually punctured through. (b) Hydrostatic responses of the valve on a sheep brain, showing excellent diodicity and little leakage flow. The valve showed flow rates of 0 ~ 98.5 μl/min and P_T of 113.0 ± 9.8 mmH_2O and < 3.7 μl/min on average leakage flow. Error bar: min to max (c) Photograph of the valve on the sheep brain. (d) Actual configuration of the experimental setup. A syringe pump injects CSF to the cavity formed by SAS and the valve.

Excess portion of manual cut was sealed by PDMS to prevent any leakage. Pressure sensor measures the differential pressure across the valve.

Future work. We manufactured a total of 140 devices. Out of them, 27 devices failed to pass the diodicity test, resulting in large reverse flow leakage. The remaining 113 devices were tested for target hydrostatic specifications and 38 met both target specifications of P_T and reverse flow leakage, which are $10 < P_T < 230$ mmH_2O and < 50 µl/min, respectively. The rest, 75, failed to meet those target specifications. Thus, the total yield is 27%, which was significantly higher than our previous work, having less than 1% yield (Schwerdt, 2013; Schwerdt, 2015).

The failed devices were analyzed to determine the cause of the malfunction. First, the 3D printed molds have finite surface-roughness. The rough surface of the mold may lead to defective valve closing because the hydrogel structure cannot adhere completely, even when the hydrogel is fully swollen. Lowering surface roughness may result in larger contacting area of the swollen hydrogel walls and more controllable one-way flow characteristic, delivering a potential performance improvement, including consistent cracking pressure, controllable flow rate, and minimized leakage flow. More detailed characterization and optimization of the swelling effect may also improve the performance. Second, the hydrogel structure needs to be flexible enough to provide sufficient flow rate for CSF drainage, yet rigid enough to fully block reverse flow of CSF. The non-optimized mechanical property of the structure results in unexpected hydraulic resistance against the flow, resulting in mechanical failure of the structure. Figure 2.5 shows finite element method (FEM) simulation results and photos of a failed

device. The hydrogel valve was partially displaced from the edge, due to the high fluidic stress. This issue can be mitigated by increasing the hydrogel flexibility; however, doing so may cause other issues such as the change of swelling ratio. The adhesion strength between the hydrogel and acrylic surface may be improved. We may deploy intermediate molecules to promote the bonding of the hydrogel as an adhesion-promoting layer (Mateescu, 2012). The hydrogel swelling mechanism is an essential component to achieve the valve functionality and may allow the valve to have different flow behaviors by adjusting the geometry and material property. The study of hydrogel degradation in vitro and in vivo certainly helps understanding failure mechanism of the valve. Therefore, the effect of the hydrogel characteristic to the valve's performance requires more studies, which will remain as future work.

The valve currently has relatively low flow rates, maximum ~ 98.5 µl/min, in the open-status ($Q_O > 0$) compared to the actual CSF out-flow rates, ranging of 0 ~ 350 µl/min in natural range of CSF drainage (Czosnyka, 2005; M., 1997; Vinje, 2019), because the hydraulic resistance of the valve is much higher than that of natural AGs. This issue can only be partially mitigated by implanting multiple valves to generate higher CSF out-flow rates or adjusting the hydrogel characteristics to decrease the hydraulic resistance of the valve.

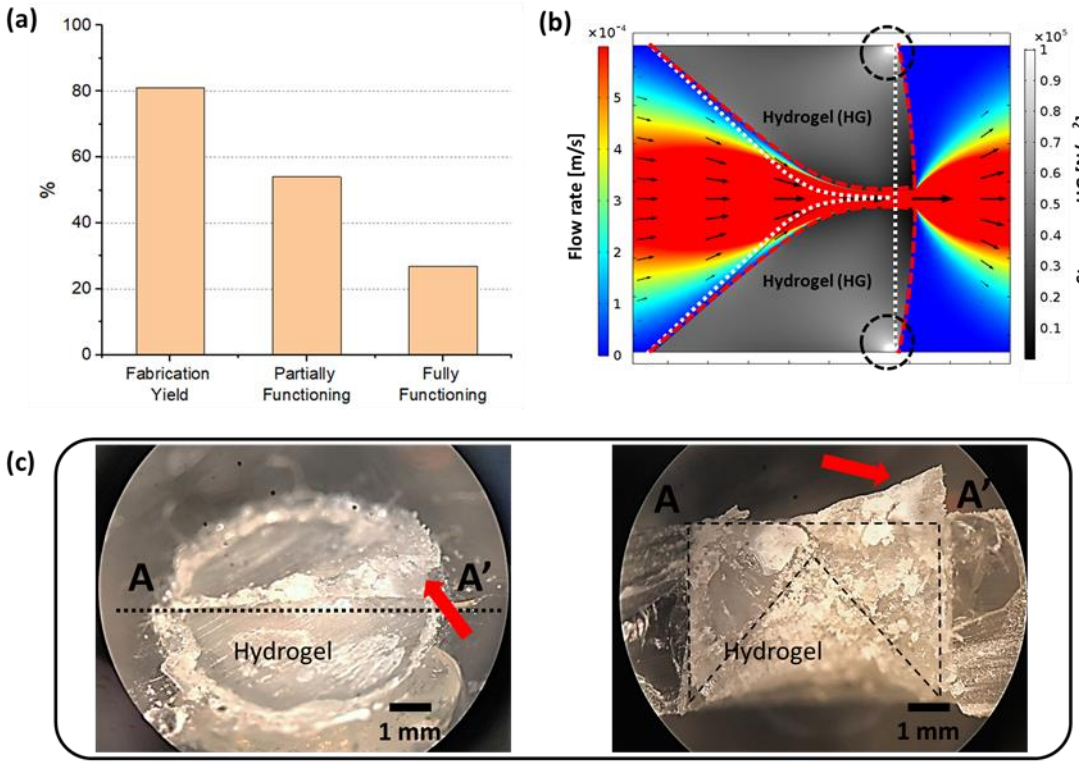

Figure 2.5. Analysis of improvement points of the hydrogel check valve. (a) Yield of manufactured devices. Out of a total of 140 fabricated devices, 113 devices (81%) had one-way valve functions where only 27 devices (19%) failed. Out of the 113 devices, 38 devices (27%) met the target hydrostatic specifications, and the rest, 75 devices (54%), marked either P_T of 10 ~ 230 mmH_2O or reverse flow leakage of < 50 µl/min. This shows significant yield improvement over our previous approaches, having less than 1% yield. (b) Finite Element Method (FEM) simulation result for stress applied to hydrogel and flow rate through the channel. The flow was applied from left end to right end at 500 mmH_2O of differential pressure. The white dotted line indicates the original location of the hydrogel before the pressure was applied and red dotted line shows deformed hydrogel at the given hydraulic condition. On the hydrogel, the highest stress is incurred at the adhesion points, indicated by black dotted circles. (c) Photographs of the failed devices. The hydrogel valve

was partially detached from the adhesion surface between the hydrogel structure and surrounding acrylic plate, which suffered the highest fluidic stress as shown in the simulation (b).

2.5. Conclusion

The hydrogel check valve utilizing hydrogel swelling phenomena and 3D printing technique for high yield fabrication was presented in this work for the treatment of hydrocephalus. The valve evaluation was performed in various ways – bench-top model, long-term loop functional test and realistic experiments – to validate the valve's ability to function as an alternative HCP treatment method. Based on measurements on the bench-top model, the valve demonstrated the target hydrostatic characteristics for CSF drainage mechanism with non-zero P_T and negligible leakage. Long-term functional tests and a realistic in vitro experiment using a sheep brain build on earlier work in our group (Schwerdt, 2013; Schwerdt, 2015) and validate the valve's potential for treating HCP.

2.6. Supporting information

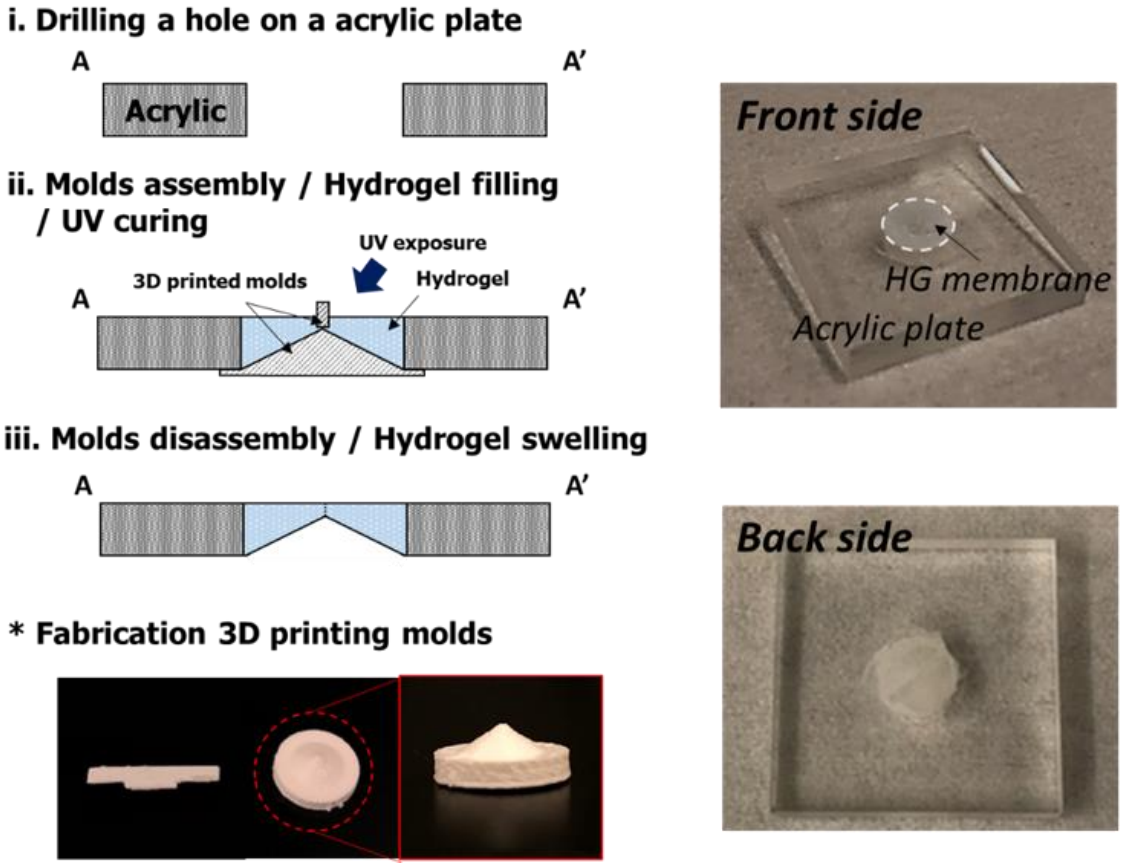

Figure 2.6. Fabrication process of the hydrogel valve. i. Drilling a hole in the center of an acrylic plate. ii. 3D printed molds is assembled in the hole, and then prepared hydrogel solution is poured and cured by UV of 400 mJ/cm2. iii. The 3D printed molds are disassembled and immerse the device in water to swell the hydrogel. iv. Photograph of actual 3D printed molds.

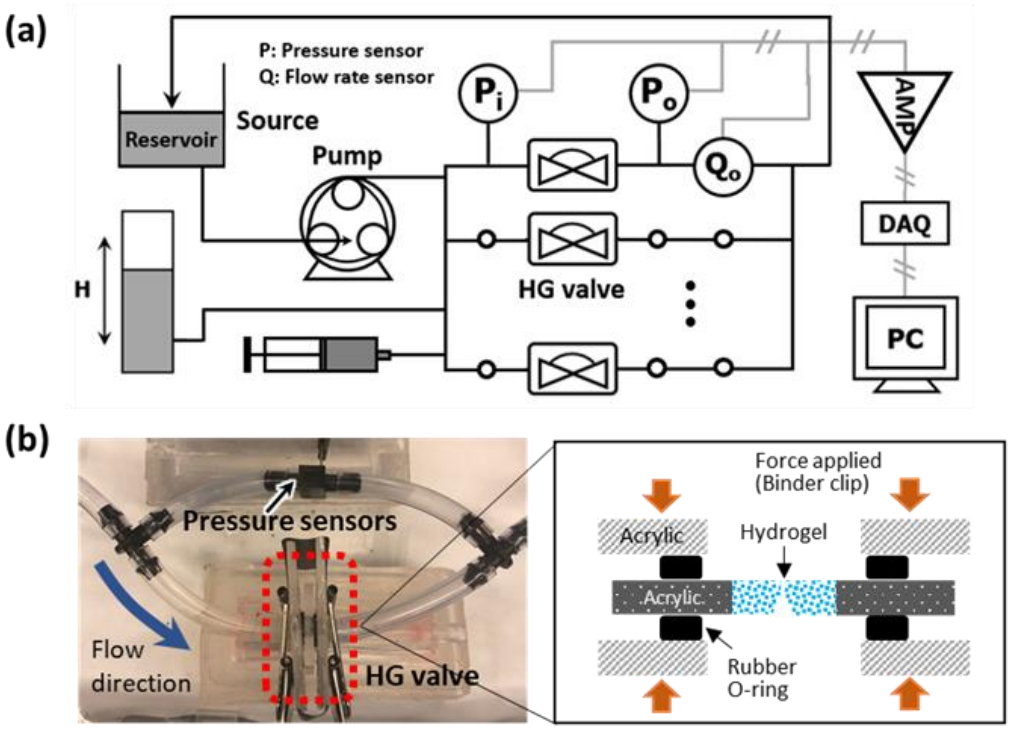

Figure 2.7. Experimental setup for the bench-top functional tests. (a) Experimental setup for evaluation of valve functionality. For the fluid sources, fluid column (a graduated cylinder), syringe pump (Model 33 syringe pump, Harvard Apparatus) and peristaltic pump (P-70, Harvard Apparatus) were used depending on the purpose of the experiments. Commercial resistive pressure sensors (PX26-001DV, Omega) are used for measurement of pressure and flow rate with customized calibrations and the electric signals, voltage, from the sensors are transmitted through voltage amplifier and data acquisition board (NI USB 6216, National Instruments) and recorded by Signal express software on a PC. (b) Photograph of the hydrogel valve setup (left) and sandwich-type connecting module (right). The module was constructed using two acrylic plates with a hole at the center and two rubber O-rings, each placed between the acrylic plates and respective side of the valve. The module sealing was performed by aligning the holes of the acrylic plates with rubber

O-rings and valve and compressing the module on both sides of the acrylic plate using binder clips.

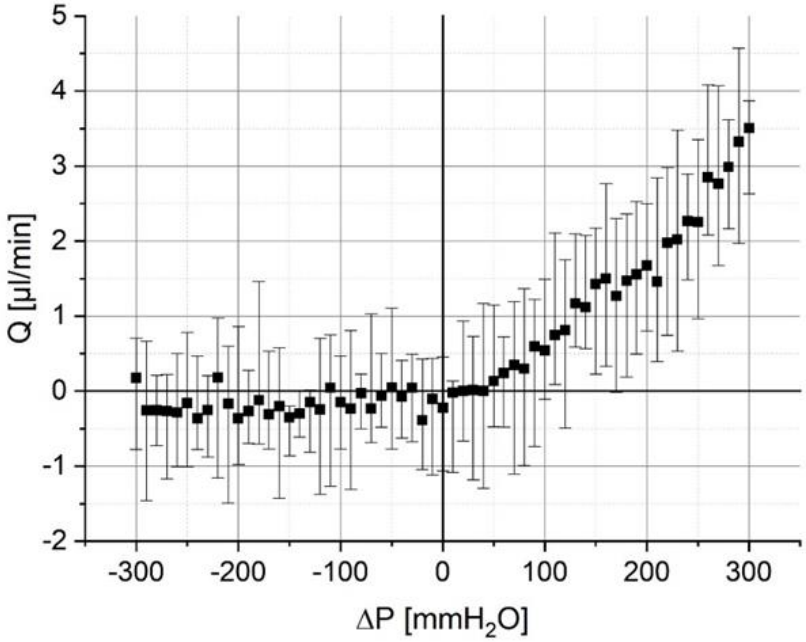

Figure 2.8. Hydraulic property of the hydrogel valve. The measurement using water column showed detail flow behavior in -300 < Δ*P* < 300 mmH2O. P_T is 42.8 ± 5.3 mmH_2O and approximately determined by calculating the slope from a fitted linear regression model based on pressure-flow rate data for $Q_O > 0$. The leakage flow was < 0.4 µl/min.

Numerical Simulations: Definitions and Geometry. COMSOL Multiphysics 5.3a software was used to illustrate the damage applied on the hydrogel structure of the valve. The software utilizes finite element method (FEM) to solve the simulated model in accordance with user-selected physics. At this model, surface plots were generated showing the flow rate of the injected liquid and stress applied on the hydrogel valve structure. The model geometry was designed using AutoCAD software (Autodesk, USA) and imported into COMSOL for modeling on the module of *Fluid-Structure Interaction*

(FSI). The model geometry consists of a horizontal flow channel and an asymmetric valve structure in the middle of it. Liquid water was assigned (COMSOL's built-in Materials Browser) as the injected liquid at inlet of the model domain. The fluid flows from left to right (inlet to outlet) and it applies a force on the valve structure's walls resulting from the fluid pressure. The valve structure is assigned as a deformable material with the physical properties of hydrogel that included young's modulus of 200 [kPa], Poisson's ratio of 0.43 and density of 1300 [kg/m^3].

Model Details. The *Fluid-Structure Interaction* module simulates a *Single-Phase Flow* interface with a *Solid Mechanics* interface to analyze the interaction between the fluid and the solid structure. Especially, the *Fluid-Structure Interaction* interface uses an Arbitrary Lagrangian-Eulerian (ALE) method to elucidate how the fluid flow can affect (or deform) the structures and how to solve for the flow in the deforming geometry. Because the fluid flow is affected by a new path resulted by the structure deformation, so solving the flow in a continuously deforming geometry is necessary using the ALE method. For this purpose, COMSOL Multiphysics utilizes generalized Navier-Stokes equations to solve for the flow interactions. The solid mechanics is usually simulated in a fixed coordinate system without the ALE method, but only strains are computed with ALE.

Governing equations and boundary conditions: Fluid flow. The fluid flow is described through the incompressible Navier-Stokes equations in the spatial moving coordinate system.

$$\rho\frac{\partial \mathbf{u}}{\partial t} - \nabla \cdot [-p\mathbf{I} + \eta(\nabla \mathbf{u} + (\nabla \mathbf{u})^T)] + \rho\big((\mathbf{u} - \mathbf{u}_m) \cdot \nabla\big)\mathbf{u} = \mathbf{F}$$

$$-\nabla \cdot \mathbf{u} = 0$$

where ρ is the fluid density, $\mathbf{u}$ is the velocity field of the flow ($\mathbf{u} = (u, v)$), p is the fluid pressure, $\mathbf{I}$ is the identity tensor, η is the dynamic viscosity of the fluid, $\mathbf{F}$ is the volume force affecting the fluid, $\mathbf{u}_m$ is the coordinate system velocity ($\mathbf{u_m} = (u_m, v_m)$) resulted by the movement of the coordinate system. In the case no gravitation or other volume forces affect the fluid, $\mathbf{F = 0}$.

Structural mechanics. An elastic formulation is utilized to solve the structure deformations with the governing equations as below,

$$\nabla\sigma + F_s = \rho_s \frac{\partial^2 \boldsymbol{d}_s}{\partial t^2}$$

For this expression, ρ_s is the solid density, σ is the Cauchy stress tensor, F_s is the body force per unit volume, and $\boldsymbol{d}_s$ is the displacement of the solid. The load experienced from the fluid can be expressed by,

$$F_T = -\mathbf{n} \cdot \big(-p\mathbf{I} + \eta(\nabla \mathbf{u} + (\nabla \mathbf{u})^T)\big)$$

where, $\mathbf{n}$ is the normal vector to the boundary. The load represents a sum of pressure and viscous forces.

Table 2-1. Summary of Major Model Conditions

Fluid material	Water	From material library	
Solid material	Hydrogel	Young's modulus	200 [kPa]
		Poisson's ratio	0.43
		Density	1300 [kg/m^3]
Temperature		293.15 [K]	
Pressure (@inlet)		5000 [Pa]	
Mesh smoothing		Winslow	
Compressibility		Incompressible flow	
2D Plots		Stress (fsi.mises)	
		Flow velocity (fsi.U)	

Table 2-2. Performance Comparison

	Arachnoid Granulation	**Traditional Shunts**	**3-D Dome Petal**	**Hydrogel Valve V1**
Cracking Pressure	40 – 60 mmH_2O	10 – 230 mmH_2O	0 mmH_2O	20 – 110 mmH_2O
Reverse Flow Leakage	0 μL/min	100 μL/min	8 μL/min	2.5 μL/min
Operating duration	-	50% failure in 2 yrs	-	-
	Hydrogel Valve V2	**Our study (Benchtop)**	**Our study (Sheep brain)**	
Cracking Pressure	1 – 110 mmH_2O	46.0 ± 7.3 mmH_2O	112.9 ± 9.8 mmH_2O	
Reverse Flow Leakage	10 μL/min	1.1 μL/min	3.7 μl/min	
Operating duration	21 days	1536 times (≈1536 days)	-	

CHAPTER 3

3. Hydrogel Check-Valves for the Treatment of Hydrocephalic Fluid Retention with Wireless Fully-Passive Sensor for the Intracranial Pressure Measurement

3.1. Abstract

Hydrocephalus (HCP) is a neurological disease resulting from a disorder of the cerebrospinal fluid (CSF) drainage mechanism in the brain, thus reliable CSF draining is necessary to treat hydrocephalus. The current standard of care is an implantable shunt system to redirect CSF. However, the shunts have a high failure rate caused by complications including mechanical malfunctions, obstructions, infection, blockage, breakage, overdrainage, and/or underdrainage. Herein, we present the evaluation of a fully realized and passive implantable valve, made of hydrogel, to restore CSF draining operations within the cranium. Valves are designed to have a non-zero cracking pressure and no reverse flow leakage with innate hydrogel swelling phenomena to strengthen reverse flow sealing. They were evaluated in a physiologically and biologically realistic fluidic environment and display reasonable operation in range of natural CSF draining with negligible reverse flow leakage. A customized wireless pressure sensor was also used for *in situ* intracranial pressure measurement in the case of valve implantation in the brain. Those evaluation validated functional reproducibility of the valve and further strengthens valve's validity for use as a chronic implant.

3.2. Introduction

Hydrocephalus (HCP) is a chronic neurological disorder characterized by the inability to adjust drainage of cerebrospinal fluid (CSF), and nearly 1 in 500 infants born in the United States suffer from hydrocephalus (NINDS, 2012). CSF is a vital supporting liquid that flows through and around the cerebral cortex representatively functioning as; 1) a "cushion" for protecting the brain and spinal cord from external shocks; 2) a "deliverer" for nutrients necessary for brain and removing waste; and 3) a "regulator" to adjust intracranial pressures (ICP) through flowing between the cranium and spine (Verrees M. a., 2004). Regarding ICP adjustment, CSF is drained through the arachnoid granulations (AG), which act as one-way biological valves, from subarachnoid space (SAS) to superior sagittal sinus (SSS). In the case of hydrocephalic patients, this draining pathway of AG is disrupted, and it causes an imbalance between the amount of produced and drainage of the CSF, leading to excess accumulation of CSF in the ventricles (Brodbelt, 2007; Chabrerie, 2002; Kirkpatrick, 1989).

The current standard treatment for HCP is the implantation of drainage tube, which is called a shunt, between the ventricles of the brain and abdominal cavity or heart for providing drainage of excessively accumulated CSF. These are implanted such that an inflow catheter directs CSF from the ventricle through the skull into a valve that controls CSF flow into an outflow catheter, which then directs CSF into distal organs (Understanding Hydrocephalus, 2019; Drake, 2000; Medtronic, 2012).

Unfortunately, these shunts have a notoriously high failure rate, where 50% of shunts fail within the first two years of implantation, even though the shunts are the most popular and primary treatment method for the hydrocephalus. Majority of the shunt

complications are normally catheter based-occlusion failures. For instance, catheters of implanted shunt are exposed to the blood and cellular debris, both contain proteins that bind to the shunt inducing macrophages and monocytes to produce growth factors. These, in turn, attract astrocytes and can potentiate an inflammatory response. Generally, occlusion-based shunt failures are caused by foreign body response, infection, and cellular growth (Drake, 2000; Drake J. K., 1998; Stone, 2013; Czosnyka, 2005; M., 1997).

Therefore, a catheter-less approach to reduce the overall implant surface area may be attractive to address these complications, and alternative shunt methods have been studied to improve current shunt systems, including MicroElectroMechanical System (MEMS)-based devices. MEMS valves have been extensively researched and developed, and many researchers have proposed fluidic valves to control CSF as an implantable valve in a various of forms such as cantilever, bridge, perforated membrane, or spherical ball type valve (Oh J. K., 2011; Oh K. a., 2006; Chen, 2007; J. Tir´en, 1989; Kim D. a., 2007; Lo R. L., 2009; Moon, 2012; Schwerdt, 2015; Schwerdt, 2013). However, critical challenges still exist: reverse flow leakage (Oh J. K., 2011), valve deformation in long-term operation (Kim D. a., 2007), valve stiction, imperfect sealing (Oh J. K., 2011; J. Tir´en, 1989; Kim D. a., 2007), etc. involving low reproducibility and durability of the valves. To overcome these challenges, our earlier work has proposed the hydrogel check valve meeting the two required features: 1) a non-zero cracking pressure (from 20 to 110 mmH_2O), and 2) negligible reverse flow leakage (Schwerdt, 2015; Schwerdt, 2013; Lee, 2020). However, the previous work suffered from deficiency in the accurate measure of

fluid pressure across the valve as measured inside of the setup, and lack of verification of the valve in realistic environments.

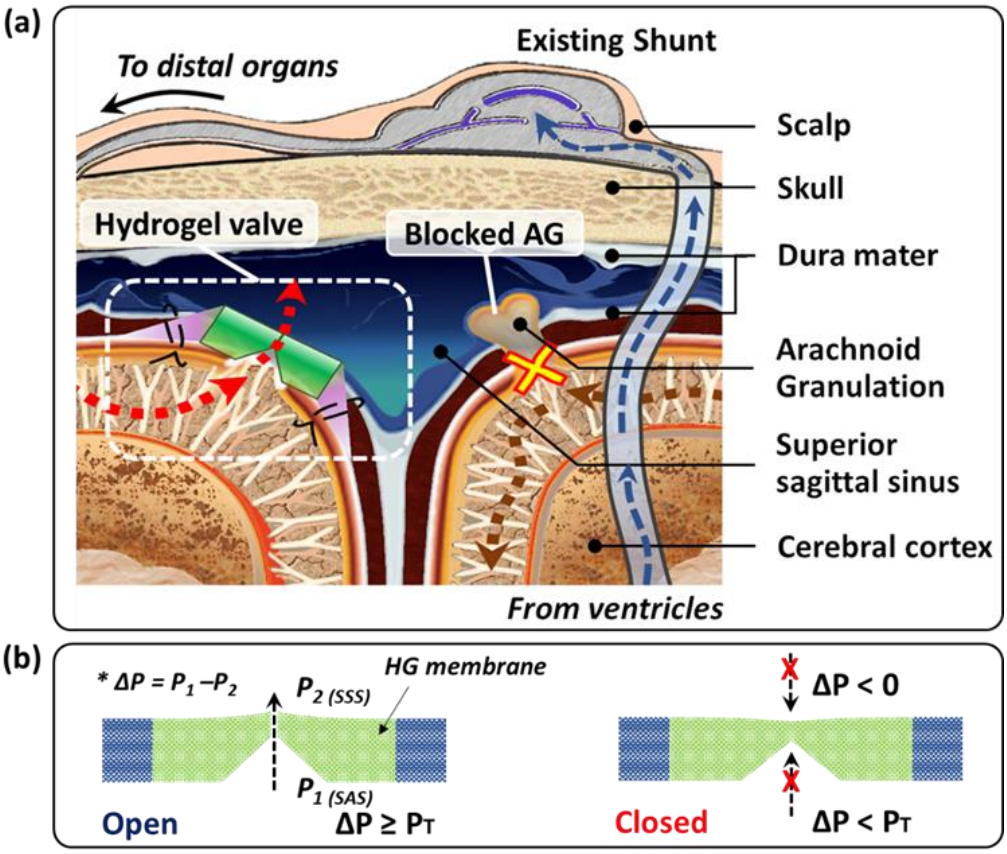

Figure 3.1. Illustration of the alternative cerebrospinal fluid draining methods and working mechanism. (a) Illustration of alternative cerebrospinal fluid (CSF) draining methods (existing shunt system and hydrogel valve of this work) for hydrocephalus treatment. Existing shunts include catheters connected from the ventricles to distal organs and transcranial to drain CSF outwards. The proposed hydrogel valve is implanted directly in the intradural surface of the superior sagittal sinus and directs CSF drainage from subarachnoid space (SAS) into the superior sagittal sinus (SSS). This method of directing CSF allows the CSF draining process to be confined within the cranium without the use of

catheters that cause many complications. (b) Basic operation of the valve at a cross-sectional view. When the hydrogel becomes hydrated, the swollen hydrogel structure closes the hole, forming the closed valve. When the pressure in the SAS reaches higher than the SSS over the threshold, namely, cracking pressure (P_T), $\Delta P > P_T$, the swollen hydrogel valve becomes the open status, and CSF can flow unidirectionally from SAS to SSS. When the pressure at the SAS is lower than that at the SSS by less than a differential threshold, P_T, $\Delta P < P_T$, the valve is closed and blocks the CSF flow as the pressure difference cannot open the valve.

Herein, we report a physiologically and biologically realistic evaluation of the hydrogel check-valve as a hydrocephalus therapeutic and propose wireless measurement of fluid pressure across the valve to reduce open-skull surgery for CSF pressure measurement. We tested the hydrogel check-valve in increasingly realistic fluidic conditions while maintaining ~ 37 °C during evaluation. These evaluations showed that the hydrogel check-valve maintains the functionality in each condition, within the specifications of traditional shunt systems. The long-term behavior of the valve was also evaluated through the automated loop functional tests, and it demonstrates more advanced repeatability and durability of the valve than our earlier work.

Additionally, we developed a fully-passive wireless pressure sensor to measure pressure applied to the valve. Clinically, the most practical way to diagnose HCP patients is to observe the CSF pressure of the brain- intracranial pressure (ICP). If their HCP treatment device is malfunctioning, the ICP range will again be abnormal, leading to HCP again. In the worst case, the HCP patients will have a craniotomy, “brain-opening”

surgery to check their HCP implant device when they suffer from abnormal symptoms - normal headache, sleepiness, vomiting, etc. – which could be unrelated to HCP. In order to avoid this worst case, wireless pressure measurement has distinct potential as a non-invasive and non-surgical method. The fully-passive wireless pressure sensor was designed using a resistive pressure sensor and RF backscattering to transmit the ICP measurement to a receiver outside of the brain. It shows compatible output data with the wired pressure measurements.

3.3. Material and Methods

Valve design and fabrication. The valve was designed by considering the actual SSS of the human skull for ideal future implantation; the valve needs to be comparable or smaller than the SSS. The SSS has a random topology, but roughly has a mean diameter of 7.3−8.8 mm (Boddu, 2018); thus, the valve dimension was designed with a 7 mm diameter. The target specification of the valve was designed by referencing traditional shunt systems which are evaluated by industry standards, ISO 7197 and ASTM F647, in terms of cracking pressure, fluidic resistance and maximum reverse flow leakage (Viker, American Society of Mechanical Engineers,; Chung, 2003). Also, we considered actual condition of HCP patients; the normal ICP in humans ranges at −100−350 mmH_2O, and it increases to >500 mmH_2O for hydrocephalus patients. Overall, the valve aims to operate at the range of $-200 < \Delta P < 600$ mmH_2O (Chabrerie, 2002; M., 1997; Czosnyka, 2005). The target cracking pressure, P_T, is 10−230 mmH_2O, and the maximum allowable leakage is set to be 50 μL/min (Chabrerie, 2002; Drake J. K., 1998). The valve is composed of a hydrogel and surrounding substrate to support the valve structure. 3D-

printed molds are assembled in the punctured hole at the center of the surrounding plate then the liquid-state hydrogel is cured inside the hole by UV light to be solidified. (Fig. 3.2)

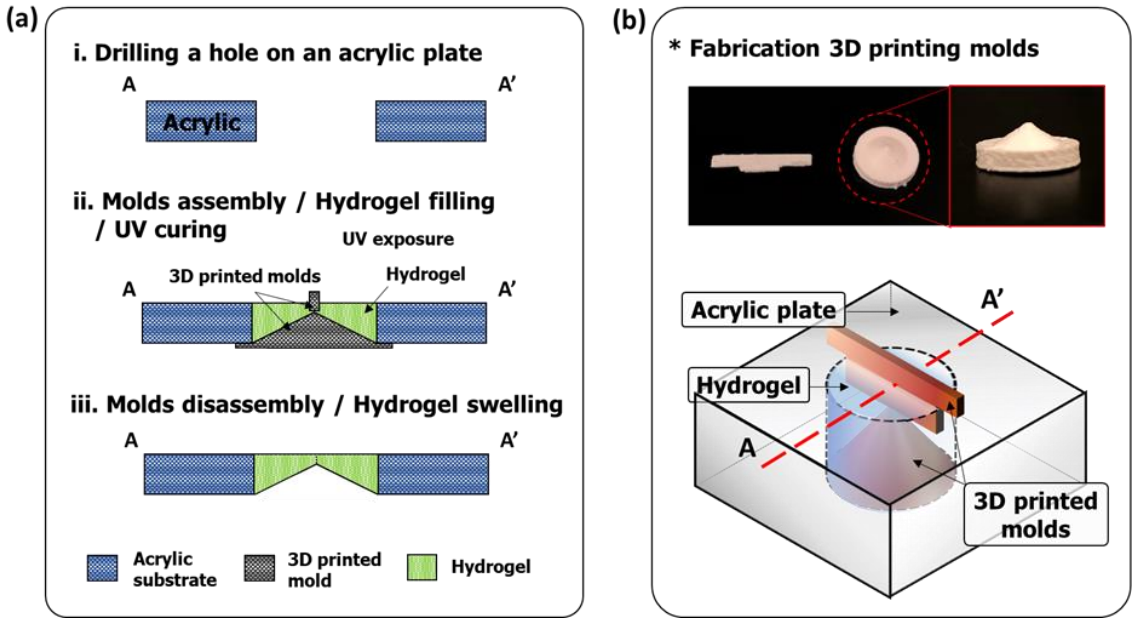

Figure 3.2. Fabrication process of the device. (a) Fabrication process - i. Drilling a hole in the center of an acrylic plate. ii. 3D printed molds is assembled in the hole, then the prepared hydrogel solution is poured and cured by UV dose of 400 mJ/cm2. iii. The 3D printed molds are disassembled and immerse the device in water to swell the hydrogel. (b) The actual 3D printed molds and illustration of the parts assembled for the device fabrication.

Hydrogel. Hydrogels are hydrophilic and absorbent polymeric networks, which can contain over 90% water. Therefore, the flexibility of a hydrogel is very similar to natural tissue, and it makes hydrogels can be very commonly used for medical devices

due to the high bio-compatibility. In this study, the preparation of the hydrogel solution was performed by mixing the base (2-hydroxyethyl methacrylate, Sigma Aldrich), crosslinker (ethylene glycol dimethacrylate, Sigma Aldrich) and photoinitiator (2,2-dimethoxy-2-phenylacetophenone, Sigma Aldrich) at a ratio of 1 : 0.04 : 0.1 respectively (Schwerdt, 2015; Schwerdt, 2013; Lee, 2020). This solution was poured onto the prepared substrate and cured by UV crosslinked at ~ 400 mJ/cm^2 for hardening it before the hydration step.

3D-printed mold. The tapered hydrogel structure was fabricated using 3D printed molds (Fig. 3.2(b)). 3D printing implements a technology known as additive manufacturing involving iteratively depositing horizontal cross sections of the desired 3D object (Rengier, 2010). This technology allows for rapid development of custom 3D models through reducing fabrication cost and time required to prototype custom models (Bose, 2013; Morgan, 2016). To create the models, 3D printers deposit layers of molten thermoplastic, a process called Fused Filament Fabrication (FFF) (Rengier, 2010). The design of these 3D models requires 3D modelling software. The models used in this research were designed in Autodesk's Fusion 360 isometric modelling software and were printed on the Ultimaker 2 Go 3D printer. The Ultimaker 2 Go has a positioning precision of 12.5 µm in the horizonal directions and a precision of 5 µm in the vertical direction.

Cerebrospinal Fluid Preparation. CSF was collected from hydrocephalic patients at the Phoenix Children's Hospital with an approved materials transfer agreement (MTA). The CSF solutions were from an aggregate of multiple CSF samples and

maintained in a 4°C environment when not in use. Five CSF sample solutions were generated from an aggregate of patient CSF, four of which were spiked with various additives known to generate occlusions in traditional shunts: calcium (1.1 mM), fibronectin (7.5 μg/mL), blood (5%), and all three combined (Del Bigio, 2015; Beems, 2003; Brydon, 1996).

Wireless pressure sensor. We aim to develop the hydrogel valve to implant in patients to treat HCP. To this end, we need to observe the status of the device when the HCP patients show any related symptoms of device failure in more patient-friendly way. Because, the HCP patients who shows any abnormal symptoms - normal headache, sleepiness, vomiting, etc. - cannot determine if the symptoms are really caused by the device malfunctions or just general causes of the physical illnesses, which are not device-related. In the worst case, the HCP patients will be supposed to have brain-opening surgery, craniotomies, just to check the device function even if the symptom was not caused by the implant. The most straightforward way to check the valve functionality is to observe the CSF pressure in the brain – the intracranial pressure (ICP), because ICP is the most related factor to show HCP symptoms. If the HCP treatment device is not working properly, the ICP range will change abnormally, and it leads to unmanaged HCP again. Through ICP measurement, we can confirm that the symptoms must be due to issues with the device. Therefore, we developed a fully-passive wireless pressure sensor to measure ICP non-invasively and non-surgically. The sensor was designed using a resistive pressure sensor and RF backscattering to transmit the ICP measurement.

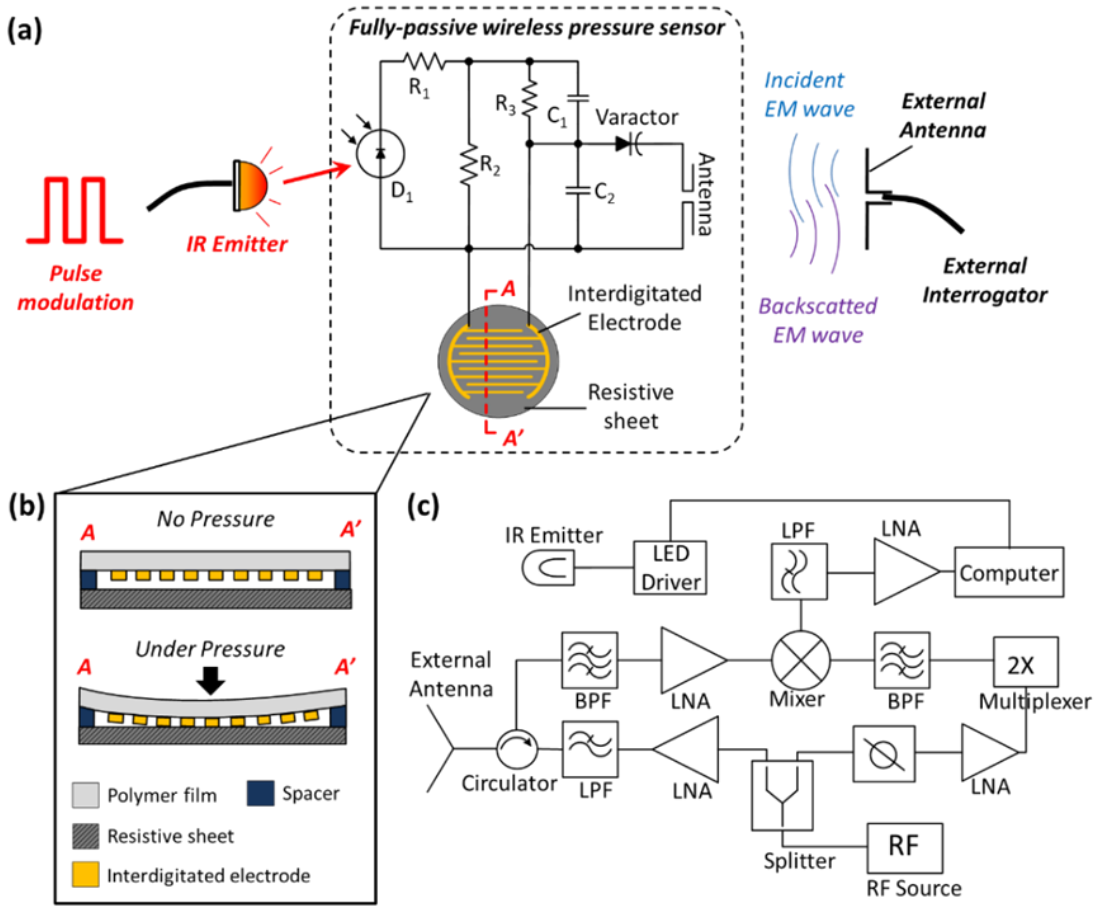

Figure 3.3. Wireless intracranial pressure (ICP) monitoring through a fully-passive method. (a) Overall of system operating principle. Wireless fully-passive pressure sensing is accomplished using both infrared (IR) and radiofrequency (RF) electromagnetic energy. The photodiode (D1) on the sensor receives the modulated IR light from the external LED IR emitter and generate an electrical voltage signal which has the same waveform as the external modulation pulse. The generated pulse is voltage divided by the resistors R_1-R_3 and the pressure sensitive resistor (b), and outputs to the varactor diode. The voltage across the varactor diode is mixed with incident RF energy, and wirelessly transmitted to the external interrogator using RF backscattering method. The external interrogator then extracts the pressure information through a series of demodulation and calculation

processes. (b) Operation principle of the pressure sensitive resistor. The resistor comprises a pair of interdigitated electrodes which is printed on a flexible polymer film. The polymer film is placed on top of a resistive sheet with a spacer sandwiched between. Under external pressure, the polymer film deforms and results in contact between interdigitated electrodes and resistive sheet, lowering the resistance of resistor. (c) Detailed structure of the external interrogator for extracting the pressure value.

Pressure value calculation. Wireless intracranial pressure (ICP) monitoring through a fully-passive method is shown in Fig. 3.3. External pressure affects the resistance of the pressure sensitive resistor. Increasing the pressure decreases the resistance. To read out the resistance change, R_3, C_1 and the resistive sensor form a voltage divider circuit, which divides the output voltage of photodiode based on the impedance ratio between $R_3 \| C_1$ and resistance of pressure sensitive resistor. For simplicity, suppose the photodiode generates a sine wave to the voltage divider circuits. The sine wave has a frequency of f_1 and amplitude of A_{i1}. The resistance of the pressure sensor is R_x. Then the amplitude of output signal, A_{o1} can be written as:

$$A_{o1} = \frac{R_x}{Z_{t1}} * A_{i1}$$

where Z_{t1} represents the impedance of $R_3 \| C_1$ (the impedance of R_3 in parallel with C_1). For simplicity suppose R_3 is 100 kΩ and C_1 is 1 nF, then Z_{t1} can be expressed as:

$$Z_{t1} = \sqrt{10^{10}\left[Im\left(\frac{1}{1 + i\frac{\pi f_1}{5000}}\right)\right]^2 + \left[R_x + 10^5 Re\left(\frac{1}{1 + i\frac{\pi f_1}{5000}}\right)\right]^2}$$

Where *Re(f)* and *Im(f)* denote the real and imaginary part of *f*. The amplitude of voltage divider output signal A_{o1} is a function of pressure sensitive resistor (R_x), photodiode output voltage A_{i1} and the modulation frequency f_1. The diode output voltage A_{i1} is greatly affected by external environment, making the output A_{o1} unstable. To overcome such effect, a second modulation frequency f_2, is introduced. Under f_2, the output signal amplitude can be written as:

$$A_{o2} = \frac{R_x}{Z_{t2}} * A_{i2}$$

where Z_{t2} is the impedance of $R_3 \| C_1$ at f_2, which can be expressed as:

$$Z_{t2} = \sqrt{10^{10}\left[Im(\frac{1}{1 + i\frac{\pi f_2}{5000}})\right]^2 + \left[R_x + 10^5 Re(\frac{1}{1 + i\frac{\pi f_2}{5000}})\right]^2}$$

The ratio between A_{o1} and A_{o2} is:

$$\text{Ratio} = \frac{A_{o1}}{A_{o2}} = \frac{A_{i1}Z_{t2}}{A_{i2}Z_{t1}}$$

Since the voltage output of diode detector is not affected by the frequency, $A_{i1} = A_{i2}$. Therefore, ratio is:

$$\text{Ratio} = \frac{Z_{t2}}{Z_{t1}}$$

Above equation shows that ratio is only a function of R_x (resistance of the pressure sensitive resistor), whose value is only related to the external pressure. Therefore, the pressure value can be obtained by calculating the ratio between A_{o1} and A_{o2}.

The two frequencies (f_1 and f_2) are chosen to be 500 Hz and 2000 Hz, respectively. It should be noted that the actual signal outputted by the photodiode is pulse wave instead of sinewave, therefore additional digital filtered need to be applied during

the post processing steps. During the testing, the DAQ outputs two frequencies (f_1 and f_2) square wave alternatively to modulate the radiation of IR light. In the meantime, ratio of two signal amplitudes is wirelessly measured to calculate real time pressure value.

The External Interrogator. Fig. 3.3(c) shows the structure of the external interrogator. The RF source (RF function generator E4432B, Agilent) produces 2.33GHz RF carrier (f_0) signal which is equally divided into two paths through a power splitter (H.N., 2011). The first path doubles the frequency to be 4.66 GHz ($2f_0$) via a frequency multiplexer for local oscillator (*LO*) of down-converter. The second path amplifies, filters the RF carrier radiates the signal through a dual-band (2.4 GHz/5 GHz) ceramic chip antenna (A10194, Antenova). Concurrently, the antenna picks up 4.66 GHz ($2f_0 \pm f_m$) backscattered third-order mixing products which carry target pressure information. The circulator isolates the backscattered signal from the RF carrier. After amplifying and filtering, the third other mixing products ($2f_0 \pm f_m$) mixes with the *LO* ($2f_0$) to down-convert the output to be f_m. Demodulated signal (f_m) go through filtering and amplifying (SR560, Stanford Research System) and is sampled at 40000 bit/sec using a Data Acquisition Card (DAQ, NI-6361, National Instrument). The LabView (National Instrument) program is developed to post process the signal and calculate pressure value.

3.4. Results

Bench-top setup. The hydrogel check-valve was evaluated for basic functionality in the bench-top fluidic circulatory setup. The functional tests were performed to ensure that the valve would open under forward flow and that the reverse flow leakage was

properly sealed by the hydrogel swelling phenomena. The setup consists of the hydrogel valve, fluid source and pressure & flow rate sensors (Fig. 3.4). For the fluid circulatory system, we used a few types of source – syringe pump (Model 33 syringe pump, Harvard Apparatus) and peristaltic pump (P-70, Harvard Apparatus) for short-term and long-term functionality tests respectively. Resistive pressure sensors (PX26-001DV, Omega), which have 1 mmH_2O resolution, were used for measurement of differential pressure & flow rate and calibrated for the actual experiments by a customized setting. All data were recorded by a data acquisition board (NI USB 6216, National Instruments) and SignalExpress software (Schwerdt, 2015; Schwerdt, 2013; Lee, 2020).

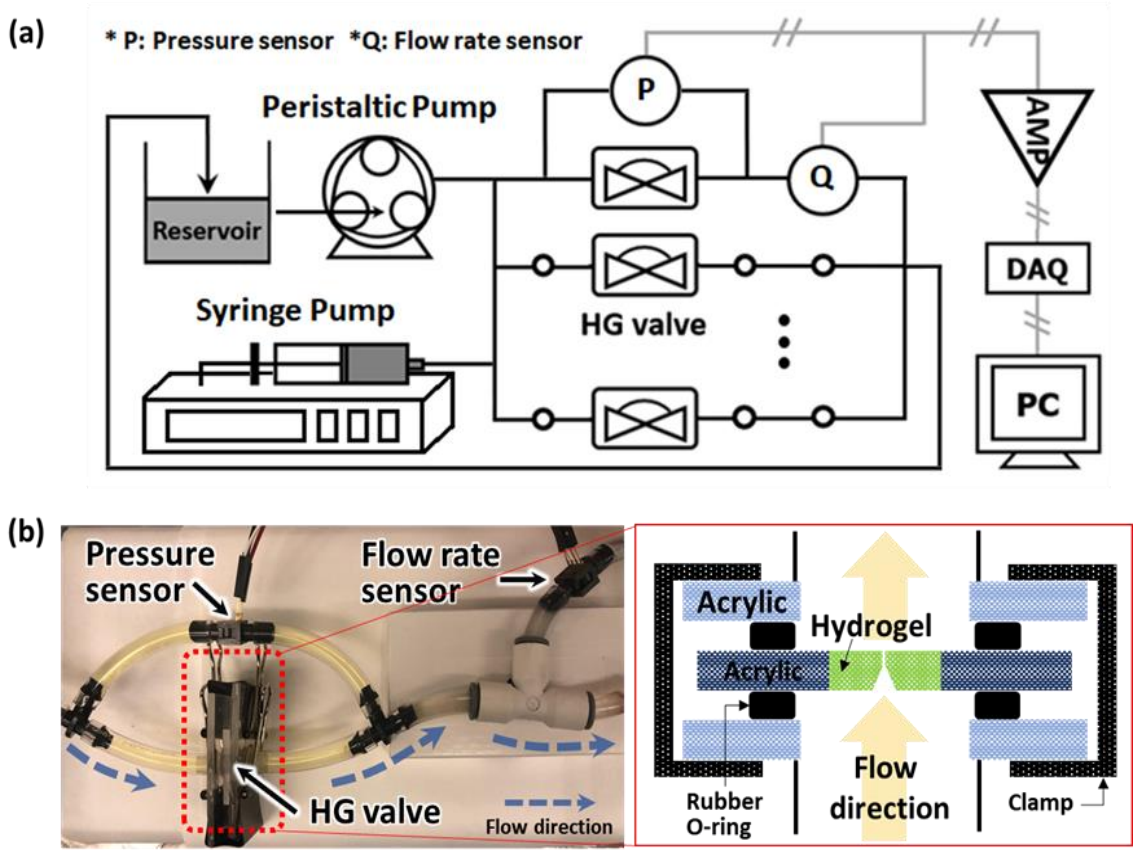

Figure 3.4. Experimental setup for the bench-top functional tests. (a) Experimental setup for evaluation of valve functionality. For the fluid sources, syringe pump (Model 33 syringe pump, Harvard Apparatus) and peristaltic pump (P-70, Harvard Apparatus) were used depending on the purpose of the experiments. Commercial resistive pressure sensors (PX26-001DV, Omega) are used for measurement of pressure and flow rate with customized calibrations and the electric signals, voltage, from the sensors are transmitted through voltage amplifier and data acquisition board (NI USB 6216, National Instruments) and recorded by SignalExpress software on a PC. (b) Photograph of the hydrogel valve setup (left) and sandwich-type connecting module (right). The module was constructed using two acrylic plates with a hole at the center and two rubber O-rings, each placed between the acrylic plates and respective side of the valve. The module sealing was

performed by aligning the holes of the acrylic plates with rubber O-rings and valve and compressing the module on both sides of the acrylic plate using binder clips.

Long-term valve testing was performed to check valve's reliability and durability by automated loop testing setup using the programmable peristaltic pump to control fluidic flow with the number of flow cycles, flow rate and flow direction. The valve was evaluated in a qualitative way to measure the number of valve's operating instead of a quantitative way in a real-time duration due to the limit of lab-base environment.

In Vitro animal model setup. The *in vitro* evaluation setting for the valve was built on a fixed sheep brain (Bio corporation, Alexandria, MN). The sheep brain was preserved with the dura mater and enclosed by PDMS molding to prevent fluid leakage. The hydrogel valve and customized wireless pressure sensor were placed on the locations we punched through the dura mater manually. CSF was injected into the cavity created by the valve and SAS, and the differential pressure across the valve was measured by the resistive pressure sensor.

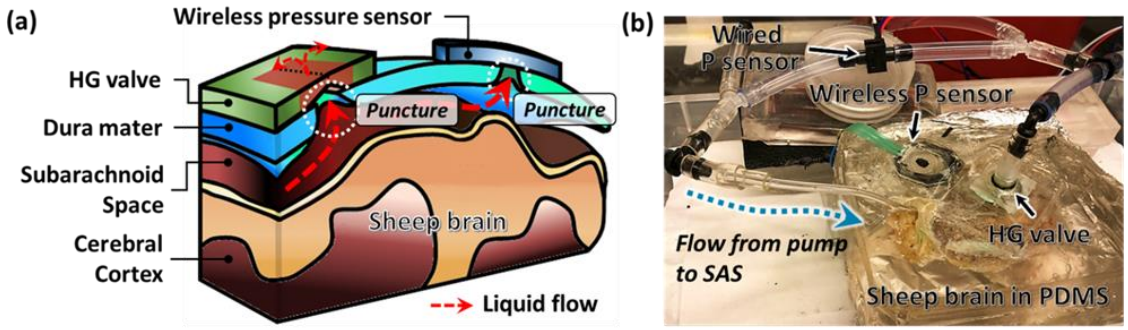

Figure 3.5. Experimental setup for the functional test on the sheep brain model. The hydrogel valve was evaluated in an *in vitro* setting using a fixed sheep brain. (a) Schematic of the experiment setup. The valve and customized wireless pressure sensor were set in the designated location on the dura mater where we manually punctured through. (b) Actual configuration of the experimental setup. A syringe pump injects CSF into the cavity formed by SAS and the valve. The excess portion of the manual cut was sealed by PDMS to prevent any leakage. The differential pressure is measured across the valve using wired and wireless sensors simultaneously.

Hydrodynamic Valve Characteristics. Basic hydrodynamic response of the hydrogel valve was measured and display valve operation within the target range in terms of normal CSF drainage in bench-top testing (Fig. 3.6 (a)) and in an *invitro* fixed sheep brain (Fig. 3.6 (b)). To evaluate the valve in further realistic patient conditions, the valve was tested in the emulated biological fluids; all based on CSF with various additives known to generate occlusion-based failures in traditional shunts: Water, CSF, CSF + Calcium (1.1 mM), CSF + Blood (5 % v/v), CSF + Fibronectin (7.5 µg/mL) and CSF + All additives at ~ 37°C (Del Bigio, 2015; Beems, 2003; Brydon, 1996). The hydrogel valve remained functional showing high diodicity without a noticeable reverse flow

leakage, while being tested under the six fluid conditions. The measured average P_T and leakage flow were 56.6 ± 5.4 mmH_2O and 1.55 μL/min in the bench-top experiments, and 115.3 ± 6.2 mmH_2O and 2.0 μL/min in the sheep brain experiments. The measured P_T from the sheep brain experiments is higher than that of bench-top evaluation because a sheep brain tends to be easily deformed and the valve was even placed on the thin flexible dura mater, possibly leading to the attenuation of pressure on the valve (Lee, 2020). The detail measurements of valve's flow response are shown in Table 1.

Table 3-1. Summary of Specifications for Hydrogel Valves Tested in Worst-case Environment

Fluid type	Bench-Top		Sheep Brain	
	P_T [mmH_2O]	Q_R [μl/min]	P_T [mmH_2O]	Q_R [μl/min]
CSF	46.0 ± 7.3	1.1	113.0 ± 9.8	2.7
Water	51.5 ± 5.5	1.3	81.2 ± 4.7	1.6
CSF + Calcium	38.5 ± 5.4	1.7	135.1 ± 5.1	2.3
CSF + Fibronectin	68.3 ± 4.7	1.7	117.5 ± 5.9	1.9
CSF + Blood	62.9 ± 3.2	2.1	152.7 ± 4.9	1.7
CSF + All	72.4 ± 6.1	1.4	92.2 ± 7.0	2.0

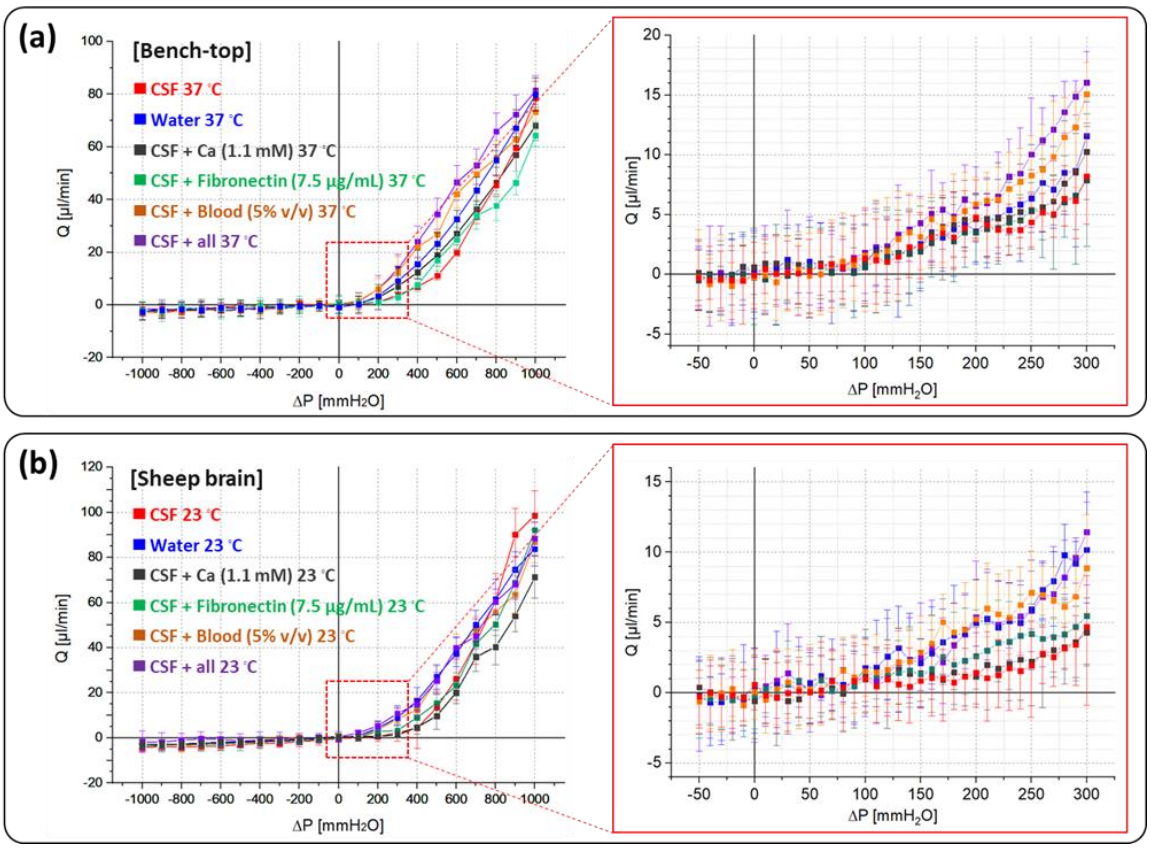

Figure 3.6. Hydraulic properties of the hydrogel valves in the worst-case fluidic conditions. A series of increasingly worst-case fluidic conditions were used to emulate various failure modes seen in traditional shunt systems, namely occlusion due to foreign body response / fibrous encapsulation, and mineralization due to calcification. The functional tests were performed on (a) bench-top and (b) *invitro* fixed sheep brain setup. The hydrogel check-valve remained functional, with reasonable cracking pressure range and negligible reverse flow leakage. The detail results of the valve's functionalities are described in Table 3-1.

Fully-passive wireless pressure sensor. Wireless monitoring of intracranial pressure (ICP) is accomplished in a completely passive manner. The overall operating principle of wireless fully-passive pressure sensor is demonstrated in Fig. 3.3(a). Herein,

two different kinds of energy, namely infrared light (IR) and radiofrequency (RF) electromagnetic wave, are adopted to enable wireless acquisition of pressure. An external LED IR emitter radiates a beam of IR light whose intensity is modulated by an external pulse signal to enable chopping. The photodiode D_1 on the sensor senses the variation of IR energy and converts it to electrical voltage signal which has the same waveform as the external pulse. The generated voltage signal is divided by a voltage divider circuit consisting of resistors R_1-R_3, capacitor C1 and the pressure sensitive resistor. Fig. 3.3(b) shows the structure of the pressure sensitive resistor. A pair of interdigitated electrodes is printed on a flexible polymer film. The film is placed upside down on top of a resistive sheet, with a spacer sandwiched in the middle. Under external pressure, the flexible polymer will deform, causing the interdigitated electrodes contacting with the resistive sheet, thereby reducing overall resistance between the two interdigitated electrodes. This forms a pressure sensing resistor whose resistance decreases as external pressure increase. As a proof of concept prototype, the pressure sensitive resistor is assembled using a commercially available force sensitive resistor (FSR). The polymer film with interdigitated electrodes is removed from the commercial FSR and is adhered onto the resistive sheet (Velostat) using double sided tape, which also function as spacer. Assembled pressure sensitive resistor is sealed with sealing tape. Two electrical leads connect the pressure sensitive resistor to the fully-passive wireless sensor.

The voltage divider circuit measures the resistance of the pressure sensitive resistor and output electrical signal to the varactor diode. Thus, external pressure value can be obtained by measuring the amplitude of voltage signal, V_m, across the varactor diode, which is accomplished utilizing RF backscattering (H.N., 2011). In short, the

external interrogator generates and radiates an RF electromagnetic wave (f_0). The sensor receives the incident EM wave through its integrated antenna. The varactor diode then mixes the RF signal (f_0) with the target signal (f_m) and produces the third-order mixing products ($2f_0 \pm f_m$), which is scattered back and picked up by the external interrogator. The external interrogator extracts the target signal (f_m) through a series filtering and demodulating procedures. Extracted signal is then processed by computer to calculate pressure value. The fully-passive wireless sensor is fabricated using copper clad polyimide pad, and discrete surface mount electronic components, including photodiode, varactor diode, resistors and capacitors, are soldered onto the exposed pad.

Wireless pressure measurements. The pressure measurements were also performed by using a wireless pressure sensor. The wireless pressure sensor required unit calibration first with arbitrary units, since the pressure to resistance relationship is highly fabrication dependent. The wired pressure sensor was used for the calibration as a reference measurement while the wireless pressure sensor measured the pressure variance. The relationship between the wireless and wired sensor showed linear behavior in positive pressure range and revealed a slope of 0.0012 a.u./mmH_2O with a coefficient of determination value of $R^2 = 0.9687$, obtained from a fitted linear regression model. In the negative pressure range, the wireless pressure sensor couldn't measure the pressure variance due to its geometrical limit of resistance. The sensor can measure pressure only in one direction currently, bi-directional wireless pressure measurement will serve as the subject of future studies.

The calibrated wireless pressure sensor was used for valve functional tests in sheep brain experiments and the results shown in Fig. 3.7 display reasonable hydrodynamic behavior of the valve within the target specification. The valve has P_T of 108.1 ± 3.4 mmH_2O, which value is clearly comparable to the result of wired measurement, P_T of 113.0 ± 9.8 mmH_2O.

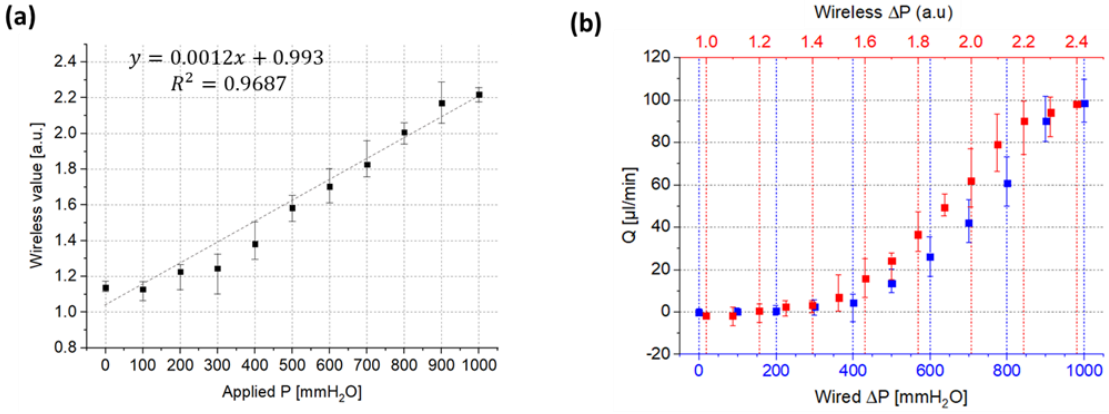

Figure 3.7. Calibration of the wireless pressure sensor. The calibrated wireless pressure sensor was used for valve functional tests in positive pressure range and served to provide reasonable hydrodynamic behavior of the valve. (a) Calibration of the wireless sensor in terms of the applied pressure. (b) Flow response of the valve in the wired / wireless measurement. The valve demonstrated reasonable flow response in both modes with high flow diodicity and no flow leakage. By the wired measurement, the valve shows flow rates of 0 ~ 98.5 μl/min, P_T of 113.0 ± 9.8 mmH_2O and negligible reverse flow leakage of 3.7 μl/min. The wireless measurement also displays that the valve has comparable flow response to the wired measurement with P_T of 108.1 ± 3.4 mmH_2O.

Long-Term Functional Tests. We performed repetitive functional tests to evaluate valve's long-term feasibility in terms of the run cycles. The test was controlled by a programmable peristatic pump for repetitive sequences of forward/reverse cycles in the range of $-50 < \Delta P < 300$ mmH_2O (Klarica, 2014). In order to advance reliability and durability of the valve, glass was used for the supporting material instead of the acrylic. Because the hydrophilicity of glass is higher than acrylic, it provides more robust adhesion strength with hydrogel than acrylic-hydrogel. 5 devices were used for the evaluation and maintained comparable cracking pressure and negligible reverse flow leakage for > 2000 running times within the range of $52.3 < P_T < 67.1$ mmH_2O and < 0.5 μL/min, respectively (Figure. 3.8 (a), (b)). Comparing to the results of previous devices using acrylic, glass-based hydrogel valves display much enhanced long-term functionality, increased by ~ 70 % as a function of run cycles. Throughout the repetitive testing, device under test #4 (DUT 4[G]) out of the 5 devices remained within design specifications over the course of 2256 cycles of running with relatively constant cracking pressure and little reverse flow leakage of $48.3 < P_T < 75.1$ mmH_2O and < 0.4 μL/min, respectively (Figure. 3.8 (c)).

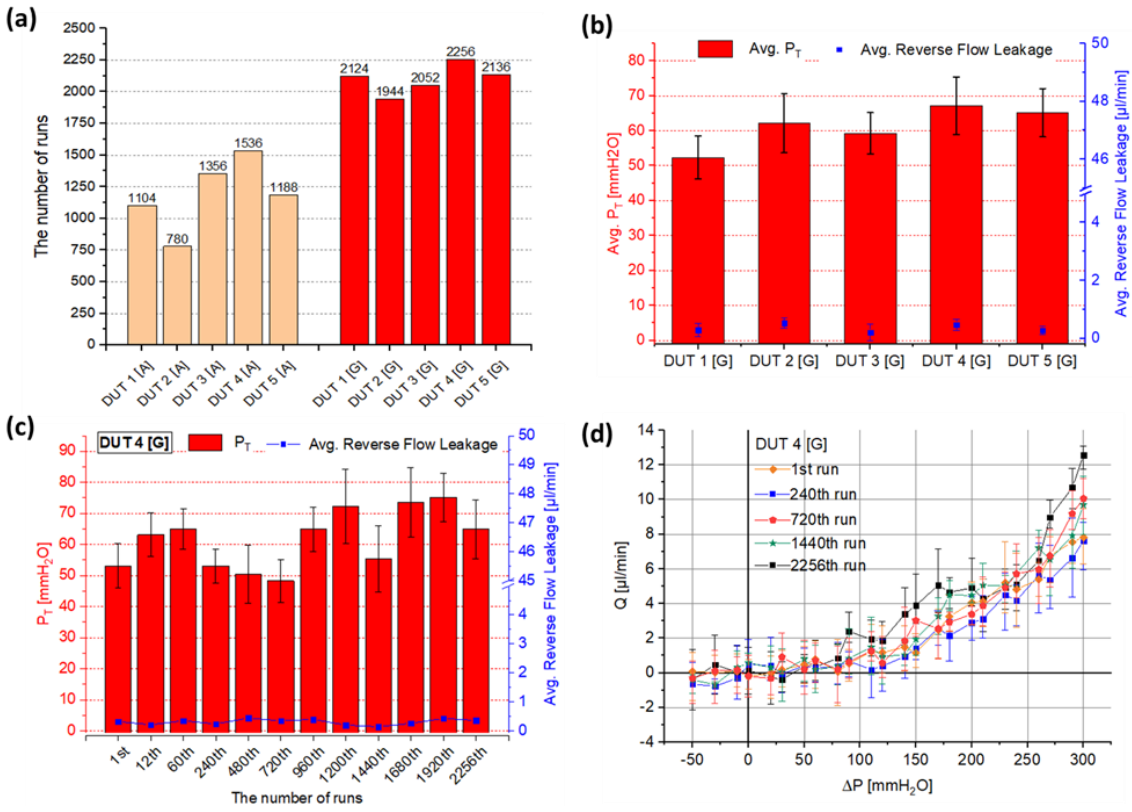

Figure 3.8. Results of the automated repetitive tests for the evaluation of the valve's long-term functionality. Automated repetitive tests were performed by a programmable peristaltic pump to evaluate the valve's long-term functionality. In order to enhance the reliability and durability of the valve, glass was used for the surrounding substrate instead of acrylic plate because glass has higher adhesion strength than acrylic due to its superior hydrophilicity. One cycle consists of flow response measurements in forward and reverse flow and is analogous to a one-day operation of the valve (Del Bigio, 2015). (a) Results of the automated repetitive tests of 5 devices of acrylic based (DUT [A]) and glass based (DUT [G]), respectively. The 4 out of the 5 devices with glass surrounding substrate (DUT 1[G], 3[G], 4[G], and 5[G]) marked much higher cycles of runs, >2000. Generally, the glass-based devices display ~ 70% higher running times than acrylic based devices. (b)

Average value of P_T and reverse flow leakage of the devices during the repetitive tests. The devices show P_T and reverse flow leakage in the range of 52.3 ~ 67.1 mmH_2O and < 0.5 μL/min, respectively. Error bar: standard deviation. (c) P_T and reverse flow leakage of DUT 4[G] over 2256 cycles. The measurements show the valve functions consistently at $48.3 < P_T < 75.1$ mmH_2O and reverse flow leakage of < 0.3 μL/min. Error bar: standard deviation. (d) The flow response of the valve (DUT 4[G]) shows high diodicity behavior with negligible reverse flow leakage throughout 2256 runs. Error bar: min to max.

3.5. Conclusion

The hydrogel check valve presented here provides near identical flow characteristics with an above zero cracking pressure and little to no reverse flow leakage as an alternative HCP treatment method. Ultimately, we have developed an implantable valve which is capable of accurately replicating the function of arachnoid granulations in a variety of *in vitro* models of hydrocephalus increasing in both biologically and physiologically realistic conditions. The wireless pressure measurement was also performed using customized fully-passive pressure sensor. By comparison with the wired measurement, the results validate the valve's potential with non-invasive and non-surgical ICP measurement.

Chapter 4

4. HYDRAULIC CHECK-VALVE FOR HYDROCEPHALUS TREATMENT FABRICATED IN GLASS NEEDLE AND IMPLANTATION WITH PDMS GROMMET

4.1. Introduction

Hydrocephalus is a chronic disorder characterized by an excessive accumulation of CSF within the cavities (ventricles) of the brain directly leading to dangerous increases in intracranial pressure (ICP)[8,9]. The exact cause of the disorder is mostly unknown or varies from case to case. More than 70% of cases are congenital. In some cases, hydrocephalus arises due to physical obstruction manifested by tumors, congenital malformations, or other blockages in normal CSF circulation, which is called non-communicating hydrocephalus. The majority of hydrocephalus belongs to the communicating type, and it is believed to originate due to faulty arachnoid granulations (AGs) which serve as natural valve formations protruding from the meningeal membrane surrounding the brain. Healthy AGs direct CSF along the natural CSF flow pathway, from the subarachnoid space (SAS) of the brain to the superior sagittal sinus (SSS) immediately exterior to the meninges and enclosed within the cranium[7]. However, in cases of communicating hydrocephalus it is believed that these AGs become obstructed leading to the accumulation of CSF and resulting in excessive ICP. Current treatment methods involve implanting a catheter into the ventricles, and a large valve (CSF shunt) under the skin outside the skull, to divert the accumulating CSF through an intracranial and sub-cutaneous long bulky catheter outside of the cranium. The catheter leads to the abdominal cavity or other adsorptive location outside the skull. However, around 40% of these shunts fail within the first 2 years and must be replaced through additional invasive surgeries[5] resulting in potential brain damage. Failure mechanisms include mechanical malfunctions, naturally caused obstructions, infections, subdural hematomas,

blockage, and over/under-drainage. The most commonly reported mechanisms are occlusion, breakage and leakage: all associated with catheters.

As described in the chapter 2 and chapter 3, the previous proposed work directly aimed to address those challenges, by developing catheter-free completely-passive miniaturized valve, which directly lower the possibility of common failure mechanisms of current shunts. The valve restores normal CSF drainage operations by bypassing defective AGs using an artificial arachnoid granulation (aAG). By implanting aAGs in the dura tissue and restore the nature CSF flow pathway, the need for persistent intracranial penetration via catheters to drain CSF outside of the skull is fully eliminated, as the aAG implant restores complete CSF draining functionality within the skull. However, these valves have a few improvement points: i) relatively less implant-friendly geometry for actual implantation in the human brain, which would cause influx of contaminated fluids from the SSS into the SAS. ii) needs to enhance the valve's durability against the CSF flow to compromise long-term reliability. To date, here we propose to advance these fundamental challenges through a simple yet effective ways. The proposed aAG valve is comprised of hydrogel diaphragm structure utilizing the innate liquid-induced swellable behavior of the hydrogel with still following the novelties: i) Non-zero valve-opening pressure ii) Negligible clogging and reverse flow leakage, and iii) Simplicity in design / fabrication process. The work presented in this chapter addresses the challenges by using a glass-based outer frame, instead of the polymer material of the previous valves. The valve is fabricated directly into the glass needle by using the custom-made 3D-printed molds to achieve higher durability of the device by enhancement of adhesion strength with the hydrogel valve structure. The work also aims to direct CSF from SAS to SSS through embedding the implant-friendly structure with the hydrogel valves on meningeal dura mater. For doing that, a PDMS grommet including the hydrogel valves inside is designed and fabricated to prevent unexpected biological contamination in in-vivo implantation environment.

4.2. Material and Methods

Valve design and fabrication. The aAG device is comprised of hydrogel diaphragm structure, for the check valve characteristic to prevent reverse leakage flow, and tubular glass needle to structurally support the hydrogel structure. The device is designed to be implanted on SSS as a bypass of malfunctioning CSF drainage to re-establish CSF flow from SAS into SSS, and its dimension needs to be comparable with the topology of SSS, which has a random topology which has mean diameter of 7.3-8.8 mm; thus the device has 5 mm diameter and 7 mm height . For the functional specification of the valve, it was referenced by traditional shunt systems evaluated by industry standards such as ISO 7197 and ASTM F647; $-200 < \Delta P < 600$ mmH_2O operating pressure range (Chabrerie, 2002; M.Czosnyka, 1997; CzosnykaZ.H.,, 2005), 10~230 mmH_2O of valve-opening pressure and 50 μL/min of the maximum allowable reverse leakage. 3D-printed molds are used for simple fabrication of the hydrogel valve structure and fabricated by using a SLA (Stereolithography Apparatus) type 3D printer (Sparkmaker Original, Sparkmaker). The molds are assembled in the tubular glass needle, then liquid-state hydrogel is poured in it by using a pipette and cured by UV light to be solidified, for 4 mins at 365 nm wavelength. The molds are disassembled after the hydrogel curing, and the cured hydrogel is swollen by dipping in water to be ready for use.

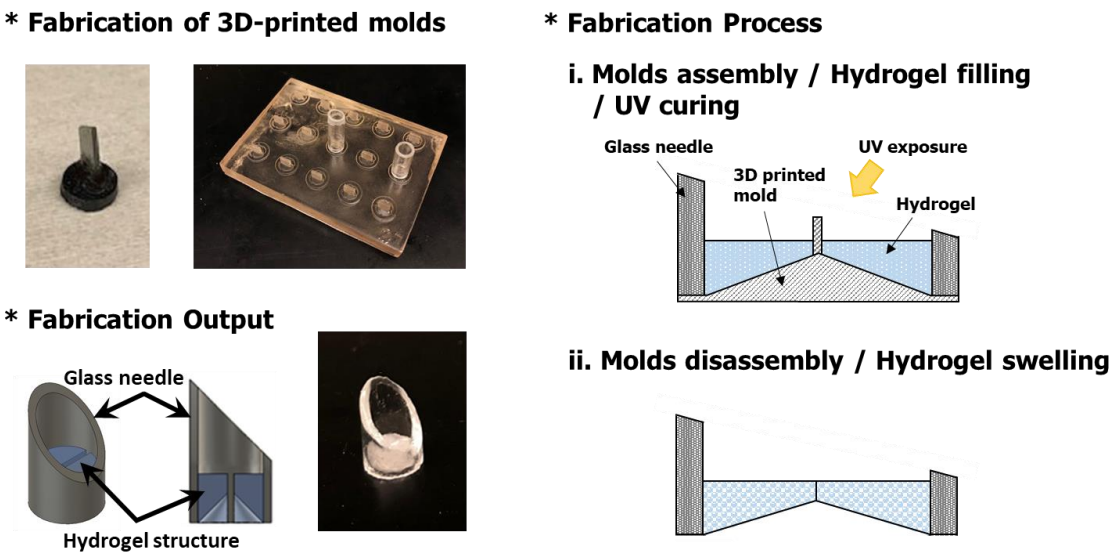

Figure 4.1. Device fabrication process and output results. Schematic of the 3D-printed molds, individual mold and mold array, (left top) and valve fabrication output (left bottom). The valve is composed of a hydrogel and surrounded by the glass needle to support the valve structure. 3D-printed molds are assembled in the needle then the liquid hydrogel solution is cured by UV light for 4 mins at 365 nm wavelength to be solidified. The solidified molds are detached from the hydrogel and submerge the device into the water to prepare for the functionality test (Right).

A PDMS grommet. The hydrogel check-valve has been evaluated and found functionally equivalent to traditional shunts in terms of its hydrodynamic properties meeting the required features mentioned previous sections. However, the hydrogel check-valve is only the operating component for adjustment of excessive CSF, an encapsulating structure coined a grommet may be used to achieve a fully implantable device. A preliminary iteration of this grommet was presented by Schwerdt *et al.* as a simple I-shape PDMS structure, 12 mm in diameter, with a single hydrogel check-valve enclosed

(Schwerdt, 2015). However, the I-shape grommet has some failure points for implantation within the cadaver human brain in terms of relatively big size and low flow rate of excessive CSF drainage. We have designed and fabricated a new type of grommet with fully-realized and surgically friendly structure. The grommet structure incorporates redundancy with two hydrogel check-valves, two CSF inlets, and six suture points, while capitalizing on a cone shape and a removable puncture tool to optimize device implantation (Fig. 4-2). The grommet structure is conical in structure and have at least two hydrogel valves enclosed within it. The conical shape will provide leverage to separate and expand the surgical incision in the dura tissue during implantation. Additionally, the flange on the outer rim of the cone provides numerous suture points for fixation of the grommet in the dura tissue . When the grommet is implanted into the dura the bulk of the conical structure protrudes into SSS, while the flanged side of the grommet remains in SAS. The puncture tool can be placed at the middle of the grommet structure, between the valves, that it protrudes out of the tip of the grommet. Then the cone shape helps to separate and spread the dural tissue after the initial surgical incision through a puncture tool. A puncture tool can be used to place the aAG in the target location and reseal the dural tissue while leaving the aAG. We used customized stainless steel molds to fabricate the proposed grommet design.

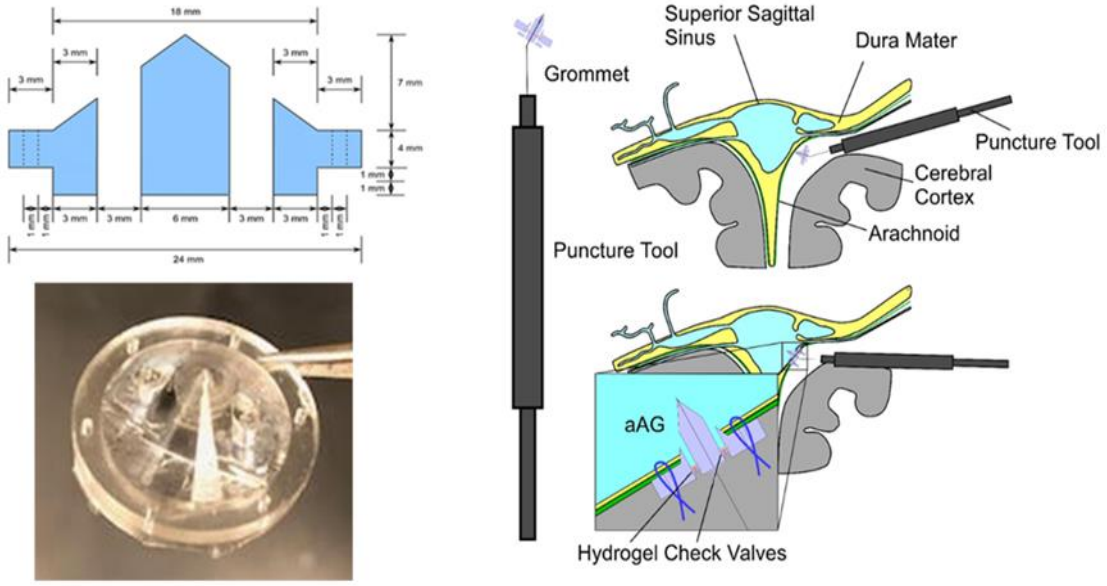

Figure 4.2. Schematic of the proposed PDMS grommet structure (left) and the proposed surgical approach (Right). The implantation tool consists of the aAG placed at the tip of a puncture tool. After the dura has been lifted from the cerebral cortex the puncture tool is inserted into the superior sagittal sinus and is held while sutures are used to secure the aAG.

4.3. Results

Setup for in-vitro sheep brain experiments. The *in-vitro* experimental setup for the evaluation of valve's functionality with the PDMS grommet structure was built on a fixed sheep brain (Bio corporation, Alexandria, MN). The sheep brain was preserved with the dura mater and the excess portion of manual cut was sealed by PDMS to prevent fluid leakage. The hydrogel valve is inserted in the PDMS grommet structure and located onto the designated points of dura mater where we manually punched through by sewing the grommet. A syringe pump (Model 33, Harvard Apparatus) was used to inject CSF into the cavity formed by the valve and SAS. The differential pressure across the valve and

flow rate of CSF were measured by the resistive pressure sensors (PX26-001DV, Omega). All data were collected by a data acquisition board (NI USB 6216, National Instruments) and SignalExpress software (Schwerdt, 2015; Schwerdt, 2013; Lee, 2020).

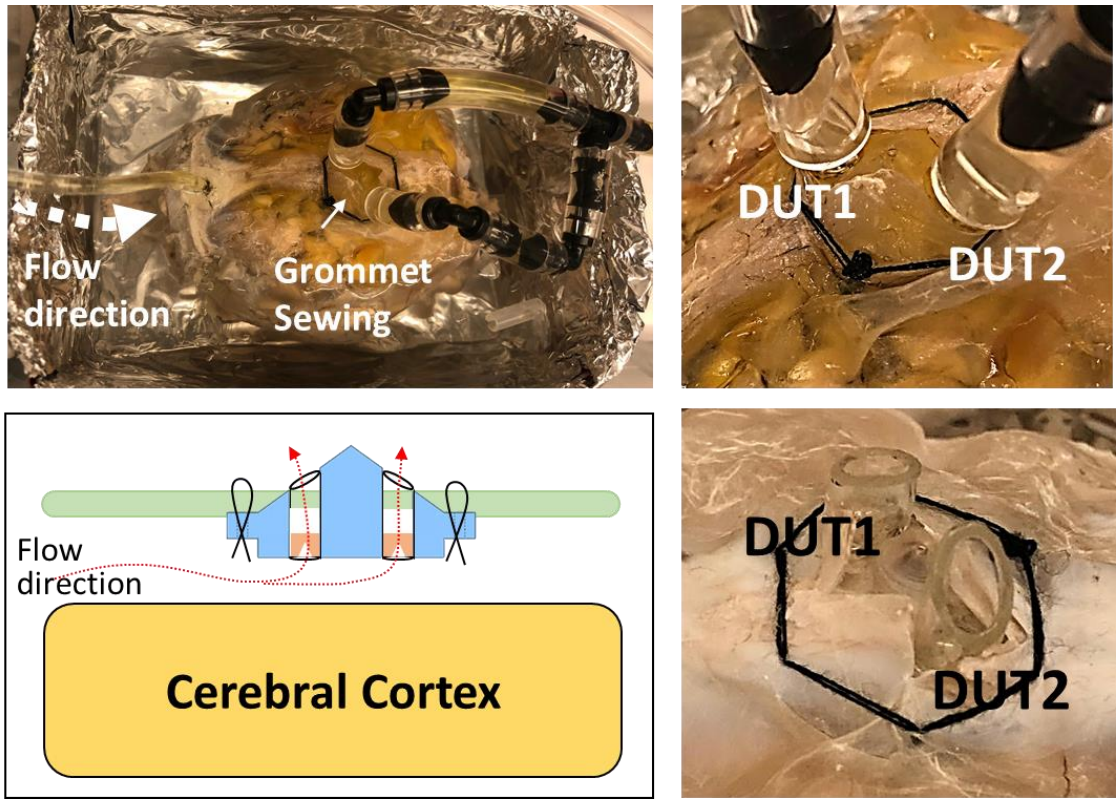

Figure 4.3. In-vitro experiment setup on the sheep brain. The PDMS grommet including two valves is located onto the designated point of the sheep brain by sewing and connected by tubing to measure the differential pressure and flow rate of CSF drained through the valves.

Long-term valve testing. The automated repetitive functional test was performed to evaluate reliability and durability of the hydrogel valve fabricated with the glass needle. A programmable peristaltic pump (P-70, Harvard Apparatus) was used to keep

controlling the fluidic flow with flow rate, flow direction and continuous flow cycles until the valve's operation fails. The valve qualitatively measured the number of valve actuations in real time rather than quantitatively due to the limitations of the laboratory-based environment.

Hydraulic Characteristic of the valve. In addition to the completed the PDMS grommet structure the hydrogel valves have been evaluated the fluidic characteristics when placed inside the grommet structure, thus maintaining the non-zero cracking pressure, and little to no reverse flow leakage characteristics that make the valves ideal for the treatment of hydrocephalus. The basic hydrodynamic measurements show the valve operation within the targeted CSF drainage specifications and predictable behavior with respect to the designed valve geometry with the glass needle, as shown in Figure 4.4.

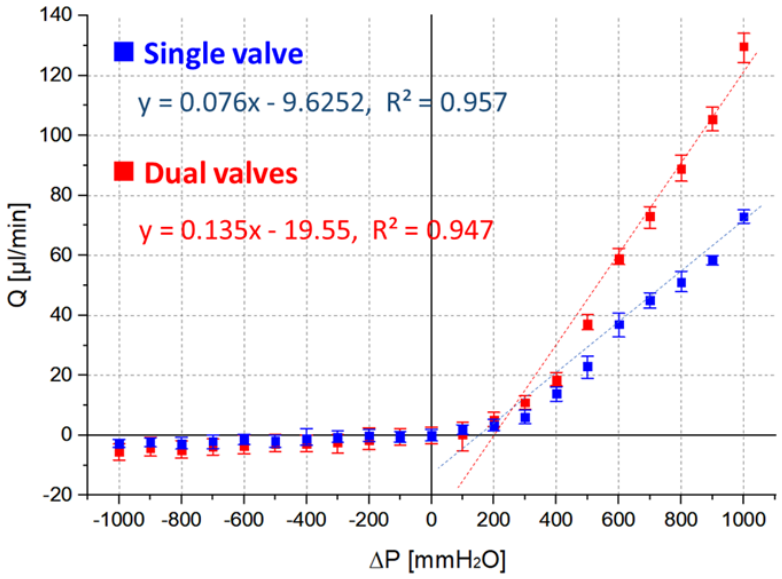

Figure 4.4. Comparison of hydraulic response between single valve vs dual valves (left). The single valve has P_T of 157.0 ± 2.9 mmH_2O and avg. reverse flow leakage of 1.3 µl/min, while the dual valves have P_T of 178.0 ± 5.2 mmH_2O and avg. reverse flow leakage of 3.1 µl/min.

The hydraulic response was measured and compared between using single valve and double valves. In the chapter 2, the previous valve has relatively low flow rates, maximum ~ 98.5 µl/min, in the open-status ($Q_O > 0$) compared to the actual CSF out-flow rates, ranging of 0 ~ 350 µl/min in natural range of CSF drainage (StoneJ.J.,, 2013; CzosnykaZ.H.,, 2005; BrydonHoward, 1996), because the hydraulic resistance of the valve is much higher than that of natural AGs. In order to address the issue, multiple valves were tested simultaneously to ensure that the valves actually drain CSF in an amount equivalent to the number of valves. As expected, the overall flow rate of dual valves is almost two times higher than single valve. The single valve has P_T of 157.0 ±

2.9 mmH_2O and avg. reverse flow leakage of 1.3 μl/min, while the dual valves have P_T of 178.0 ± 5.2 mmH_2O and avg. reverse flow leakage of 3.1 μl/min. Through the result, it can be expected that CSF drainage can be adjustable by using multiple devices in terms of the flow rate at the given differential pressure across the valve, and the lower flow rate issue of the previous devices can be partially mitigated by implanting multiple valves to generate higher CSF out-flow rates to decrease the hydraulic resistance of the valve.

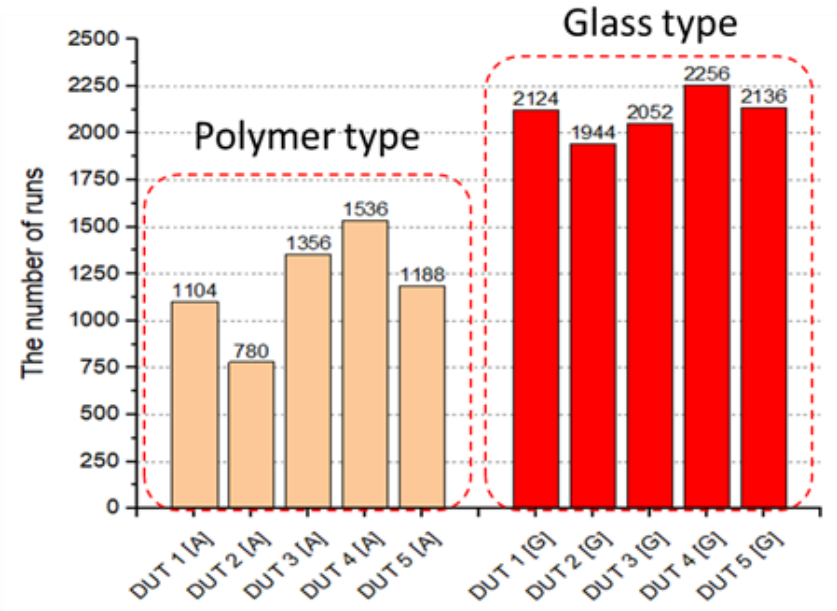

Figure 4.5. Comparison of the valve's long-term functionality between polymer-based and glass-based hydrogel valves. The glass-based devices display much higher running times, ~70%, than the polymer-based devices by increasing durability of the hydrogel valve structure.

Table 4-1. Comparison of Flow Characteristics According to the Material of the Valve's Outer Frame

	Polymer based valves	Glass based valves
Operating cycle	Avg. 1216 runs	Avg. 2104 runs
Cracking pressure	$40.3 < P_T < 53.2$ mmH$_2$O	$52.3 < P_T < 67.1$ mmH$_2$O
Reverse flow leakage	< 0.5 μl/min	< 0.5 μl/min

Comparison data for valve's long-term functionality between polymer-based devices and glass-based devices is shown in figure 4.5. The glass-based devices display much higher running times than the polymer-based devices. It has 2104 running times in average, which is ~ 70% higher than the polymer-based devices, and it can be expected that the increased durability of the hydrogel valve structure affected the results due to the enhanced adhesion strength between the hydrogel structure and the glass needle.

In order to realistically evaluate the hydrogel valve incorporating with the PDMS grommet, the preserved sheep brain was used in a custom-built setup for emulating more physiologically-relevant environment. The grommet containing the hydrogel valves are sutured with the dura layer of the sheep brain so that the CSF pathway passes through the valves surrounded by the grommet structures. Figure 4.6 shows measurements of P_T and flow rate depending on the number of valves encapsulated in the grommet. The result demonstrates the compatibility of the valve with the PDMS grommet maintaining their draining functionality with little degradation in reverse flow sealing features, 0.8 μl/min in average, and reasonable P_T range of $68.2 < P_T < 84.7$ mmH$_2$O. For double valves

(DUT1 + DUT2), the CSF drainage flow increases about 2 times compared to the individual valves (DUT1, DUT2) as expected.

Far thus the valve functionality was established under the grommet encapsulation condition with non-cracking pressure and minimal reverse flow leakage, but the grommet encapsulation still requires more study and evaluation to prove its implantability in terms of biological compatibility and durability. It will be able to be performed by cooperation of in-vivo testing to identify long-term reliability and foreign body response to the valve encapsulated by the grommet. Also, the valve and grommet structure should be downsized to aid in implantation for multidevice usage.

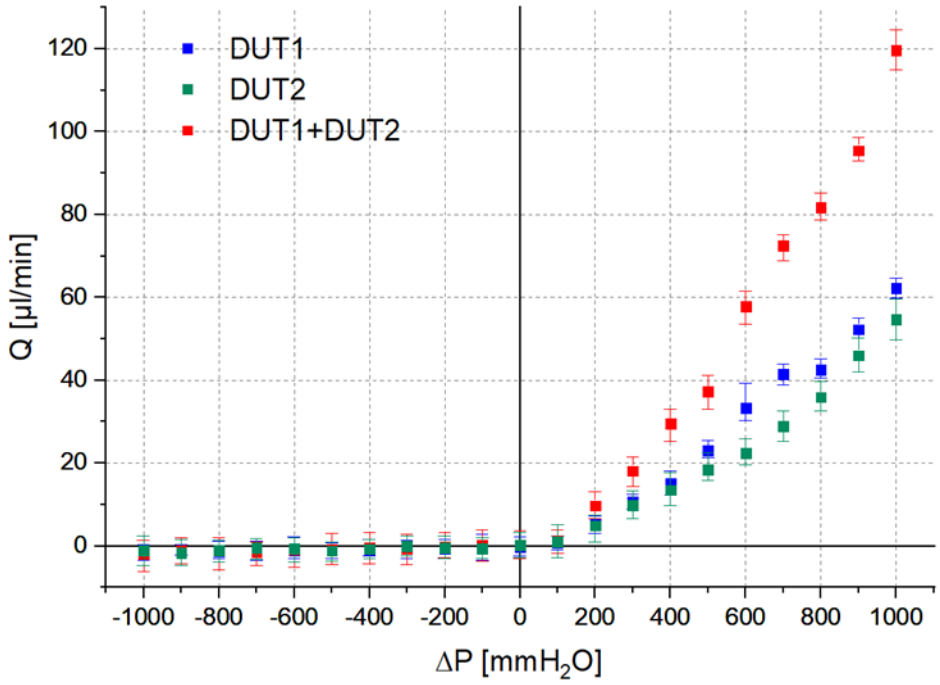

Figure 4.6. Comparison of hydraulic response between individual valve (DUT1, DUT2) vs dual valves (DUT1+DUT2).

4.4. Conclusion

Current cerebrospinal fluid (CSF) shunt treatment has a high failure rate, ~40% within the first 2 years, and 98% within 10 years. These failures lead to high readmission rates and repetitive surgical procedures, resulting in poor quality of life. New treatments are needed to improve the disease burden associated with hydrocephalus. To this end, we have proposed passive valves to replace malfunctioning arachnoid granulations. The proposed valves have catheter-free, completely passive miniaturized valve structure maintaining a consistent and reliable cracking pressure range and little to no reverse flow leakage. The valves also had been evaluated in diverse methods to prove basic functionality, long-term reliability and bio compatibility as a check valve for hydrocephalus treatment, and described the details in previous chapters. The valve described in this chapter is composed of hydrogel diaphragm structure and glass outer frame to address the relatively low durability of the previous devices by enhancing valve's durability against CSF flow through high adhesion strength between hydrogel and glass. The PDMS grommet structure encapsulates valves, provides CSF inlets through the hydrogel valves, suture points, and a cone shape to aid in implantation. We simulated device implantation and evaluated maintaining the non-cracking pressure and little to no reverse leakage flow. The PDMS grommet encapsulating the hydrogel valves remained within design specifications in the physiological experimental model, which used a fixed preserved sheep brain. This evaluation preliminarily validates the hydrogel valve encapsulated by the PDMS grommet structure as an alternative treatment for hydrocephalus paving the way for animal trials.

Chapter 5

5. A fully passive wireless microsystem for a cardiac pacemaker

5.1. Introduction

A pacemaker is an electrical battery-operated medical implant device that delivers electrical pulse signals to the heart to help control abnormal heart rhythms by beating it at a normal rate and pump more effectively. To date, managing heart failure patients with pacemaker transplants has become the primary therapy. Typically, modern pacemakers have two parts, a pulse generator and leads. The pulse generator contains the battery and the programable electrical system that control the heart rate. The leads are typically small wires connected from the pulse generator to the heart to send electrical signals. The first fully implantable pacemaker was developed by Senning in 1958 for cardiac resynchronization therapy (SenningÄke., 1983). Since then, the pacemakers have continued to develop with tremendous advances in the fields of battery and sensor industry with modern advanced semiconductors technology, developing pacemakers more compact, but more efficient. However, despite all the advances, conventional pacemakers face some significant complications associated with finite battery life, ultra-vein pacing leads, and risk of infection from device pockets and leads. To solve these problems, recent advances in power transmission have made bio implantable devices without batteries put into practice (Ebrahim NematiM., 2012). Significantly downsizing devices in millimeters requires the removal of batteries from medical electronic devices, which require technology to transmit power wirelessly to implantable devices. This

wireless technology reduces the risk of infection from machines by eliminating batteries and existing leads and essentially improves the quality of human life.

Fundamentally, the pacemaker detects the electrical signal from the heart and, if the pulse rate is slower than a certain setting value, it applies electrical stimulation to the heart. Then, the heart that received the electrical stimulation contracts, so the heart rate is accelerated. Typically, the heart has two upper and two lower chambers. The upper chamber constricts and draws blood into the lower chamber of the heart. When the ventricles contract, this blood is pushed out of the heart and circulated throughout the body. This contraction is the heartbeat, and electrical signals control the rhythm of the heart beating. The cells in the upper chamber generate these electrical signals and move along the heart to coordinate their activity. In some instances, arrhythmia interferes with electrical signals generation from the heart, causing the heart to beat irregularly, which can lead to symptoms such as fatigue, weakness, fainting, shortness of breath, and chest pain because the heart does not supply blood properly. In severe cases, internal organs may be continuously damaged or even a heart attack may occur. A pacemaker can reduce these symptoms by using electrical pulses to affect the rhythm of the heart. Depending on the different symptoms, a pacemaker can speed up or slow down the heartbeat, alleviating those symptoms. In addition, a pacemaker requires a continuous monitoring system to control the heart rate. Through this, various important health indicators, including basic cardiac activity, can be recorded, and if the heartbeat is not normal according to the recorded information, the electrical pulse of the heart can be automatically adjusted according to the situation.

In order to develop the pacemaker which can be worked in wireless system, wireless fully-passive sensors using radio frequency (RF) microwaves for both of electric signal stimulator and ECG (Electrocardiogram) recorder are described in this chapter. A prototype combined the wireless stimulator and recorder are evaluated in a bench-top experimental setup to show its potential to be used for a pacemaker. The prototype device presents the promising potential of the proposed wireless application for the cardiac pacemaker by demonstrating successful electrical stimulation signaling and recording performance to control abnormal heartbeats.

5.2. Material and Methods

Design for wireless telemetry for the pacemaker system. The term "fully-passive" refers to a specific type of passive system that has no energy source. This means that a fully passive system eliminates the need to regulate or rectify externally generated power to activate the onboard circuits, resulting in a complete rule out of sophisticated and complex circuits. In addition, the fully-passive circuit consumes little or no induced power, thus reducing the risk associated with power consumption of the implant. The first development of the fully-passive wireless sensor for the pacemaker was presented by Schwerdt et al. as a neuropotential recorder by using the RF backscattering methods (Schwerdt et al, 2011).

The device was fabricated by microfabrication technology to minimize footprint and minimize off-chip component count, demonstrating its properties and potential relevance as an implantable sensor. It was also evaluated its potential for neural recording applications through results obtained by recording the frog's nerve potential. The wireless

sensor for the electric signal recording and stimulating for the pacemaker described in this chapter utilize fundamentally the same operating principle of RF backscattering technolgy as the neuropotential recorder. Recently, wireless biomedical devices utilize inductor-based technology to record bioelectric signals externally the human body. These devices use inductive coupling for wireless telemetry, which is a technology that has relatively high efficiency in the low frequency band, below 1 GHz, compared to the EM propagation method of wireless communication using large sized antenna for implantable devices. However, this technique has the disadvantage of being very sensitive to the relative placement of the primary and secondary inductive coils (WanschR., 2002). Especially in the high frequency band above 2 GHz, the induction coil can be replaced by an antenna where RF energy propagates as EM waves. This is because as the frequency increases, the signal experiences more attenuation through the tissue, but the internal efficiency of the antenna also increases at the same time (Abbaspour-TamijaniA., 2008). This tradeoff can have a positive effect on improving the overall efficiency of EM transmission in the high frequency band.

Basically, the wireless system consists of two components for each of recording sensor and stilmulating sensor: 1) the ECG recording and RF backscattering microsystem and 2) the external interrogator to deliver and receive RF microwave.

External interrogator design. The external interrogator is common to both the wireless recorder and stimulator. The interrogator system utilizes the same operating principle as reported by Shiyi et al. for RF backscattered wireless telemetry with the implantable devices (Shiyi, 2017). Figure 5.1 shows the schematic of the external

interrogator. For the stimulator, the pulse modulates 2.4 GHz RF carrier (f_0) through amplitude modulation. The modulated signal (f'_0) is amplified and filtered, then radiated from the external antenna to the stimulator. The pulse and RF carrier were generated by an arbitrary waveform (Agilent 33250A) and RF signal generators (Agilent E4432B), respectively. At the recorder, the modulated RF carrier (f'_0), radiated from the external interrogator, and neuropotentials (f_m) are mixed at the varactor, and this signal has many nonlinear harmonic components. Out of the harmonics, the third-order mixing product ($2f'_0+f_m$) is chosen as the higher signal-to-noise ratio (SNR) and backscattered from the recorder antenna to the external antenna to extract the target neuropotentials (f_m).

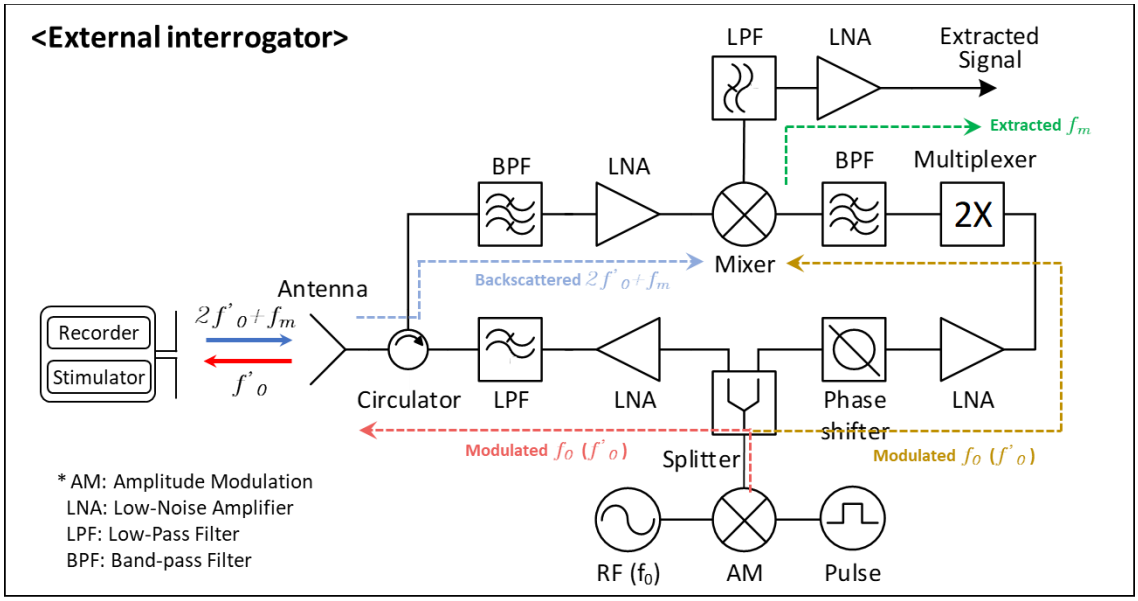

Figure 5.1. The schematic of the external interrogator. The interrogator is common for the recorder and stimulator both for the wireless telemetry utilizing RF backscattering technique.

Recorder design. The equivalent circuit diagram of the wireless fully-passive recorder is shown in figure 5.2. Discrete passive electronic components include a varactor, bypass capacitors C_1 and C_2, a RF choke inductor L_1, a DC block capacitor C_3 and other impedance matching components R_{in}, C_4 and L_2. V_m represents the target neuropotentials. A RF carrier signal (2.4 GHz, f_0) is transmitted from the external interrogator to the implanted recorder. For the high frequency RF signal (f_0) the capacitors C_1 and C_2 are equivalent to short circuits resulting in only the RF carrier (f_0) exciting the varactor diode. The Inductor L_1 isolates the neuropotentials V_m from the RF signal f_0 as an RF choke. On the other hand, the C_1 and C_2 are open circuits while L_1 becomes the short circuit for low frequency neuropotentials (<1000 Hz, f_m), it allows neuropotentials (f_m) to directly reach the varactor diode. Both neuropotentials (f_m) and RF carrier (f_0) appear at the varactor diode, enabling mixing of the two signals. The capacitor C_3 serves as a dc block to protect the neuro cells from the DC component from the varactor. The sensor can have maximum backscattered power through the impedance matching controlled by C_4, L_2 and R_{in}.

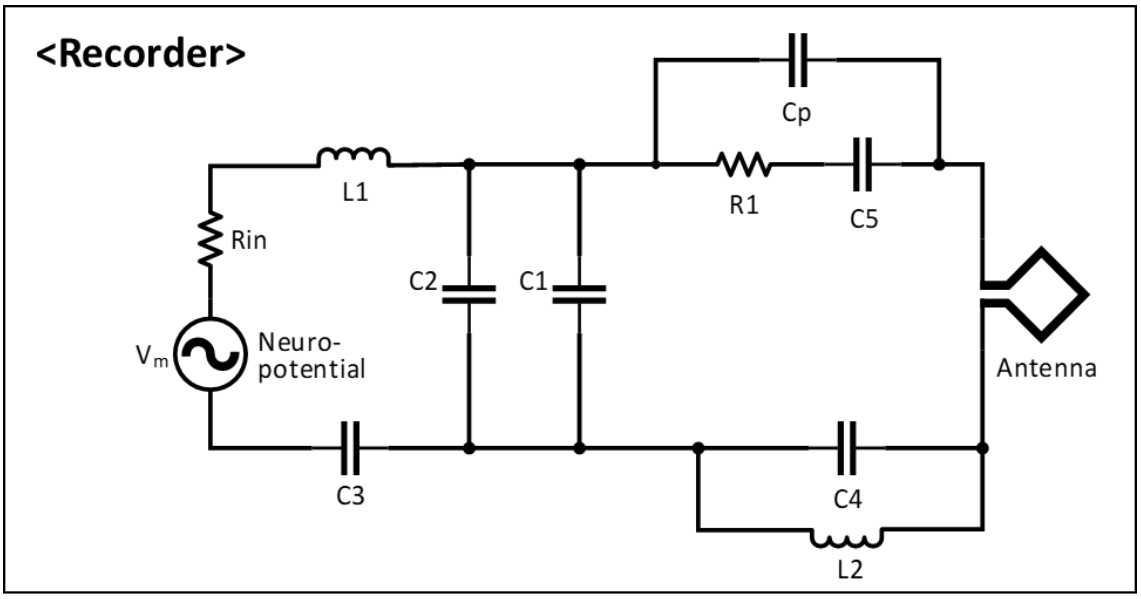

Figure 5.2. The equivalent circuit diagram of the wireless fully-passive recorder.

Stimulator design. The equivalent circuit diagram of the wireless fully-passive stimulator is shown in figure 5.3. The stimulator utilizes multistage diode voltage multipliers to accumulate electric charges. P-channel MOSFET is also used for switching to control the output stimulus. The sensor works in the two states, charging and discharging states, and those states are controlled by the modulated RF pulses radiated from external RF interrogator. The pMOS is turned off in the charging state because the voltage accumulated through the multistage diode voltage multipliers (C_1-C_6 / D_1-D_6) at C_7 is higher than [C_8 || C_9 || C_{10}]. On the other hand, the voltage accumulated at [C_8 || C_9 || C_{10}] is higher than C_7 in the discharging state, which makes the gate-source voltage of the pMOS lower than the thresholds voltage, turning on the pMOS to generate the stimulus. R_1 and R_2 can be controlled for the total power consumption of the circuit. R_3 represents the target cardiac cell.

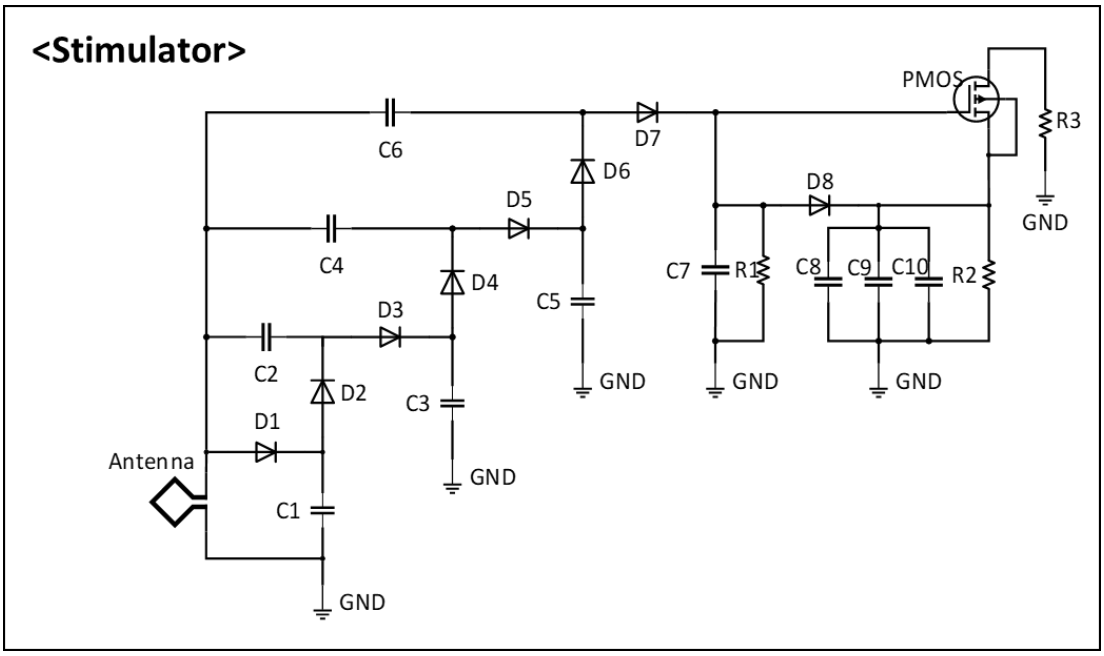

Figure 5.3. The equivalent circuit diagram of the wireless fully-passive stimulator with multistage diode voltage multipliers to accumulate electric charges.

Cardiac Electric Signal Control by LabVIEW. LabVIEW software was used to test the basic performance of the prototype device. In order to control the electric signals for the cardiac pacemaking, LabVIEW software was used to build an algorithm that detects an abnormal ECG signal and delivers the appropriate electrical stimulation signal to the device corresponding to that symptom (Figure 5.4). The electrical signals of the heart are transmitted entirely by wireless communication between devices, and LabVIEW algorithm analyzes those signals and controls the timing of transmission of the corresponding electrical signals. Through the algorithm, it takes ECG input from the function generator (33250A, Agilent) and apply filter onto the input signal to reduce noises. Then the filtered signal is collected by a data acquisition board (NI USB 6216, National Instruments) and checked against conditions to check for the abnormal peaks,

right now abnormal peaks are just any value higher or lower than set boundaries. If the signal is out of boundary, the program will issue an abnormal detection signal. But before issuing this signal, the signal first check if there's another detection signal being issued, if there is, then the program will ignore the detected abnormal peak and continue issuing the detection signal for an amount of time. If there's no detection signal being issued, then the program will set the detection signal to 1 for an amount of time.

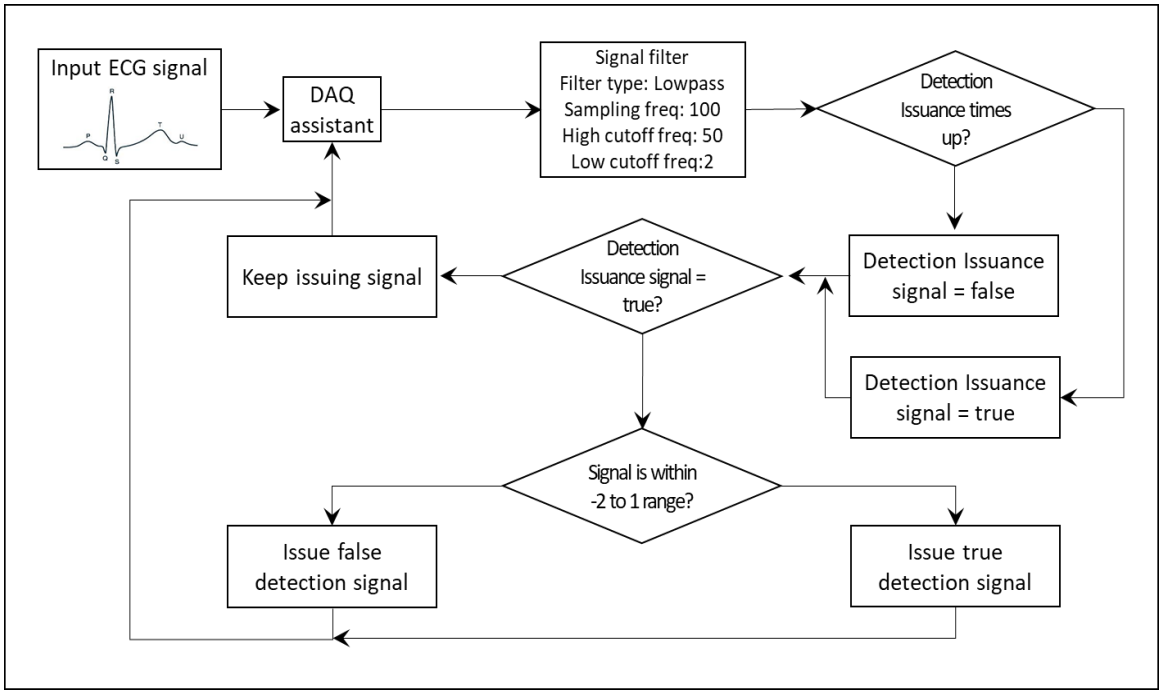

Figure 5.4. The algorithm programmed in LabVIEW software to control cardiac electrical signals and communicate with fully-passive wireless sensors.

5.3. Results

Fig. 5.5 shows the structure of the experimental setup for the basic functional test to evaluate the wireless fully-passive sensors. From the external interrogator part, the pulse and RF carrier were generated by an arbitrary waveform (33250A, Agilent) and RF signal generators (RF function generator E4432B, Agilent), respectively. The pulse signal (6 Vpp / 2 Hz / 2 ms) and 2.3 GHz RF carrier (f_0) signal which is equally divided into two paths through a power splitter. The first path doubles the frequency to be 4.6 GHz ($2f_0$) via a frequency multiplexer for local oscillator (LO) of down-converter. The second path amplifies, filters the RF carrier radiates the signal through a dual-band (2.4 GHz/5 GHz) ceramic chip antenna (A10194, Antenova). Concurrently, the antenna picks up 4.66 GHz ($2f_0 \pm f_m$) backscattered third-order mixing products from the recorder and stimulator which carry target pressure information. The circulator isolates the backscattered signal from the RF carrier. After amplifying and filtering, the third other mixing products ($2f_0 \pm f_m$) mixes with the LO ($2f_0$) to down-convert the output to be f_m. Demodulated signal (f_m) go through filtering and amplifying (SR560, Stanford Research System) and is measured by digital oscilloscope (DPO2024B, Tektronix). The artificial cardiac signal was emulated with 1 Hz and 5 mV_{pp} by the function generator (33250A, Agilent).

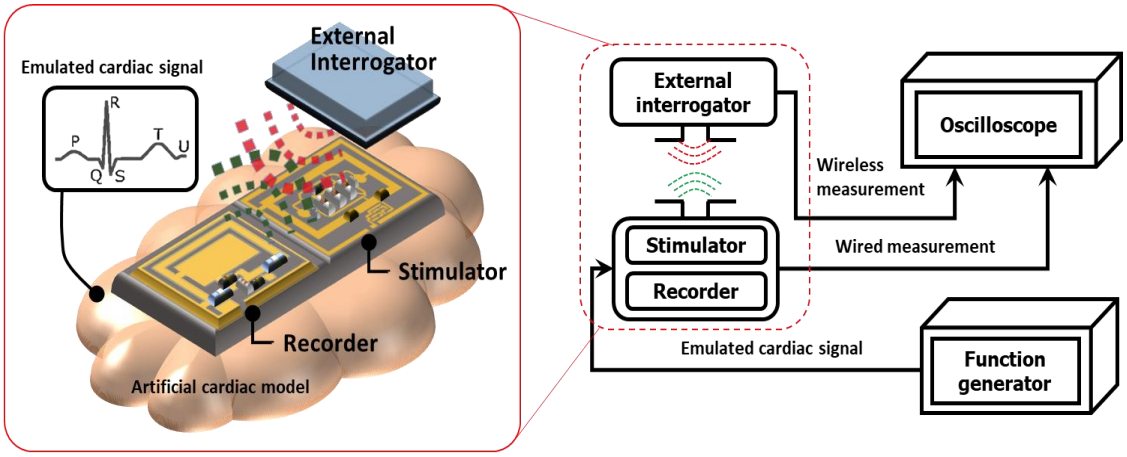

Figure 5.5. Schematic of the bench-top experimental model to evaluate the wireless operation of the recorder and stimulator.

The prototypes of the fully-passive wireless sensors are fabricated on a copper clad polyimide pad, and discrete surface mount electronic components, including varactor diode, resistors inductors and capacitors, are soldered onto the exposed pad. The size of whole devices are 8 mm x 9 mm (W x H) and 20 mm x 13 mm (W x H) for the recorder and stimulator, respectively. Figure 5.6 and 5.7 show the fabrication outputs of the sensors. The detail parameters for the electronic components are shown in table 5.1.

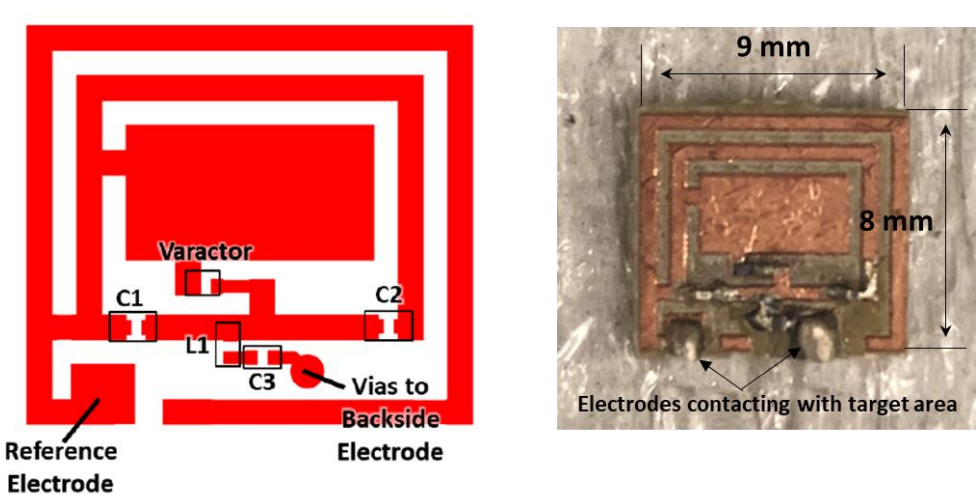

Figure 5.6. Schematic of the wireless recorder (left) and fabrication result on the copper clad polyimide pad (right).

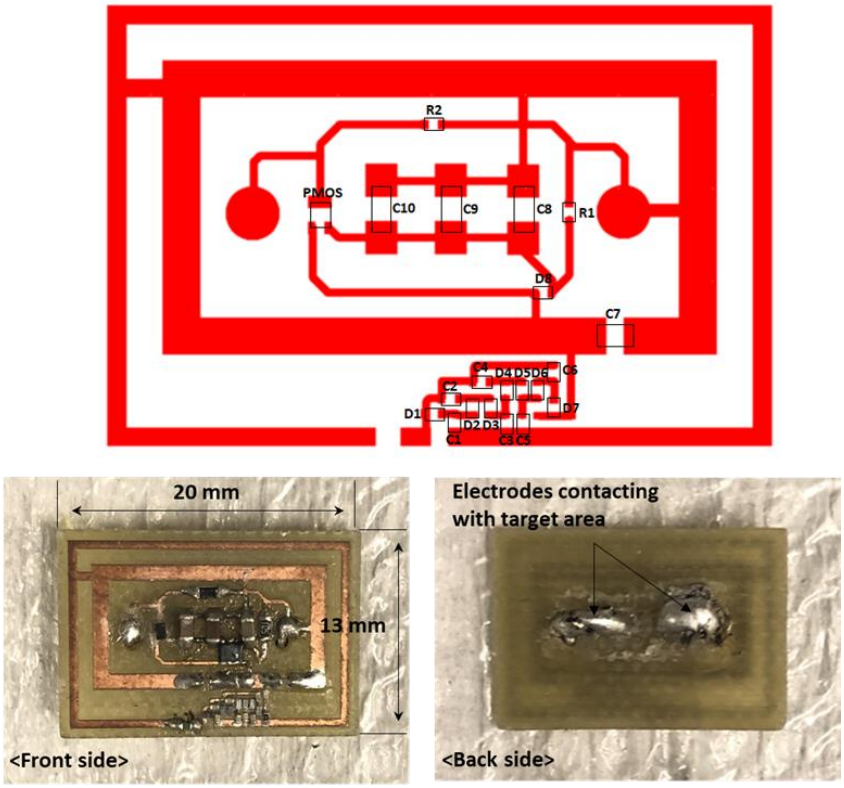

Figure 5.7. Schematic of the wireless stimulator (top) and fabrication result on the copper clad polyimide pad (bottom).

Table 5-1. Detail Parameters of the Electronic Components

Recorder	
Components	Model/Values
Varactor	MA46H120
C1	33 pF
C2	33 pF
C3	4.7 µF
L1	27 nH

Stimulator	
Components	Model/Values
Varactor	MA46H120
C1-C6	1 pF
C7	30 pF
C8-C10	10 µF
R1-R2	50 kΩ
R3	10 kΩ

The artificial ECG signal (1 Hz, 5 mV_{pp}) was simultaneously recorded by wired and wireless system (Figure 5.8). (*General ECG range is 1 - 5 mV for amplitude and 0.5 – 2 Hz for frequency.) The ECG signal was emulated by an arbitrary function generator (33250A, Agilent) and applied on the two electrodes in the wireless fully-passive recording sensor. The output signal in wired system was directly measured between the two electrodes in the sensor. On the other hand, the output signal in wireless system was measured by using external interrogator. The wirelessly recorded signal has some noise and distortion caused by the leakage current of the function generator and environment EM interference. However, the wireless output signal can be advanced by controlling the RF power and external antenna distance. Input and output voltage waveforms of the stimulator were also measured in wireless system and the results are shown in figure 5.8. The input pulse signal was generated by an arbitrary waveform (Agilent 33250A) and set to be 6 V_{pp}, 2 Hz and 2 ms. The input pulse modulates 2.4 GHz RF carrier through amplitude modulation. The modulated signal is amplified, then radiated from the external

antenna to the stimulator. The output voltage was measured between the two electrodes in the stimulator. The output voltage amplitude is 5.8 V_{pp} which is enough to be used for cardiac pacing. (*General range of the pacing voltage amplitude is 0.13 V – 5 V.) The output amplitude can be adjustable by controlling the RF power, pulse amplitude and external antenna distance. For the both functional tests of the recorder and stimulator, the external antenna (A10194, Antenova) was placed 10 mm away from the sensors, and the RF signal generators (E4432B, Agilent) was set by 2.4 GHz and 10 dBm.

After the individual evaluation of each devices, the ECG signal was emulated by an arbitrary function generator (Agilent 33250A) and applied on the two electrodes of the wireless fully-passive sensor combining recorder and stimulator. Both wired and wireless measurements have the stimulus at the point that the input pulse was generated by the wireless stimulator. The peak of the stimulus in wired measurement is out of the display due to its high amplitude much over than the ECG signal measured by the wireless sensor. The signal distortion of the wired measurement is resulted by the leakage current of the function generator used for emulated ECG signal.

The emulated ECG signal was transmitted to LabVIEW algorithm through data acquisition board (NI USB 6216, National Instruments). If the signal is out of the boundary set by the algorithm (-2 V ~ 1 V), the program will issue an abnormal detection signal, ‘1’, and pacing pulse is simultaneously generated with a certain pulse duration.

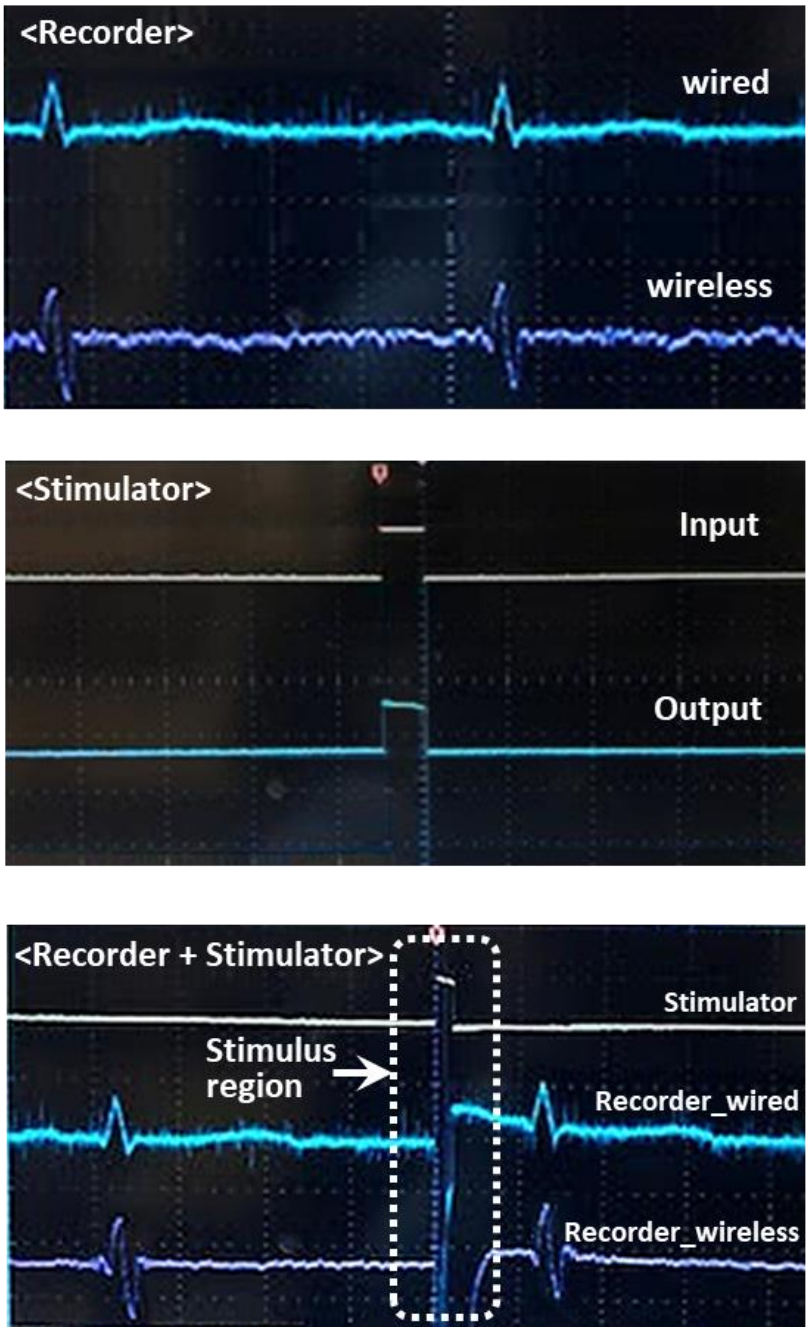

Figure 5.8. Results of the functional test of the fully-passive wireless recorder and stimulator. Electrocardiogram (ECG) signal (1 Hz, 5 mV_{pp}) was simultaneously recorded by wired and wireless system (top). Input and output voltage waveforms of the stimulator in wireless system (middle). The emulated ECG signal (1 Hz, 5 mV_{pp}) with stimulus

applied by wirelessly radiated pulse from external interrogator. (Yellow: Wirelessly transmitted electrical pulse stimulation, Blue: ECG recorded by wired system, Purple: ECG recorded by wireless fully-passive sensor)

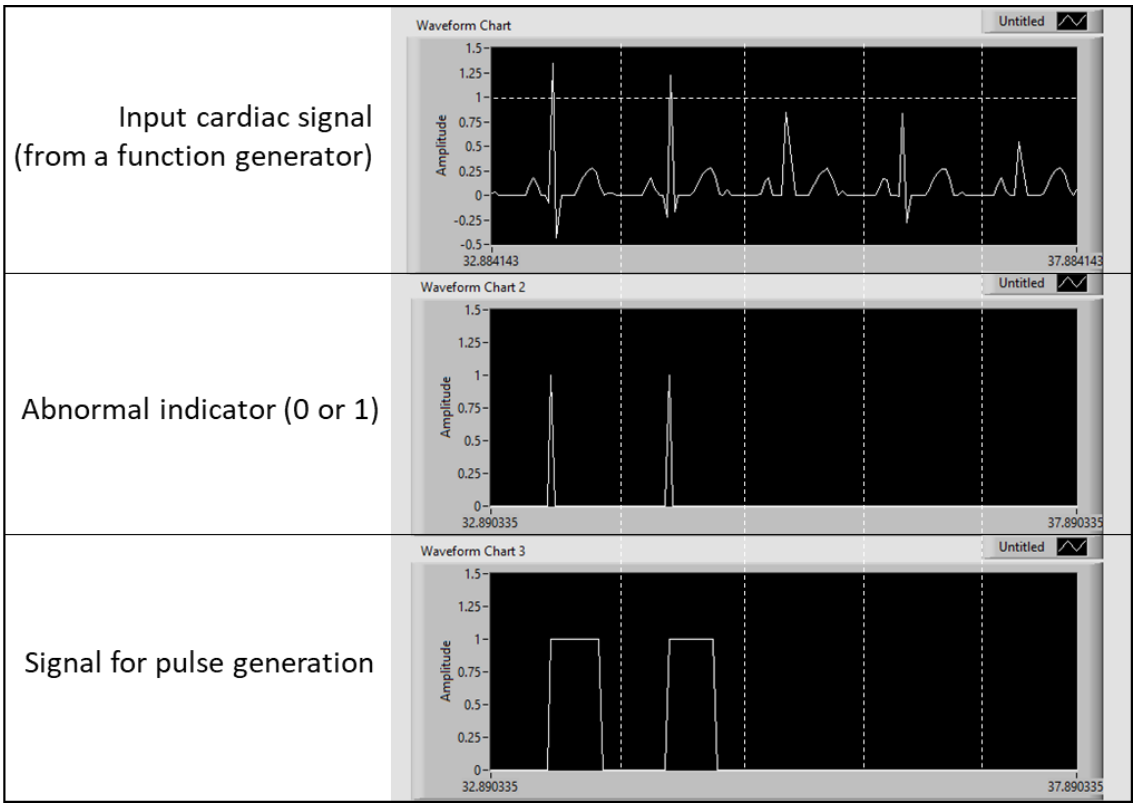

Figure 5.9. Results for abnormal ECG detection of the LabVIEW algorithm.

5.4. Discussion

In this chapter, fully-passive wireless sensors were described as a prototype for a pacemaker that record the ECG signals and also provide appropriate electrical stimulation signals in case of heartbeat abnormalities in wireless system. The operation principles of each device were referenced by the previous work done by former group members (Shiyi, 2017; H.N.Schwerdt, 2011). The device performs wireless telemetry with an external

interrogator for signal modulation using the RF backscatter method. The basic functional test demonstrates the device's ability to successfully acquire ECG signals wirelessly and deliver electrical pulsed stimuli in a completely passive manner without batteries.

At this stage, the prototype devices were fabricated on the solid copper clad polyimide pad. However, the fabrication process will be performed on a flexible substrate, i.e. thin polyimide film, for practical use in the future or for in-vitro / in-vivo biological evaluation of the wireless system in the near future. The in-vitro or in-vivo tests for the device evaluation is supposed to be performed to prove its biocompatibility and functional reliability as a biomedical device. In this respect, careful material selection for device fabrication and sterilization or additional coating processes to prevent biological and physiological contamination must be considered. The size of the device is also one of the main challenges in combining the recorder and stimulator for practical use in cardiac pacemaker. Future work will focus on decreasing the size of the system with keeping or increasing the sensitivity. The simplicity of the wireless microsystem relies on its fully-passive operation and several components for it. Therefore, additional size reduction must be realized in the step of the external receiver system design including antenna design process. Another major work which should be performed for the next step is to build software algorithm to control the electric signals. The process of identifying abnormal ECG signals due to cardiac dysfunction rather than a single transient symptom and delivering electrical pulse signals corresponding to the detected heart disease at appropriate time intervals are essential functions of a pacemaker. Hence, the LabVIEW algorithm is as much an important part of this research as device development. A list of ECG signal characteristics corresponding to various heart conditions requiring

pacemaking is already established in existing pacemaker products, and there are many open sources for programming their algorithms. Such algorithms can be referenced using various software and are expected to be easily applied to our wireless system.

REFERENCES

Acar, C. (2009). Environmentally robust MEMS vibratory gyroscopes for automotive applications. *IEEE Sensors Journal*, 1895-1906.

Au, A. K. (2011). Microvalves and micropumps for BioMEMS. *Micromachines*, 179-220.

Bashir, R. (2004). BioMEMS: state-of-the-art in detection, opportunities and prospects. *Advanced drug delivery reviews*, 1565-1586.

Beems, T. (2003). Serum-and CSF-concentrations of brain specific proteins in hydrocephalus . *Acta neurochirurgica*, 37-43.

Benabid, A.-L. (1987). Combined (thalamotomy and stimulation) stereotactic surgery of the VIM thalamic nucleus for bilateral Parkinson disease. *Stereotactic and functional neurosurgery* , 344-346.

Boddu, S. G. (2018). Anatomic measurements of cerebral venous sinuses in idiopathic intracranial hypertension patients. *PloS one*.

Bogue, R. (2013). Recent developments in MEMS sensors: A review of applications, markets and technologies. *Sensor review*.

Bose, S. S. (2013). Bone tissue engineering using 3D printing . *Materials today* , 496-504.

Brodbelt. (2007). CSF pathways: a review. *Brit. J. Neurosurg*, 510-520.

Bronzino, J. D. (2016). *Tissue engineering and artificial organs.* CRC press.

Brydon, H. L. (1996). Reduced bacterial adhesion to hydrocephalus shunt catheters mediated by cerebrospinal fluid proteins . *Journal of Neurology, Neurosurgery & Psychiatry* , 671-675.

Chabrerie, A. (2002). Ventricular shunts. *Journal of Intensive Care Medicine*, 218-229.

Chen, P. R. (2007). Surface-micromachined parylene dual valves for on-chip unpowered microflow regulation. *Journal of Microelectromechanical Systems*, 223-231.

Cheung, K. C. (2006). BioMEMS for medicine: On-chip cell characterization and implantable microelectrodes. *Solid-State Electronics*, 551-557.

Chung, S. J.-C.-K. (2003). Development of MEMS-based cerebrospinal fluid shunt system. *Biomedical Microdevices(2003)*, 311-321.

Ciuti, G. (2015). MEMS sensor technologies for human centred applications in healthcare, physical activities, safety and environmental sensing: a review on research activities in Italy. *Sensors*, 6441-6468.

Codman. (2014, October 4). *Hydrocephalus Catalog*. Retrieved from http://implantesclp.com/uploads/pdf/Codman. pdf.

Czosnyka, M. C. (1997). Hydrodynamic properties of hydrocephalus shunts: United Kingdom shunt evaluation laboratory. *Journal of Neurology, Neurosurgery & Psychiatry*, 43-50.

Czosnyka, Z. C. (2005). Hydrocephalus shunts and waves of intracranial pressure. *Medical and Biological Engineering and Computing*, 71-77.

Del Bigio, M. R. (2015). Nonsurgical therapy for hydrocephalus: a comprehensive and critical review . *Fluids and Barriers of the CNS* .

Dolle, S. (2013, September). *CNS Shunt Monitoring and In-Vivo Shunt Prediction with the DiaCeph Test, ICP Taps, and Bench Tests*. Retrieved from http://www.dollecommunications.com/Shunt-Selection-Method.htm

Drake. (2000). CSF shunts 50 years on–past, present and future. *Child's Nervous System*, 800-804.

Drake, J. K. (1998). Randomized trial of cerebrospinal fluid shunt valve design in pediatric hydrocephalus. *Neurosurgery*, 294-303.

El-Shafei. (2001). The retrograde ventriculosinus shunt: concept and technique for treatment of hydrocephalus by shunting the cerebrospinal fluid to the superior sagittal sinus against the direction of blood flow. *Child's nervous system*, 457-465.

Eric Mounier. (2018). *Status of the MEMS Industry 2018 - Yole Développement.* Yole Développement.

FDA. (2019, August 21). *MED-EL Cochlear Implant System - P000025/S104*. Retrieved from FDA: https://www.fda.gov/medical-devices/recently-approved-devices/med-el-cochlear-implant-system-p000025s104

Fetalhydrocephalus. (2020). *A frontal shunt placement*. Retrieved from http://fetalhydrocephalus.com/hydro/Shunts.aspx

FiorMarkets. (2020). Wearable Artificial Organs Market by Product (Vision Bionics, Brain Bionics, Bionic Limbs, Exoskeleton, Cochlear Implants, Pancreas, Kidney), Technology (Electronic, Mechanical), Region, Global Industry Analysis, Market Size, Share, Growth, Trends, and Fo. *Fior Markets*.

Flader. (2019). Micro-tethering for fabrication of encapsulated inertial sensors with high sensitivity. *J. Microelectromech. Syst.*, 372-381.

Grayson, A. C. (2004). A BioMEMS review: MEMS technology for physiologically integrated devices. (pp. 6-21). IEEE.

Greatbatch, W. (1991). History of implantable devices. *IEEE Engineering in Medicine and Biology Magazine*, 38-41.

H.N., Schwerdt. (2011). A Fully-Passive Wireless Microsystem for Recording of Neuropotentials using RF Backscattering Methods. *J. Microelectromechanical Syst. Jt. IEEE ASME Publ. Microstruct. Microactuators Microsens. Microsyst.*, 1119–1130.

Healthwise. (2020, May). *Congenital hydrocephalus*. Retrieved from https://www.uvmhealth.org/healthwise/topic/tp12484

Huff, C. (2020, March 11). *How artificial kidneys and miniaturized dialysis could save millions of lives*. Retrieved from Nature: https://www.nature.com/articles/d41586-020-00671-8

J. Tir´en, L. T. (1989). A batch-fabricated non-reverse valve with cantilever beam manufactured by micromachining of silicon. *Sens. Actuators*, 389-396.

Kim. (2011). Epidermal electronics. *science*, 838-843.

Kim, A. (2015). New and emerging energy sources for implantable wireless microdevices. *IEEE Access*, 89-98.

Kim, D. (2007). A bi-polymer micro one-way valve. *Sensors and Actuators A: Physical*, 426-433.

Kirkpatrick. (1989). Symptoms and signs of progressive hydrocephalus. *Archives of disease in childhood*, 124-128.

Klarica, M. R. (2014). The influence of body position on cerebrospinal fluid pressure gradient and movement in cats with normal and impaired craniospinal communication. *PLoS One* .

Knapp, A. (2020, March 27th). *AbCellera Raises $105 Million To Boost Drug Discovery Against Coronavirus And Other Diseases*. Retrieved from Forbes: https://www.forbes.com/sites/alexknapp/2020/05/27/abcellera-raises-105-million-to-boost-drug-discovery-against-coronavirus-and-other-diseases/#73b1786a2a6c

Ko, W. H. (2012). Early history and challenges of implantable electronics. *ACM Journal on Emerging Technologies in Computing Systems (JETC)*, 1-9.

Kraft, M. (2013). *MEMS for automotive and aerospace applications.* Elsevier.

Lee. (2013). Fabrication of a 3 dimensional dielectrophoresis electrode by a metal inkjet printing method. *Micro and Nano Systems Letters*, 1-7.

Lee. (2020). Three-Dimensionally Printed Microelectromechanical-System Hydrogel Valve for Communicating Hydrocephalus. *ACS sensors*, 1398-1404.

Lo. (2008). A refillable microfabricated drug delivery device for treatment of ocular diseases. *Lab on a Chip*, 1027-1030.

Lo, R. L. (2009). A passive MEMS drug delivery pump for treatment of ocular diseases. *Biomedical microdevices*, 959-970.

Luo, Y. H.-L. (2014). A review and update on the current status of retinal prostheses (bionic eye). *British medical bulletin*, 31-44.

Lyshevski, S. E. (2018). *MEMS and NEMS: systems, devices, and structures.* CRC Press.

MarketWactch. (2020). *Brain Bionics Market 2020 - Impact of Covid 19 on Industry Share, Size, Price, CAGR, Growth Rate and Future Prospects.* MarketWactch.

Mateescu, A. W. (2012). Thin hydrogel films for optical biosensor applications. *Membranes*, 40-69.

Medtronic. (2012, October 8). *Neurological Products: Shunts*. Retrieved from http://www.medtronic.com/for-healthcare-professionals/products-therapies/neurological/shunts/index.htm

Mehregany, M. (1999). *Introduction to MEMS.*

Meinhart, C. D. (2000). The flow structure inside a microfabricated inkjet printhead. *Journal of microelectromechanical systems* , 67-75.

Moon, S. I. (2012). Selectively bonded polymeric glaucoma drainage device for reliable regulation of intraocular pressure. *Biomedical microdevices*, 325-335.

MordorIntelligence. (2019). *Bio-MEMS Market - Growth, Trends, and Forecasts (2020 - 2025).* Mordor Intelligence.

Morgan, A. J. (2016). Simple and versatile 3D printed microfluidics using fused filament fabrication . *PloS one* .

Mysid. (2010, May 30). *Arachnoid granulation*. Retrieved from Wikimedia: https://en.wikipedia.org/wiki/Arachnoid_granulation#:~:text=Arachnoid%20granulations%20(also%20arachnoid%20villi,(the%20thick%20outer%20layer).

NINDS. (2012). *Hydrocephalus fact sheet.* NIH Publication.

Nitzan, S., Zega, V., Li, M., Ahn, C., Corigliano, A., Kenny, T., & Horsley, D. (2015). Self-induced parametric amplification arising from nonlinear elastic coupling in a micromechanical resonating disk gyroscope. *Sci. Rep*.

Oh, J. K. (2011). Design and Fabrication of a PDMS/Parylene Microvalve for the Treatment of Hydrocephalus. *Journal of Microelectromechanical Systems*, 811-818.

Oh, K. (2006). A review of microvalves. *Journal of micromechanics and microengineering*.

Oliveira, M. T. (2015). Surgical technique of retrograde ventricle-sinus shunt is an option for the treatment of hydrocephalus in infants after surgical repair of myelomeningocele. *Arquivos de neuro-psiquiatria*, 1019-1025.

Oliveira, M. T. (2017). Revisiting Retrograde Ventriculosinus Shunt as an Alternative for Treating Hydrocephalus in Children. *Arquivos Brasileiros de Neurocirurgia: Brazilian Neurosurgery*, 108-116.

Onuki, Y. (2008). A review of the biocompatibility of implantable devices: current challenges to overcome foreign body response. 1003-1015.

Polla, D. L. (2001). BioMEMS applications in medicine. *International Symposium on Micromechatronics and Human Science.* IEEE.

R Wang, A. L.-K. (2011). Regenerative Surface Plasmon Resonance (SPR) biosensor: Real-time measurement of fibrinogen in undiluted human serum using the competitive adsorption of proteins. *Biosensors and Bioelectronics*, 304-307.

Reddy, G. K. (2014). Long-term outcomes of ventriculoperitoneal shunt surgery in patients with hydrocephalus. *World Neurosurgery*, 404-410.

Rengier, F. (2010). 3D printing based on imaging data: review of medical applications. *International journal of computer assisted radiology and surgery*, 335-341.

S Choi, J. C. (2009). A regenerative biosensing surface in microfluidics using electrochemical desorption of short-chain self-assembled monolayer. *Microfluidics and nanofluidics*, 819-827.

Saliterman, S. (2006). *Fundamentals of BioMEMS and medical microdevices.* SPIE press.

Sanders, D. (2009). Introducing AI into MEMS can lead us to brain-computer interfaces and super-human intelligence. *Assembly Automation*.

Schoebel, J. (2005). Design considerations and technology assessment of phased-array antenna systems with RF MEMS for automotive radar applications. *IEEE Transactions on Microwave Theory and Techniques*, 1968-1975.

Schwerdt. (2013). Miniaturized passive hydrogel check valve for hydrocephalus treatment. *IEEE Transactions on Biomedical Engineering*, 814-820.

Schwerdt. (2015). In vitro hydrodynamic, transient, and overtime performance of a miniaturized valve for hydrocephalus. *Annals of biomedical engineering*, 603-615.

Schwerdt. (2011). A Fully Passive Wireless Microsystem for Recording of Neuropotentials Using RF Backscattering Methods. *JOURNAL OF MICROELECTROMECHANICAL SYSTEMS*, 1119-1130.

Seshia, A., Palaniapan, M., Roessig, T., Howe, R., Gooch, R., Schimert, T., & Montague, S. (2002). A vacuum packaged surface micromachined resonant accelerometer. *J. Microelectromech. Syst*, 784-793.

Shin, D., Ahn, C., Chen, Y., Christensen, D., Flader, I., & Kenny, T. (2017). Environmentally robust differential resonant accelerometer in a wafer-scale encapsulation process. *IEEE 30th International Conference on Micro Electro Mechanical Systems (MEMS)*, (pp. 17-20). Las Vegas.

Shiyi Liu. (2017). Wireless Passive Stimulation of Engineered Cardiac Tissues. *ACS sensors*, 1006-1012.

Slaughter, G. (2015). Enzymatic glucose biofuel cell and its application. *Journal of Biochips & Tissue Chips*.

Stone, J. W. (2013). Revision rate of pediatric ventriculoperitoneal shunts after 15 years. *Journal of Neurosurgery*, 15-19.

Suh, J., & Christie, B. (2014, June 5). *Futurescope: From lab-grown lungs to mechanical eyes, the latest and most realistic artificial body parts Infographic.* Retrieved from New York Magazine: https://nymag.com/health/bestdoctors/2014/artificial-body-parts-2014-6/

Suzuki, Y. (2011). Recent progress in MEMS electret generator for energy harvesting. *IEEJ Transactions on Electrical and Electronic Engineering*, 101-111.

Technavio. (2018). *Integrating Nanotechnology with Bio-MEMS to Change the Medical and Healthcare Industry | Technavio.*

Tiren, J. L. (1989). A batch-fabricated non-reverse valve with cantilever beam manufactured by micromachining of silicon. *Sensors and Actuators*, 389-396.

Torchilin, V. (2014). *Handbook of Nanobiomedical Research: Fundamentals, Applications, and Recent Developments. Vol. 3.* World scientific.

Understanding Hydrocephalus. (2019). Retrieved from http://www.integralife.com/file/general/1571412375.pdf

Van Canneyt, K. K. (2008). Experimental and numerical modelling of the ventriculosinus shunt (El-Shafei shunt). *Proceedings of the Institution of Mechanical Engineers, Part H: Journal of Engineering in Medicine*, 455-464.

Velten, T. (2005). Packaging of bio-MEMS: strategies, technologies, and applications. *IEEE Transactions on Advanced Packaging*, 533-546.

Verrees. (2004). Management of normal pressure hydrocephalus. *American Family Physician*, 1071-1090.

Verrees, M. (2004). Management of normal pressure hydrocephalus. *American Family Physician*, 1071-1078.

Viker, T. (American Society of Mechanical Engineers,). Modular Redundancy for Cerebrospinal Fluid Shunts: Reducing Incidence of Failure due to Catheter Obstruction. *Frontiers in Biomedical Devices.* .

Vinje, V. E. (2019). Intracranial pressure elevation alters CSF clearance pathways. *bioRxiv*.

Wilson, B. S. (2003). Cochlear implants: some likely next steps. *Annual Review of Biomedical Engineering*, 207-249.

Wilson, K. P. (2007). Integration of functional myotubes with a Bio-MEMS device for non-invasive interrogation. *Lab on a Chip*, 920-922.

Wise, K. D. (2007). Integrated sensors, MEMS, and microsystems: Reflections on a fantastic voyage. *Sensors and Actuators A: Physical*, 39-50.

Yole Development. (2016). *MEMS & Sensor Roadmap.* Yole Development.

Yole Development. (2019). *2019-2025 MEMS market forecasts by end-market.* Yole Development.

YoleDevelopment. (2020). *COVID-19 impact: the different bioMEMS devices growth rate between 2019 and 2020.* Yole Development.

Ziaie, B. (2004). Hard and soft micromachining for BioMEMS: review of techniques and examples of applications in microfluidics and drug delivery. *Advanced drug delivery reviews*, 145-172.

APPENDIX A

STANDARD OPERATION PROCEDURE OF HYDROGEL CHECK VALVE RESEARCH FOR HYDROCEPHALUS TREATMENT

❖ Fabrication

- Hydrogel preparation

- Mix hydrogel solutions:

  2-hydroxyethyl methacrylate (HEMA), 1 part (typically, 6 mL)

  ethylene glycol dimethacrylate (EGDA), 0.04 part (typically 0.25 mL)

  2,2-dimethoxy-2-phenylacetophenone (DMPA), 0.1 part (typically, 0.6 gram)

- Valve fabrication (Acrylic plate version)

- Prepare acrylic plate: drill a hole at the center (ϕ 3~5 mm)

- Prepare 3D-printed molds and apply vacuum grease to the molds to prevent unexpected breakage of the solidified hydrogel when you detach the 3D-printed molds after UV curing step.

- Assemble the 3D-printed molds to the hole of the acrylic plate

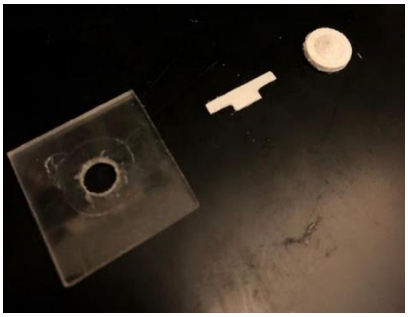
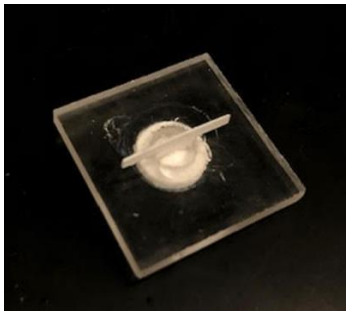

- Pour the hydrogel at the hole until the empty space is full (Beware of air bubbles)

- Expose to UV (long wavelength (365nm)) for 4 - 8 mins in a dark room

- Disassemble the 3D-printed molds from the acrylic plate (Caution for breakage of solidified hydrogel structure)

- Soak the device in water overnight to swell the hydrogel

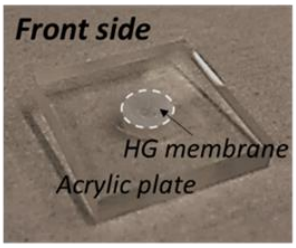

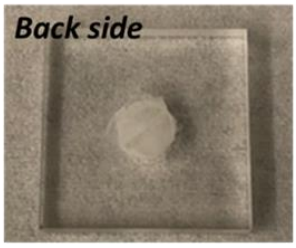

- Valve fabrication (Glass needle version)
- Prepare a glass needle (I.D: 4 mm)
- Prepare 3D-printed molds and apply vacuum grease to the molds to prevent unexpected breakage of the solidified hydrogel when you detach the 3D-printed molds after UV curing step. (Ultimaker 2 Go)
- Assemble the 3D-printed molds to bottom of the glass needle
- Pour the hydrogel into the assembled glass needle (30 ul) (Beware of air bubbles)

  * The volume of the hydrogel solution will be different depending on the size of the glass needle.

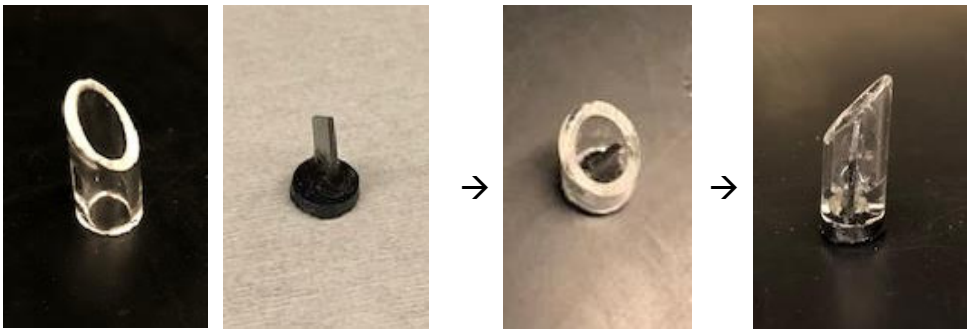

- Expose to UV (long wavelength) for 4 - 8 mins in a dark room
- Disassemble the 3D-printed molds from the glass needle (Caution for breakage of solidified hydrogel structure)
- Soak the device in water overnight to swell the hydrogel

  * Another 3D-printed molds (Sparkmaker Original, Sparkmaker)
    - Fabrication process is same as well.

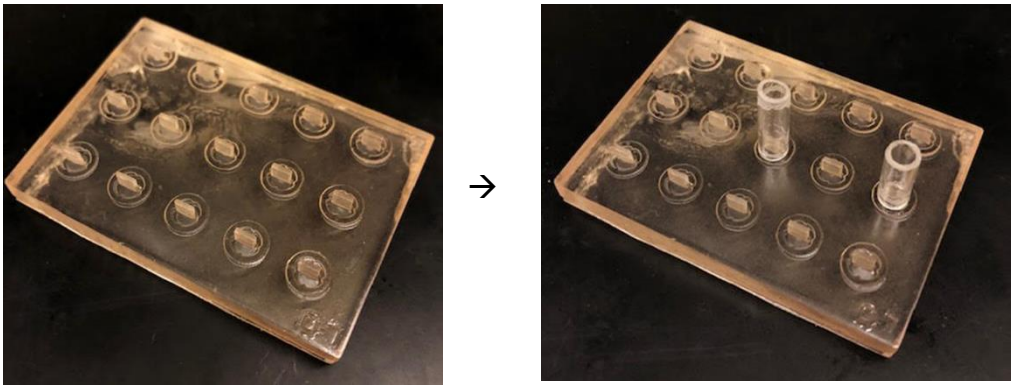

❖ Experimental Setup

- Bench-top test setup

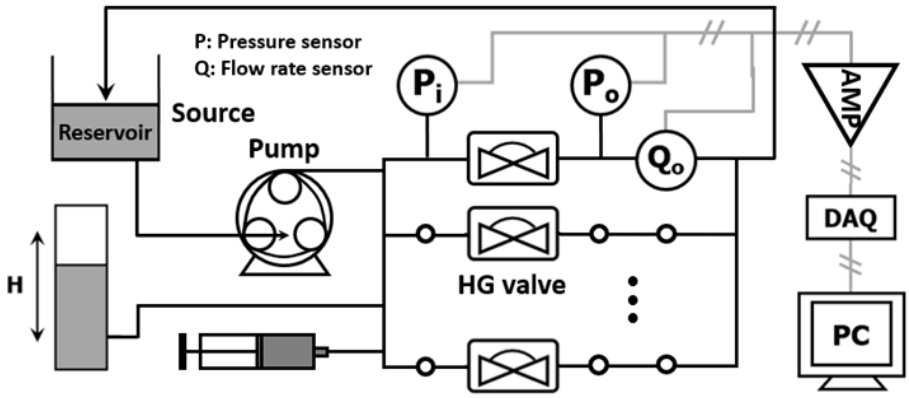

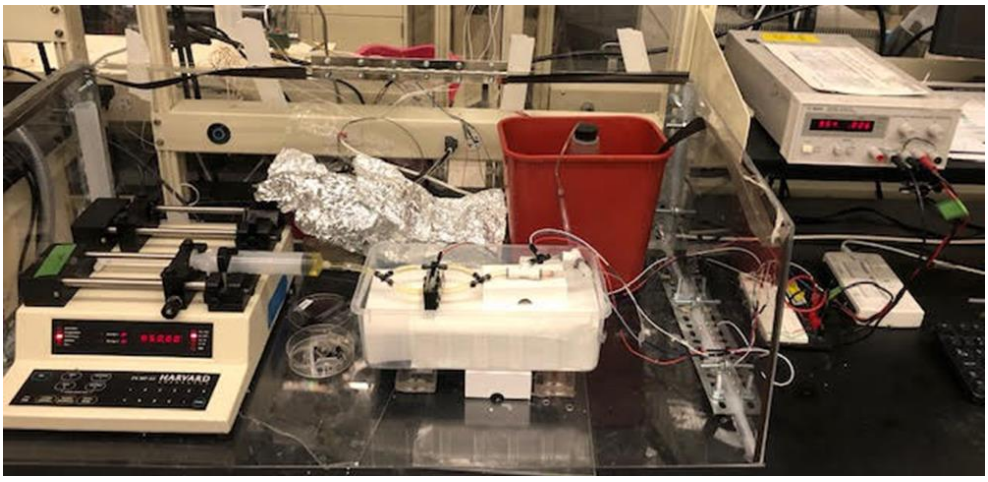

- Fluid source

  Syringe pump (Model 33 syringe pump, Harvard Apparatus)

* Flow rate setup:

  [Set] button -> [Rate1] button -> Set flow rate value -> [Enter] button

* Flow rate unit change:

  [Set] button -> [Rate1] button -> [Rate1] button -> [Rate1] button -> … -> Set flow rate value -> [Enter] button

- Sandwich-type connecting module

  Sandwich-type connecting module is constructed using two acrylic plates with a hole at the center and two rubber O-rings, each placed between the acrylic plates and respective side of the valve. The module sealing is performed by aligning the holes of the acrylic plates with rubber O-rings and valve and compressing the module on both sides of the acrylic plate using binder clips.

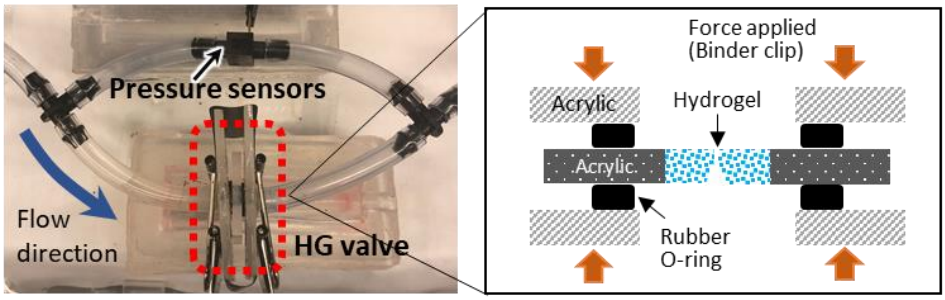

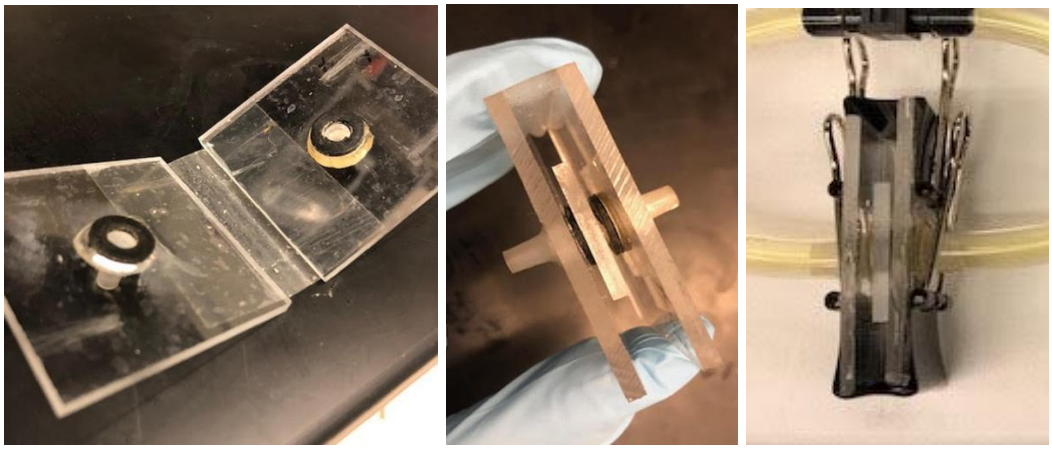

- CSF

  CSF is collected from hydrocephalic patients at the Phoenix Children's Hospital with an approved materials transfer agreement (MTA). The CSF solutions were from an aggregate of multiple CSF bags and maintained in a 4°C environment when not in use.

- Pressure and flow rate sensors

  Commercial resistive pressure sensors (PX26-001DV, Omega) with customized calibrations

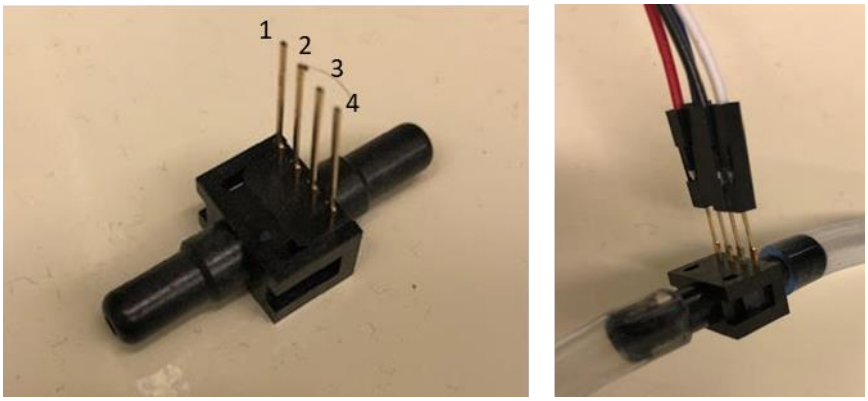

1: Red wire: V_{CC}

2: Blue wire: Input signal #1

3: Black wire: Ground

4: White wire: Input signal #2

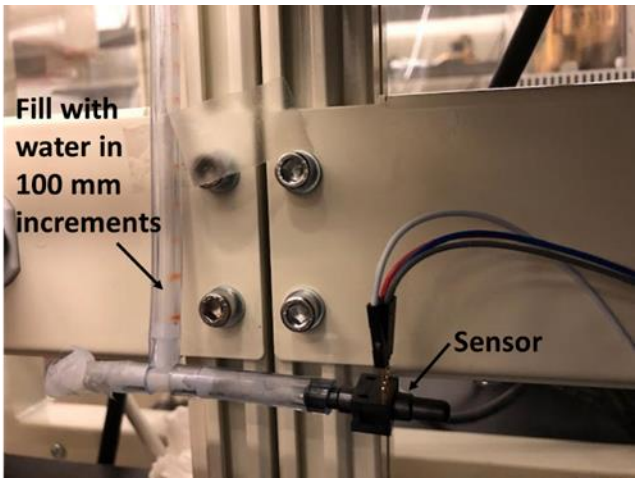

* Pressure sensor calibration

- Connect the sensor, which is needed to calibrate, at the end of the tubing at the bottom of the calibration set.

- Fill the tubing with water in 100mm increment (or 50mm), then measure the voltage of the sensor at each step by SignalExpress.

* Filling up 100mm of water = Applying 100 mmH_2O

* Filling up 200mm of water = Applying 200 mmH_2O

……

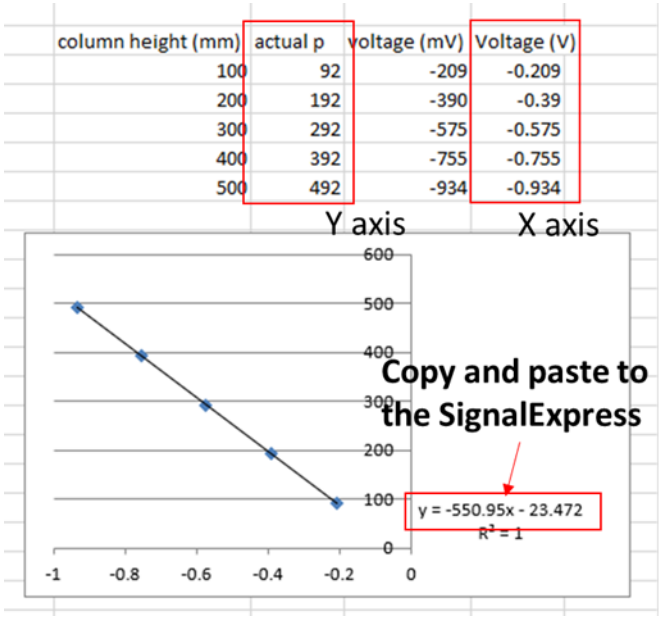

- Collect the data and create a plot

- Copy the trendline equation, paste it to the SignalExpress (‘Step setup’ for Pressure difference)

* Flow rate sensor calibration

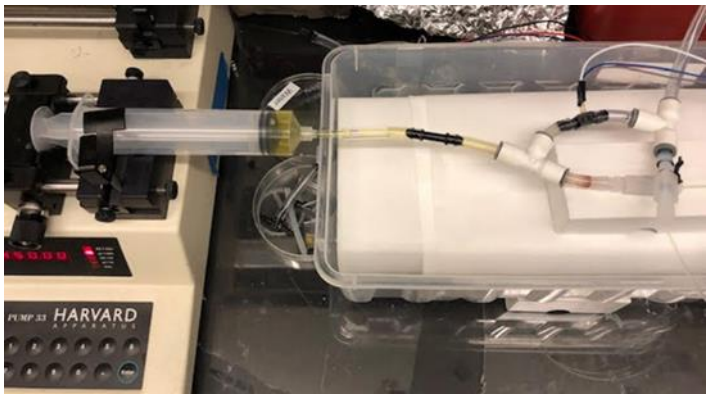

- Connect the flow rate sensor directly to the syringe pump
- Apply flow rate by increasing the flow rate at regular intervals, then measure the voltage of the sensor at each step by SignalExpress.

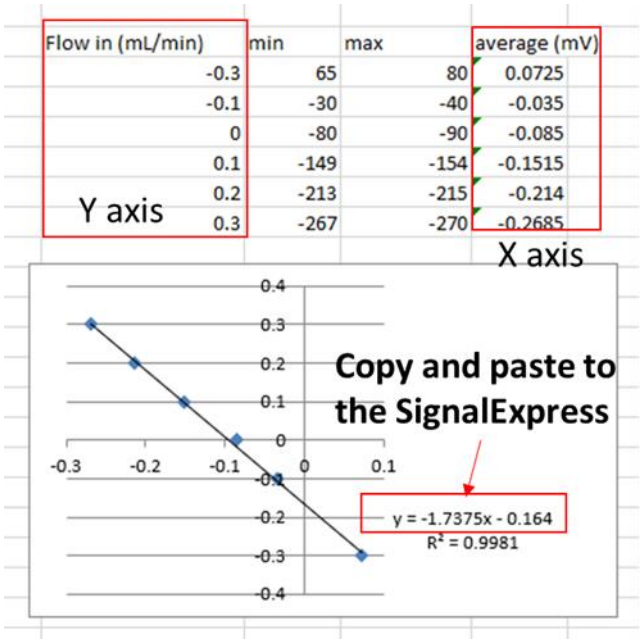

- Collect the data and create a plot
- Copy the trendline equation, paste it to the SignalExpress (‘Step setup’ for Flow)

- Signal detection for the sensors

  The electric signals, voltage, from the sensors are transmitted through voltage amplifier and data acquisition board (NI USB 6216, National Instruments) and recorded by Signal express software on a PC.

  *Amplifier circuit (using dual differential op-amp, TL082)

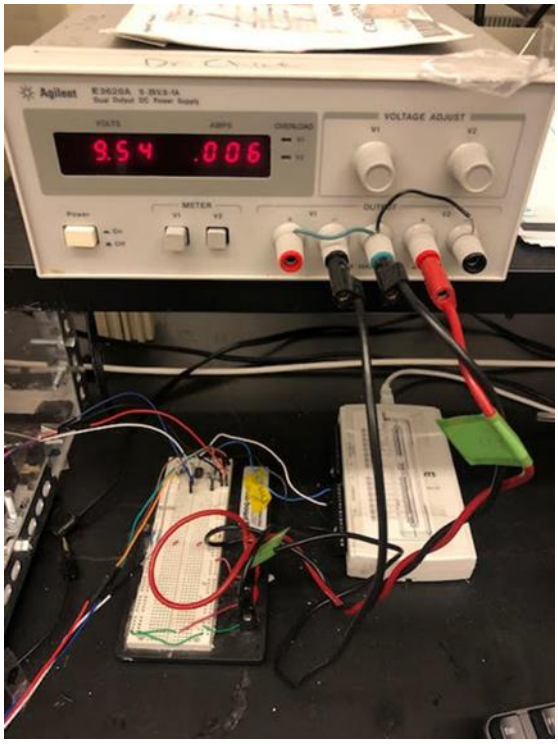

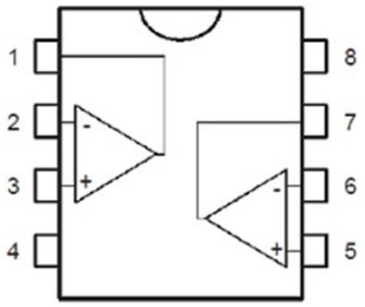

1 - Offset null 1
2 - Inverting input 1
3 - Non-inverting input 1
4 - V_{CC}^-
5 - Non-inverting input 2
6 - Inverting input 2
7 - Output 2
8 - V_{CC}^+

TL082 pinout

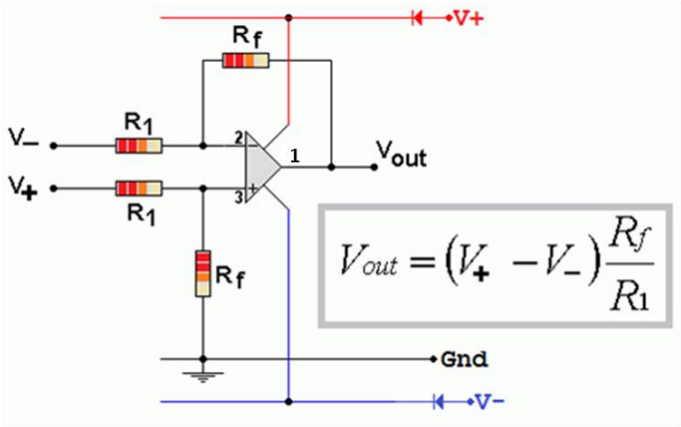

$$V_{out} = (V_+ - V_-)\frac{R_f}{R_1}$$

Differential op amp gain

- SignalExpress

  * Basic window for data measurement

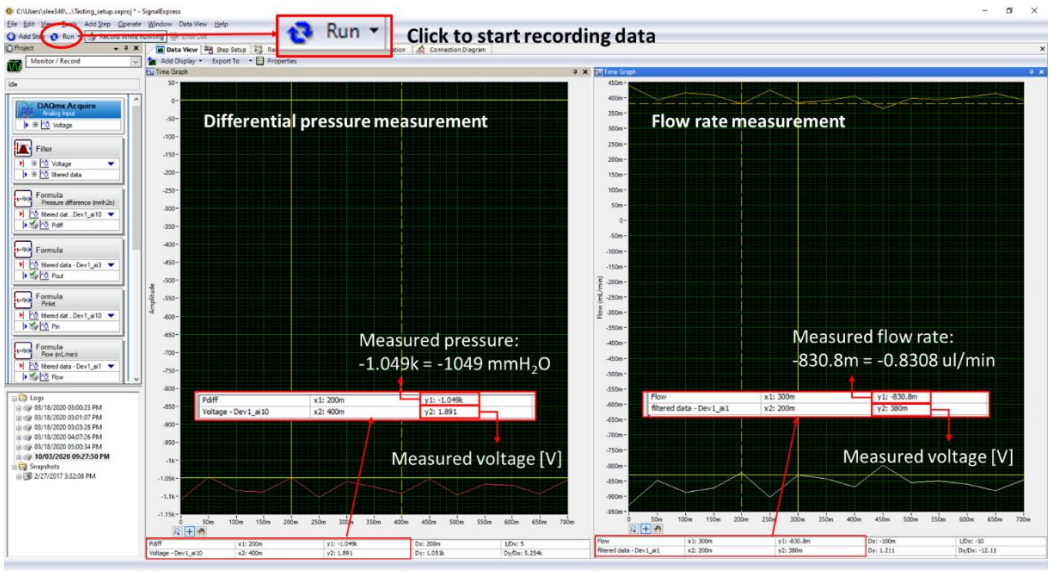

  * Apply calibrated equations

    - For a pressure sensor

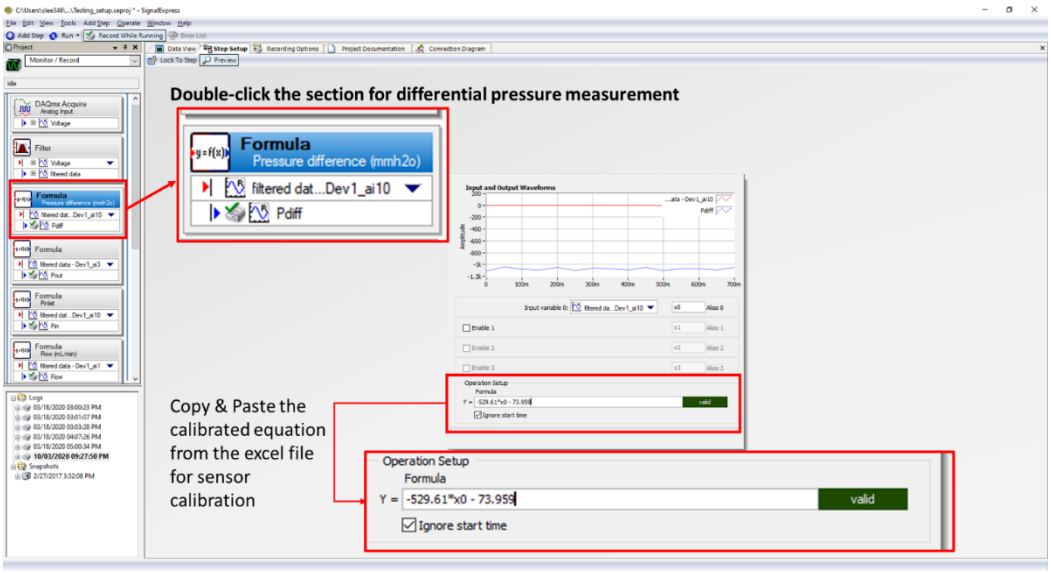

- For a flow rate sensor

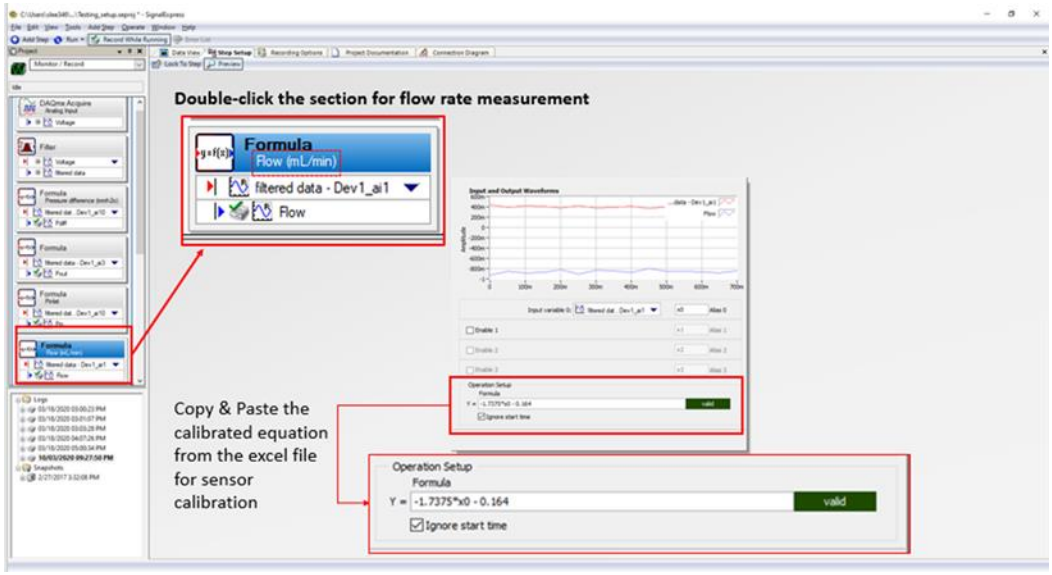

- Data collection

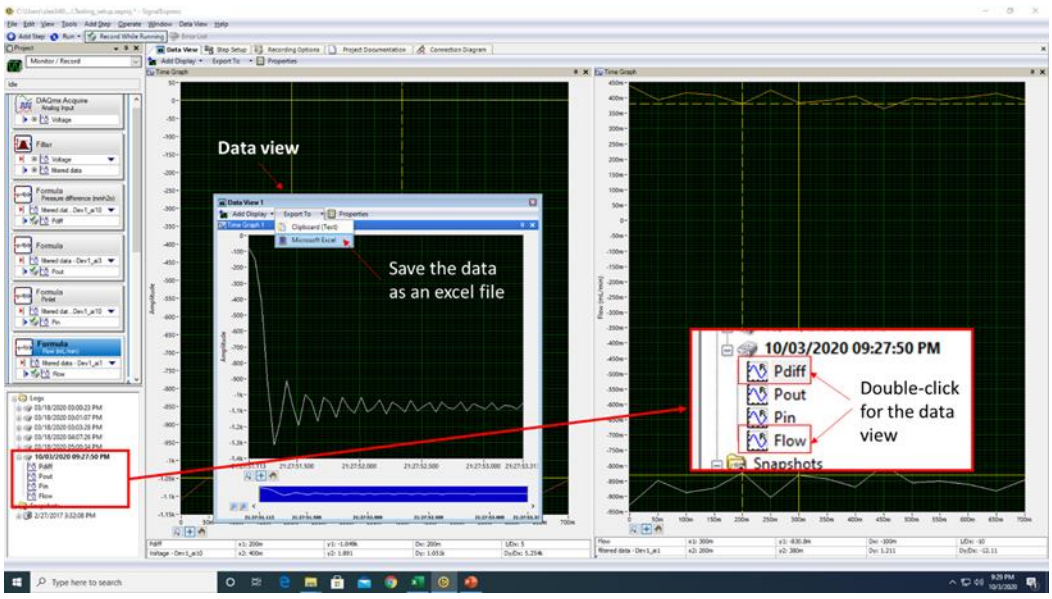

- Imported quantitative data from SignalExpress

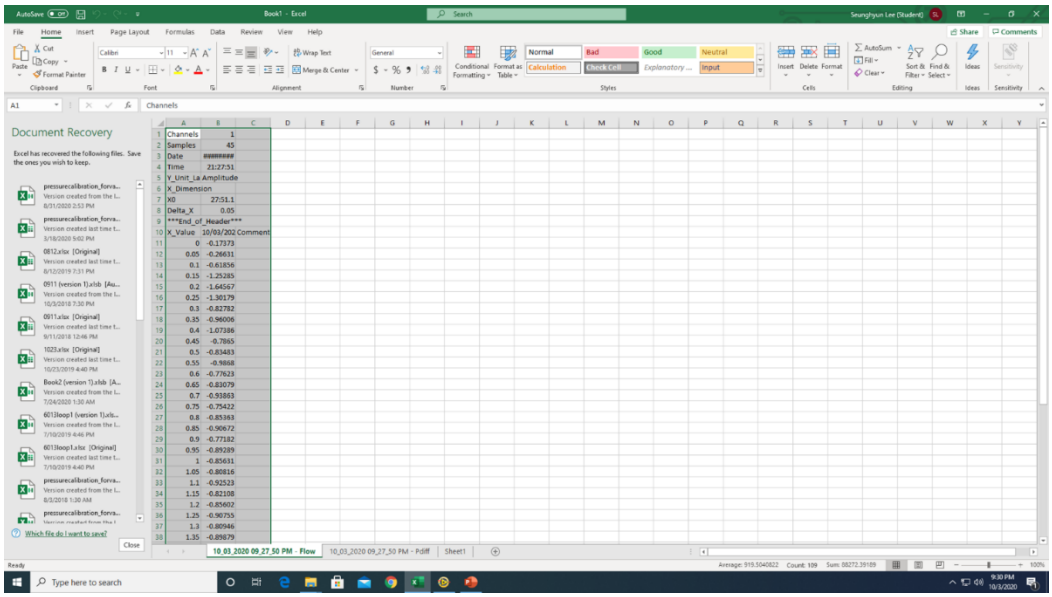

- Bench-top long-term functional test

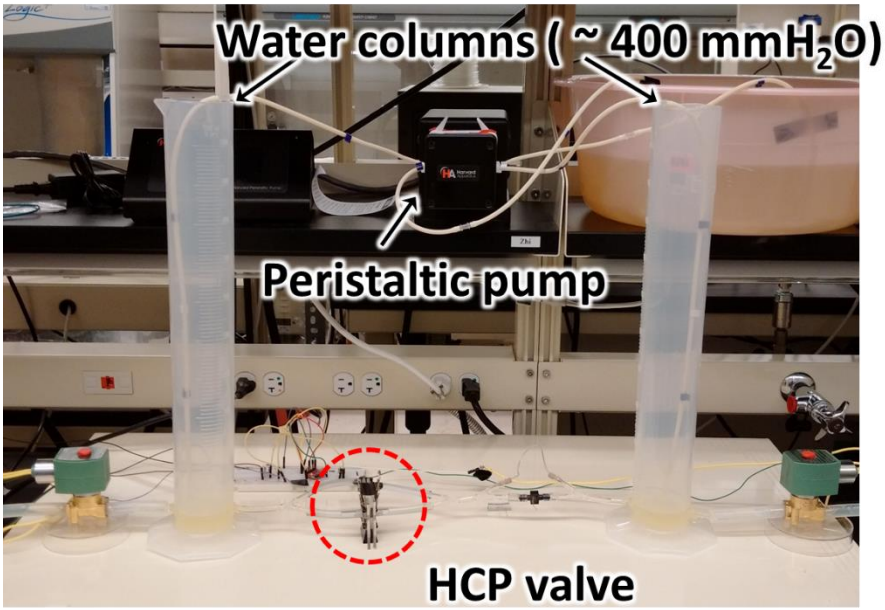

- Fluid source:

  Peristaltic pump (P-70, Harvard Apparatus) with water columns (1000 mL gradient cylinders)

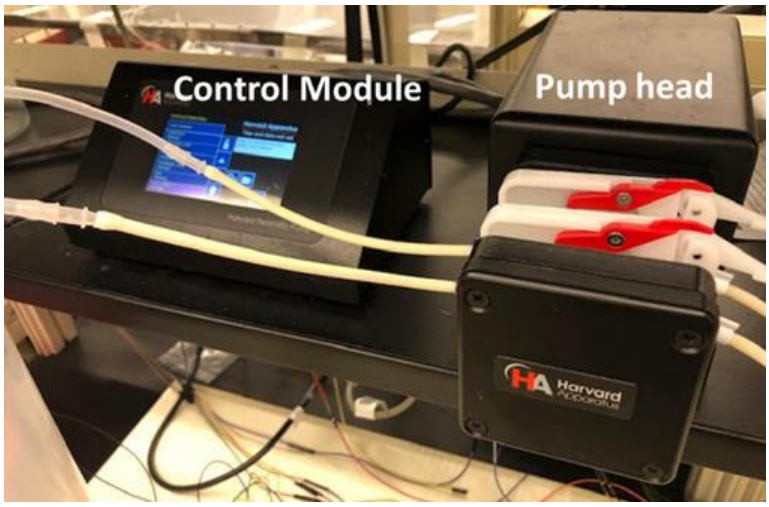

* Program setup

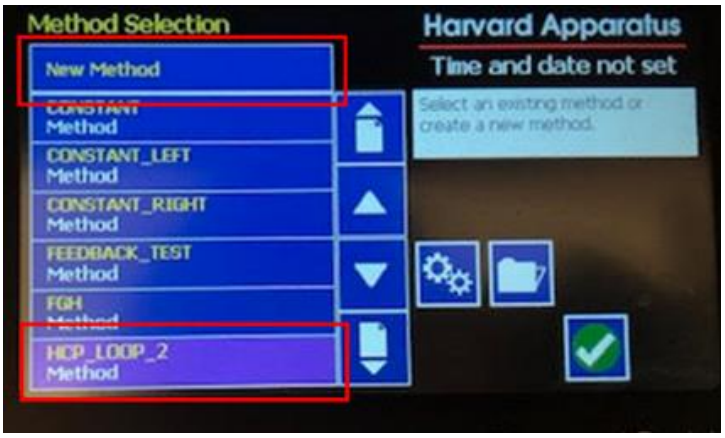

- If you need a new pumping method, choose the “New Method” on the touch panel.

- If you want to use previous pumping method for the long-term test, choose the “HCP_LOOP_2”.

<HCP_LOOP_2>

* Tubing selection

- Choose the “Tubing select” → Select from the list or Enter the size of the tubing you will use.

* Process programming

- Choose the “Step Definition” → Setup detail pumping process

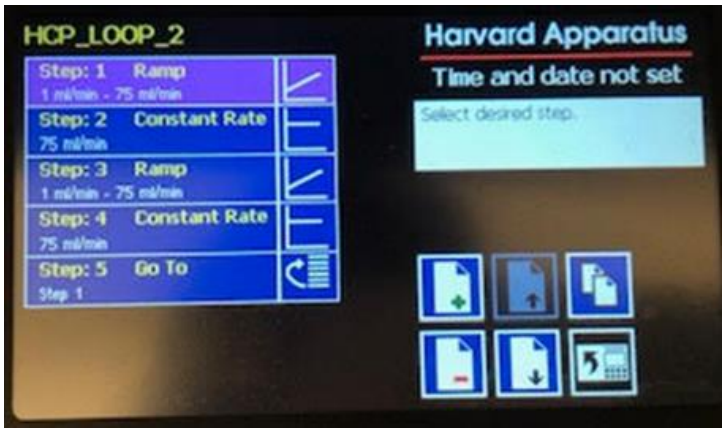

- Choose a step you want to modify

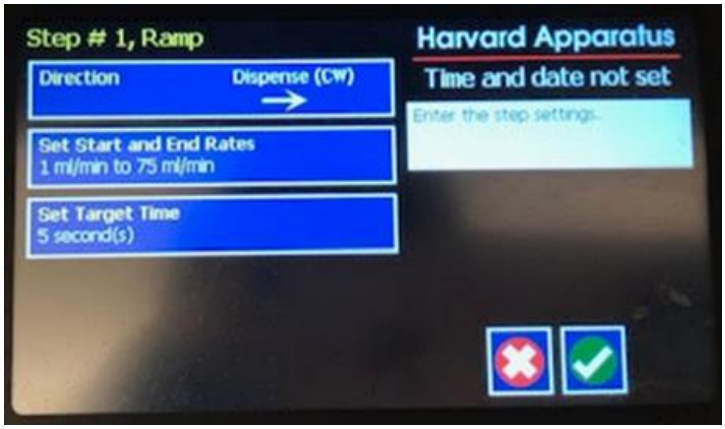

- Setting parameters: Direction / Start and End Rates / Target Time

* Creating a new step:

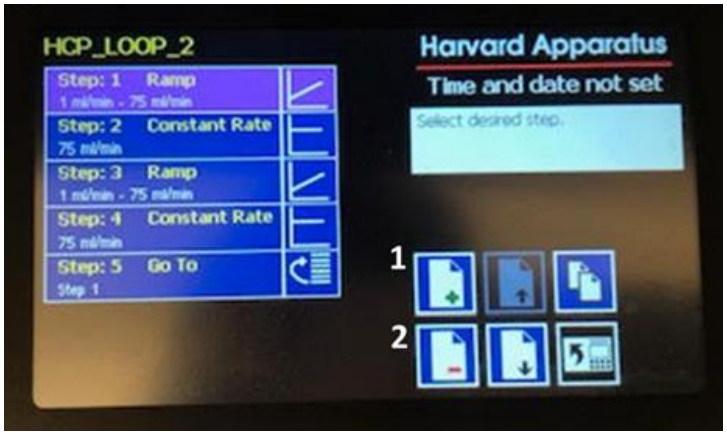

- Tap icon #1 → Select proper pumping profile → Set detail parameters

* Delete a step: Choose the step you want to delete → Tap icon #2

- Touch screen button reference

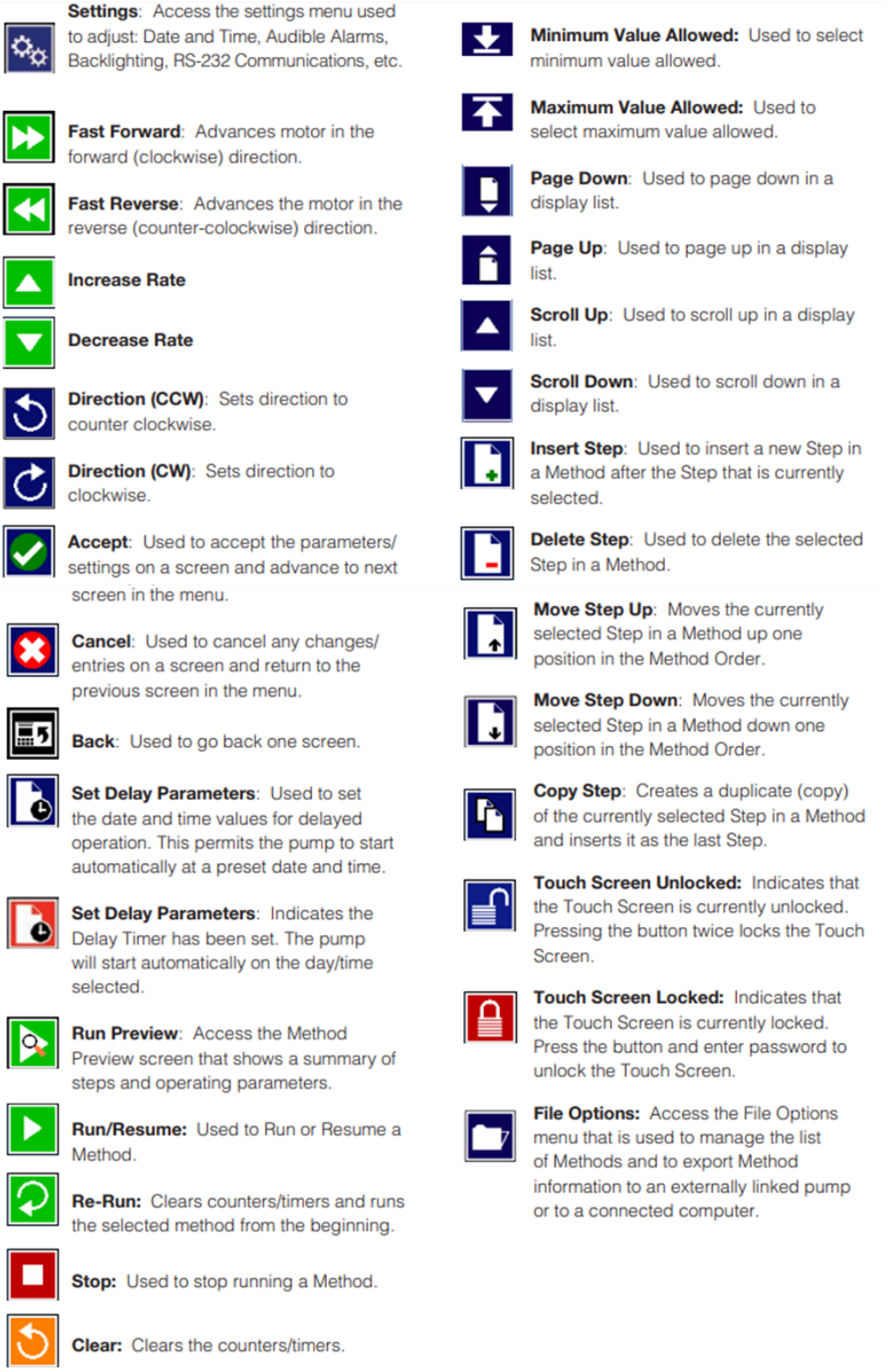

Settings: Access the settings menu used to adjust: Date and Time, Audible Alarms, Backlighting, RS-232 Communications, etc.

Fast Forward: Advances motor in the forward (clockwise) direction.

Fast Reverse: Advances the motor in the reverse (counter-colockwise) direction.

Increase Rate

Decrease Rate

Direction (CCW): Sets direction to counter clockwise.

Direction (CW): Sets direction to clockwise.

Accept: Used to accept the parameters/ settings on a screen and advance to next screen in the menu.

Cancel: Used to cancel any changes/ entries on a screen and return to the previous screen in the menu.

Back: Used to go back one screen.

Set Delay Parameters: Used to set the date and time values for delayed operation. This permits the pump to start automatically at a preset date and time.

Set Delay Parameters: Indicates the Delay Timer has been set. The pump will start automatically on the day/time selected.

Run Preview: Access the Method Preview screen that shows a summary of steps and operating parameters.

Run/Resume: Used to Run or Resume a Method.

Re-Run: Clears counters/timers and runs the selected method from the beginning.

Stop: Used to stop running a Method.

Clear: Clears the counters/timers.

Minimum Value Allowed: Used to select minimum value allowed.

Maximum Value Allowed: Used to select maximum value allowed.

Page Down: Used to page down in a display list.

Page Up: Used to page up in a display list.

Scroll Up: Used to scroll up in a display list.

Scroll Down: Used to scroll down in a display list.

Insert Step: Used to insert a new Step in a Method after the Step that is currently selected.

Delete Step: Used to delete the selected Step in a Method.

Move Step Up: Moves the currently selected Step in a Method up one position in the Method Order.

Move Step Down: Moves the currently selected Step in a Method down one position in the Method Order.

Copy Step: Creates a duplicate (copy) of the currently selected Step in a Method and inserts it as the last Step.

Touch Screen Unlocked: Indicates that the Touch Screen is currently unlocked. Pressing the button twice locks the Touch Screen.

Touch Screen Locked: Indicates that the Touch Screen is currently locked. Press the button and enter password to unlock the Touch Screen.

File Options: Access the File Options menu that is used to manage the list of Methods and to export Method information to an externally linked pump or to a connected computer.

- Sheep brain

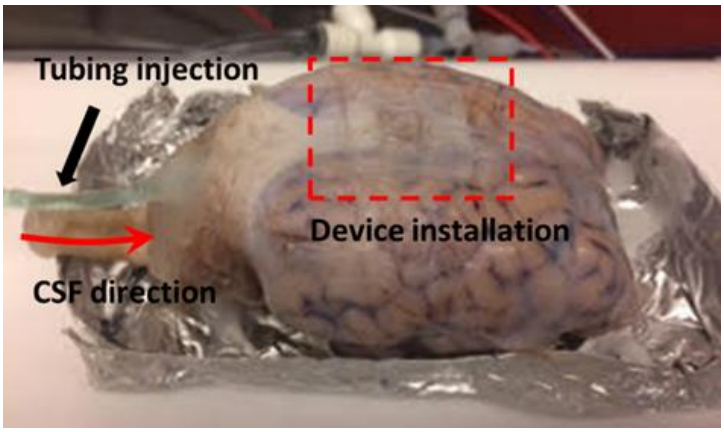

- PDMS molding
  - Insert tubes into the sheep brain for CSF injection.
  - Prepare temporal basket made from aluminum foil and put the sheep brain in the temporal basket.
  - Pour PDMS in the basket so that the top of the sheep brain won't submerged.
  - Cure the PDMS overnight (45˚C ~ 55˚C)

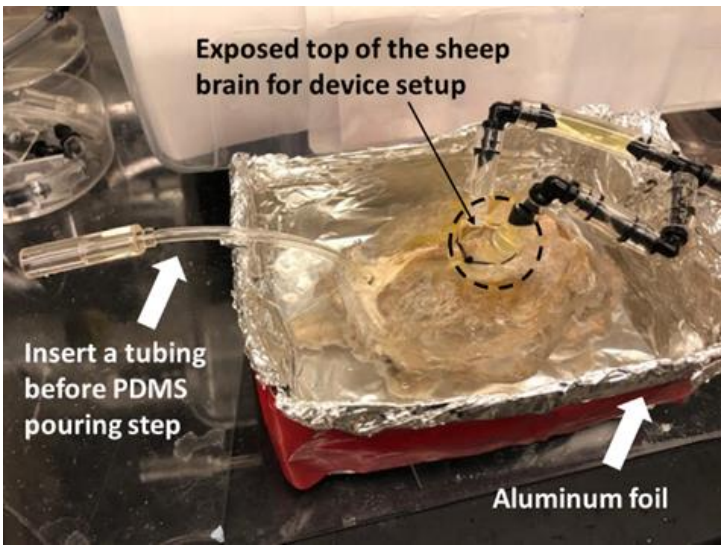

- Valve setup. The valve was placed on designated points of dura mater manually punctured.

❖ Experiments

- Turn on the syringe pump at 450 μL/min flow rate

  * The average CSF flow rate in human brains: $200 < Q_O < 700$ μL/min
- Start recording the signal by SignalExpress (Click ‘Run’ button)
- Collect data at the range of pressure ($-1000 < \Delta P < 1000$ mmH_2O)
- After collecting data for the target period, stop recording (click ‘Stop’ button) and then analyze the data set

• Example data

  * SignalExpress data

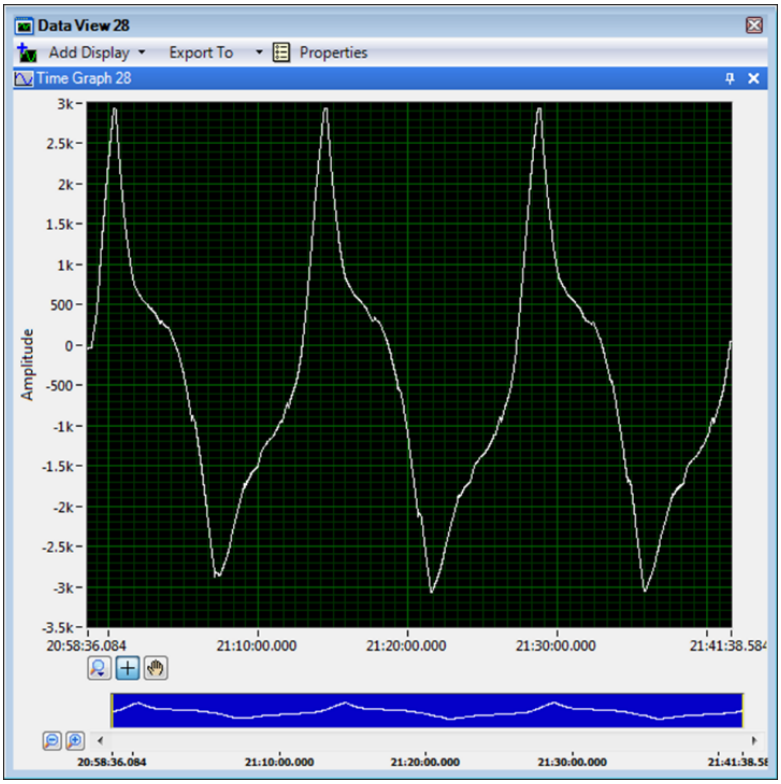

- Data for the applied pressure across the valve
- ΔP [mmH2O] vs Time [s]

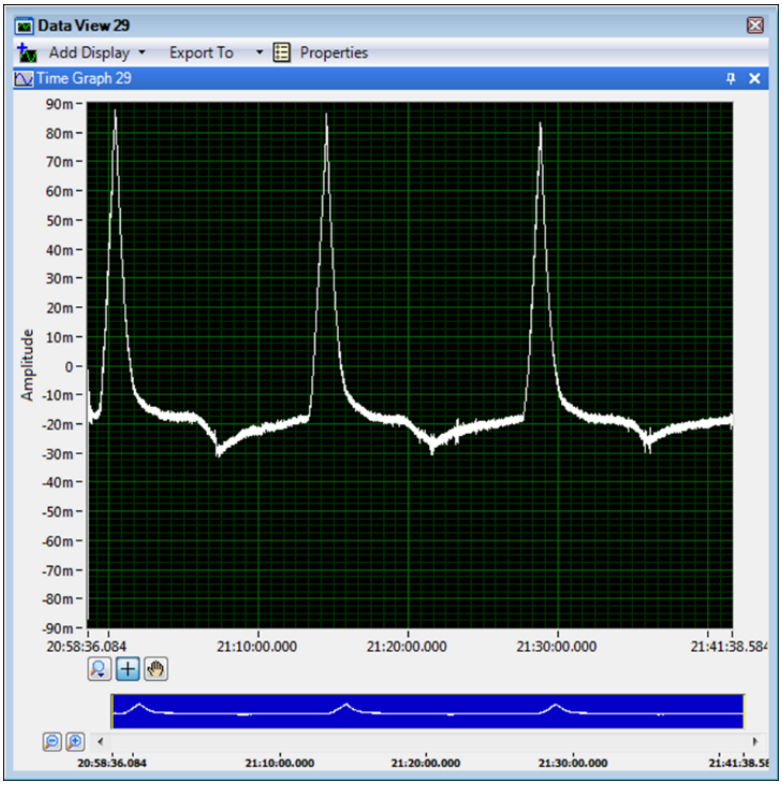

- Data for the flow rate through the valve

- Q [ul/min] vs Time [s]

* Excel data imported from the SignalExpress

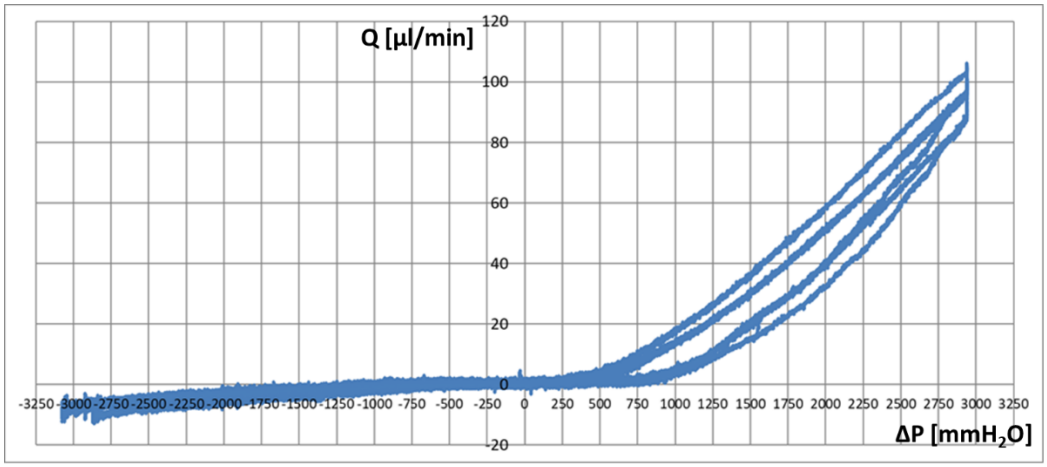

* Failure examples

- Fail to prevent reverse flow

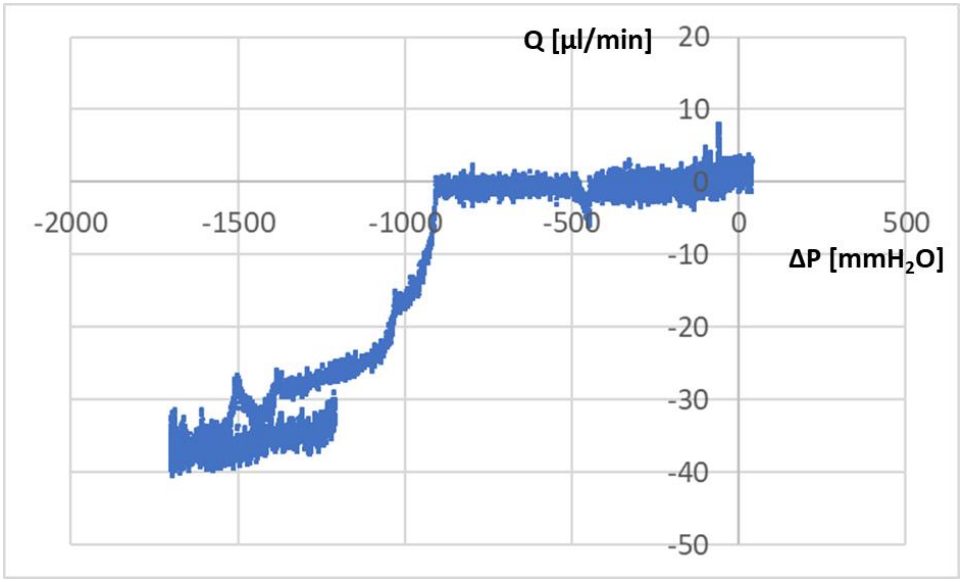

- Fail to have enough flow rate

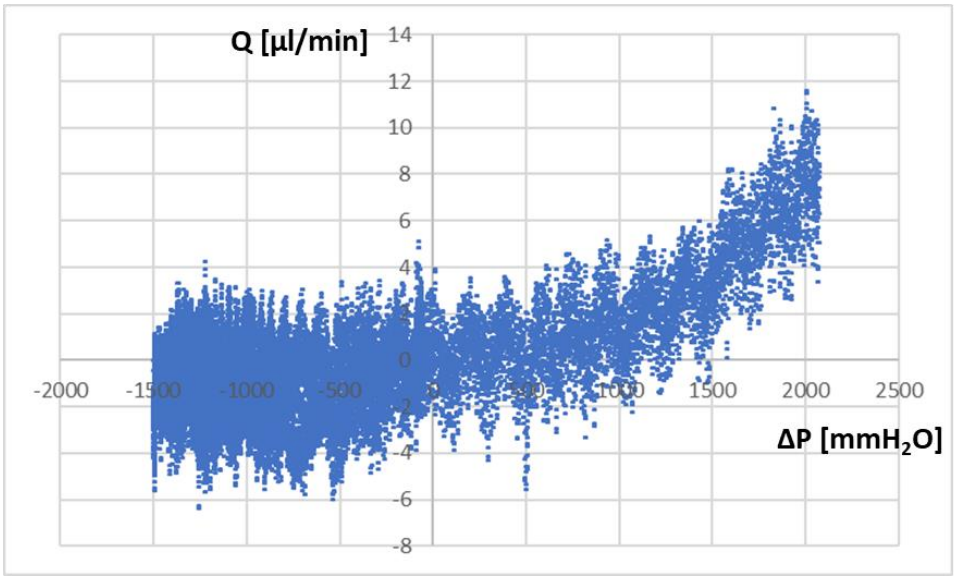

- Fail to have check-valve property